Stony Brook University

Diamond detector--material science, design and application

A Dissertation Presented

by

Mengjia Gaowei

to

The Graduate School

in Partial Fulfillment of the

Requirements

for the Degree of

Doctor of Philosophy

in

Materials Science and Engineering

Stony Brook University

May 2014

Stony Brook University

The Graduate School

Mengjia Gaowei

We, the dissertation committee for the above candidate for the

Doctor of Philosophy degree, hereby recommend

acceptance of this dissertation.

Dr. John Smedley – Dissertation Advisor
Physicist, Instrumentation Division
Brookhaven National Laboratory

Dr. Michael Dudley - Dissertation Co-Advisor
Professor, Department of Materials Science and Engineering
Stony Brook University

Dr. Balaji Raghothamachar – Chair of Committee
Research Assistant Professor, Department of Materials Science and Engineering
Stony Brook University

Dr. Erik Muller – Committee Member
Research Assistant Professor, Department of Physics and Astronomy
Stony Brook University

This dissertation is accepted by the Graduate School

Charles Taber
Dean of the Graduate School

Abstract of the Dissertation

Diamond detector--material science, design and application

by

Mengjia Gaowei

Doctor of Philosophy

in

Materials Science and Engineering

Stony Brook University

2014

Modern synchrotrons will enable unprecedented science by having extremely high brightness and flux with exceptional beam stability. These capabilities create a harsh and demanding environment for measuring the characteristics of the x-ray beam. In many cases, existing measurement techniques fail completely, requiring the development of new detectors which can meet the demands of the synchrotron. The combination of diamond properties ranked diamond an appealing candidate in the field of radiation detection in extreme conditions and it has been used as x-ray sensor material for decades. However, only until the development of chemical vapor deposition (CVD) process in the synthesis of diamond that has it been considered for wider applications in the state-of-art synchrotron light sources as part of beamline diagnostics, including the detection of x-ray beam flux and position.

While defects and dislocations in CVD grown single crystal diamonds are inevitable, there are solutions in other aspects of a device fabrication to compensate this technological downside, including improving device performance in engineering diamond surface electrode materials and patterns and slicing and polishing diamond plates into thinner pieces.

The content of this dissertation summarizes our effort in addressing several problems we encounter in the process of design and fabrication of single crystal CVD diamond based electronic devices. In order to study the generation of post-anneal photoconductive gain in our devices we have discussed in section 3 and 4 the two criteria for the observation of photoconductive current. In section 3 we reveal the correlation between structural defects in diamond and the post-anneal photoconductive regions. Section 4 introduces the measurements of hard x-ray photoelectron spectroscopy (HAXPES) we applied to investigate the diamond-metal Schottky barrier height for several metals and diamond surface terminations. The position of the diamond valence-band maximum was determined by theoretically calculating the diamond

density of states and applying cross section corrections. The diamond-platinum Schottky barrier height was lowered by 0.2 eV after thermal annealing, indicating annealing may increase carrier injection in diamond devices leading to photoconductive gain.

In order to adapt our device to soft x-ray applications, efforts are made to develop a thin diamond position monitor for lowering device absorption. In section 5 we have discussed the fabrication and testing of thin diamond x-ray monitors made from diamond plates with nominal thickness of 30μm, which is 1/10th of the thickness of the diamonds we previously used. Calibration results of this detector are presented and discussed in comparison with thicker diamond sensors.

Section 6 introduces our effort on the investigation of carrier loss mechanism in diamond detectors. Near edge responsivity in diamond x-ray detectors has been used to confirm the carrier loss mechanism as recombination due to diffusion into the incident electrode. We present a detailed study of the bias dependence of the diamond responsivity across the carbon k-edge. The carrier loss is modelled by incorporating a characteristic recombination length into the absorption model and is shown to agree well with Monte Carlo simulated carrier losses.

In addition, nitrogen doped ultrananocrystalline diamond (nUNCD) grown on the surface of a CVD single crystal diamond as an alternative contact to metal is tested in the similar measurements as the metal contact diamond. nUNCD has a much lower x-ray absorption than metal contacts and is designed to improve the performance of our device. This diamond is calibrated over a wide photon energy range from 0.2 keV to 28 keV, and compared with platinum coated diamond. Results of these studies will be presented and discussed in section 7.

Future work has been proposed in the last section in improving the design and fabrication of diamond based electronics as well as in the investigation to enhance our understanding of its material and device physics.

Dedicated to my family and friends.

谨以此文献给我的家人和朋友。

Table of Contents

List of Figures

List of Tables

List of Abbreviations

CVD	Chemical vapor deposition
BDD	Boron doped diamond
SWBXT	Synchrotron white beam X-ray topography
XRT	X-ray topography
XBIC	X-ray beam induced current
HAXPES	Hard X-ray photoelectron spectroscopy
nUNCD	Nitrogen doped ultrananocrystalline diamond

Acknowledgments

I would like to express my sincere gratitude to my advisor, Dr. John Smedley and my co-advisor, Prof. Michael Dudley for introducing me to this project and their guidance and support to my work on this project, and for agreeing to be my defense committee members. Professor Dudley has given valuable advices on the characterization of diamonds in this project and provided great insight to my work from his profound knowledge in the field of x-ray topography and crystal defect characterization.

Special thanks are given to Dr. Erik Muller for joining this committee and for sharing his expertise in many aspects of this project. In the past 4 years Dr. Muller has given me valuable advices in both theoretical understanding and experimental details of my thesis work. It is my great pleasure to work with Dr. Muller in the diamond project.

Thanks are also given to Dr. Balaji Raghothamachar for joining this committee and for his help and advices to my research work.

I would like to express my gratitude to Prof. Ilan Ben-Zvi for introducing me to the diamond work and have been a great guidance over the project.

I would also like to thank John Walsh for the design and fabrication of sample mounts and technical assistance and Dr. Xiangyun Chang and Dr. Qiong Wu for their assistance with sample metallization. Thanks are given to Dr. Bin Dong and Dr. James Distel for their technical assistance at beamline U3C and X8A. The team is further indebted to Jeff Keister, Jen Bohon, Triveni Rao, Dimitre Dimitrov and Ilan Ben-Zvi for discussion and contributions over the course of this work.

Thanks are also given to staff at Center for Functional Nanomaterials, Dr. Ming Lu, Dr. Aaron Stein, Dr. Fernando Camino and Dr. Xiao Tong for their assistance in the experiments.

Special thanks are given to Dr. A. K. Rumaiz, Dr. C. Weiland, Dr. E. Cockayne, Dr. J. Jordan-Sweet and Dr. J. C. Woicik for their contributions in the HAXPES measurements and in the discussion of the results interpretation.

I'd also like to thank my lab members and my friends in Stony Brook University and in Brookhaven National laboratory.

This work is supported by U.S. Department of Energy under grants KC0407-ALSJNT-I0013 and DE-FG02_08ER41547.

Use of the National Synchrotron Light Source and Center for Functional Nanomaterials, Brookhaven National Laboratory, was supported by the U.S. Department of Energy, Office of Science, Office of Basic Energy Sciences, under Contract No. DE-AC02-98CH10886.

Publications

M. Gaowei, E. M. Muller, A. K. Rumaiz, C. Weiland, E. Cockayne, J. Jordan-Sweet, J. Smedley, and J. C. Woicik, Appl. Phys. Lett. 100, 201606 (2012).

E. M. Muller, **M. Gaowei**, I. Ben-Zvi, D. A. Dimitrov and J. Smedley, Appl Phys Lett 104 (9), (2014).

E. M. Muller, J. Smedley, J. Bohon, X. Yang, **M. Gaowei**, J. Skinner, G. De Geronimo, M. Sullivan, M. Allaire, J. W. Keister, L. Berman and A. Heroux, J Synchrotron Radiat **19**, 381-387 (2012).

E. M. Muller, J. Smedley, B. Raghothamachar, **M. Gaowei**, J. W. Keister, I. Ben-Zvi, M. Dudley and Q. Wu, in Diamond Electronics and Bioelectronics — Fundamentals to Applications III, edited by P. Bergonzo, J.E. Butler, R.B. Jackman, K.P. Loh, M. Nesladek (Mater. Res. Soc. Symp. Proc) (Warrendale, PA, 2010), Vol. 1203, (2010).

Section 1 Introduction

For over 3,000 years diamond has been recognized as the hardest substance on earth and as a gemstone, carrying symbolic or religious meanings over the long history of human culture. Not until the prosperity of modern science had diamond become a subject of scientific investigation, for its mechanical, optical, chemical as well as electrical properties. In 1663, Irish natural philosopher Robert Boyle reported about diamond thermo-luminance, which was considered the earliest report on the investigation of the properties of diamond as a semiconductor. [1]

1.1 Diamond properties

It is now well aware that the intrinsic diamond has a large band-gap of 5.47 eV, which makes it insensitive to visible light. It has a high breakdown voltage (~10^7 V/cm), much higher than that of Si (~10^3 V/cm) and a much higher limit of the saturated carrier drift velocity. Its thermal conductivity is more than 4 times higher than that of copper at room temperature.[2] Diamond properties that are relevant to this report are summarized in Table 1. [3]

Table 1 Diamond Properties

Dielectric constant (10^2-10^4 Hz)	5.7
Breakdown field	10^8-10^9 V/m
Mobility of holes	$\leq$1800 $cm^2V^{-1}s^{-1}$
Mobility of electrons	$\leq$2200 $cm^2V^{-1}s^{-1}$
Indirect band gap	5.47 eV
Direct band gap	7 eV
Electron thermal velocity	~10^5m/ s
Saturated electron drift velocity	$2.7\cdot10^7$cm/s

1.2 Diamond based electronics

The combination of diamond properties ranked diamond an appealing candidate in the field of radiation detection in extreme conditions and diamond has been used as x-ray sensor material for decades.[4-7] However, only until the development of chemical vapor deposition (CVD) process in the synthesis of diamond that has it been considered for wider applications in the state-of-art synchrotron light sources as part of beamline diagnostics, including beam flux and position monitoring.[8-11] Examples include the RD42 effort of the Large Hadron Collider[5, 12], which has been a principle development in diamond based electronics, and accelerator

diagnostics in the field of high energy physics[1, 2, 5, 10-15], due to diamond's high resistance of radiation damage. Diamond detectors has also be developed in the interest of astrophysics and solar astronomy[16, 17], as well as finding its application in medical devices that measure the relative dose distribution in radiotherapy[18, 19]. Diamond devices have been tested in low power monochromatic beam as well as high power focus white beam and its response linearity has been determined over 11 orders of magnitude. [8, 20]

Current application of the diamond devices built by our group are functioning as part of beam diagnostics in various facilities, including the white beam position monitors installed in beamline X25A, NSLS, where two identical diamond devices are aligned in the beam path to calibrate the beam direction (see Appendix V for detailed test results),[21] and a beam flux monitor at beamline X23A, NSLS, which is an x-ray absorption spectroscopy beamline that uses monochromatic beam ranging from 4.9keV to 30keV,[22] and the position x-ray monitor at the beamline G3, CHESS, which is an in-situ hard x-ray diffraction beamline, to detector beam flux and position.[23]

1.3 Structural defects in CVD diamond

1.3.1 Growth dislocations

The diamond cubic structure is based on the FCC structure and dislocations in this structure are known to lie on (111) planes and to have ½<110> Burgers' vectors. Single crystal diamond grown by chemical vapor deposition (CVD) has far less impurities than the ones grown by high temperature high pressure (HTHP) processes. However, in x-ray topography and TEM studies edge and mixed dislocations lying approximately along <001> direction (the growth direction) with Burgers' vector 1/2<110> are still observed.[24] Martineau et al. found that dislocations in homoepitaxial CVD diamond layers tend to nucleate at or near the interface with their substrate. Growth dislocations are often observed in bundles and fan out along [110] directions. In particular, the ones with its projections on (001) plane along [110] and [-1-10] have ½<1-10> Burgers' vectors, while those with projections along [1-10] or [-110] have Burgers' vector of ½<110>. One bundle of dislocations has a net Burgers' vector of 0.[25] Examples are given in Figure 1 of 4 different reflections for a typical bundle of dislocations in CVD diamond. Scales in Figure 1 indicating contrast of these dislocation bundles in x-ray topography image, which arises from the strain field caused by displacements of crystal lattice. Details will be introduced in Section 2.1.

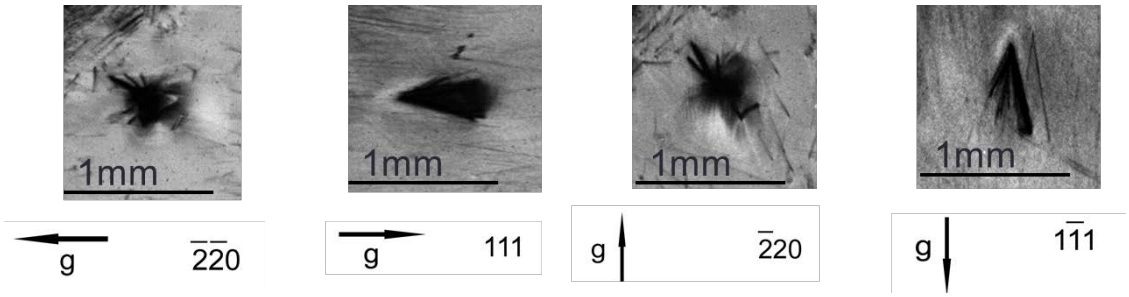

Figure 1 A typical bundle of dislocations in 4 different reflections in x-ray white beam topography.

1.3.2 Stress relaxation/ processing introduced slip bands

Aside from crystal growth, dislocations can also be formed during crystal processing when they are induced by mechanical stress during thermal treatments.[26] In the case of CVD single crystal diamond, laser cutting and mechanical polishing will introduce stress relaxation inside the crystal. Slip bands coming from the edge of the diamond plates are widely observed in our x-ray topographs and might fall into this category. (Figure 2)

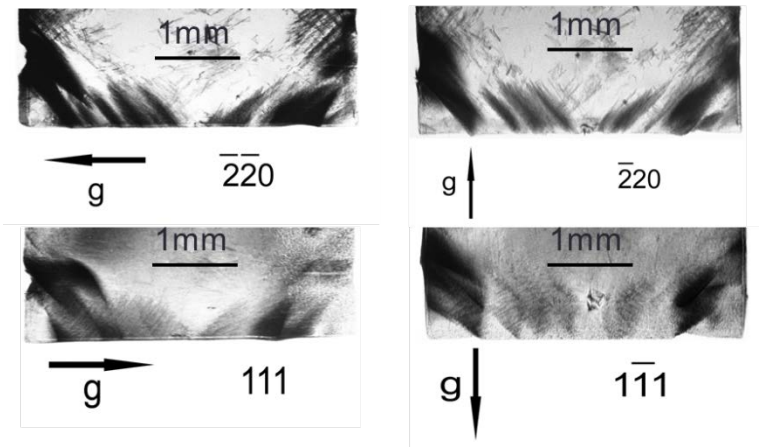

Figure 2 X-ray topographs of slip bands in single crystal CVD diamond in 4 reflections.

1.3.3 Seed or solvent introduced point defects

Earlier reports suggest that both metallic and silicate phases of inclusions can be formed inside the diamond during the process of synthesis.[27] While the control of point impurity and other point defects has significantly improved and recent research suggests that inclusions can hardly be found in current CVD diamond,[28] point defects are difficult to be eliminated and can be introduced by the substrate or reaction chamber contamination.[29]

1.4 Motivation

While defects and dislocations in CVD grown single crystal diamonds are inevitable, there are solutions in other aspect of a device fabrication to compensate this technological downside, including improving device performance in engineering diamond surface electrode materials and patterns and slicing and polishing diamond plates into thinner pieces.

The following sections have summarized our effort in addressing several problems we encounter in the process of design and fabrication of single crystal CVD diamond based electronic devices. In order to study the generation of post-anneal photoconductive gain in our devices we have discussed the correlation between structural detects in diamond and the post-anneal photoconductive regions. Hard x-ray photoelectron spectroscopy (HAXPES) was applied to investigate the diamond-metal Schottky barrier height for several metals and diamond surface terminations. The position of the diamond valence-band maximum was determined by theoretically calculating the diamond density of states and applying cross section corrections. The diamond-platinum Schottky barrier height was lowered by 0.2eV after thermal annealing, indicating annealing may increase carrier injection in diamond devices leading to photoconductive gain.

In order to adapt our device to soft x-ray applications, efforts are made to develop a thin diamond position monitor for lowering device absorption. In section 5 we have discussed the fabrication and testing of thin diamond x-ray monitors made from ~30 micron diamond plates, which is 1/10th of the thickness of the diamonds we previously used. Calibration results of this detector are presented and discussed in comparison with thicker diamond sensors.

Section 6 introduces our effort on the investigation of carrier loss mechanism in diamond detectors. Near edge responsivity in diamond x-ray detectors has been used to confirm the carrier loss mechanism as recombination due to diffusion into the incident electrode. We present a detailed study of the bias dependence of the diamond responsivity across the carbon k-edge. The carrier loss is modelled by incorporating a characteristic recombination length into the absorption model and is shown to agree well with Monte Carlo simulated carrier losses.

In addition, nitrogen doped ultrananocrystalline diamond (nUNCD) grown on the surface of a CVD single crystal diamond as an alternative contact to metal is tested in the similar measurements as the metal contact diamond. nUNCD has a much lower x-ray absorption than metal contacts and is designed to improve the performance of our device. This diamond is calibrated over a wide photon energy range from 0.2 keV to 28 keV, and compared with the Pt contact diamond. Results of these studies will be presented and discussed in section 7.

Future work has been proposed in the last section in improving the design and fabrication of diamond based electronics as well as in the investigation to enhance our understanding of its material and device physics.

Section 2 Investigation methods

The presented work in the preceded sections summarizes the effort on designing and fabricating diamond x-ray detectors to improve device performance in real applications. Synchrotron white beam x-ray topography (SWBXT) has been used to characterize structural defects and screen the diamonds proceeding for fabrication. Various micro-patterned Pt electrodes have been metalized onto oxygen terminated electronic grade single crystal CVD diamond surface using standard optical lithography. Energy calibration over a range of with photon energy as low as 50 eV and as high as 28 keV as well as 2D responsivity and position sensitivity tests at various photon energies have been performed for these devices. In addition, nitrogen doped ultrananocrystalline diamond (nUNCD) grown on the surface of a CVD single crystal diamond as a contact is tested in the similar measurements as the metal contact diamond. Hard x-ray photoelectron spectroscopy (HAXPES) was applied to investigate the diamond-metal Schottky barrier height for several metals and diamond surface terminations, as well as several types of boron doped diamonds prepared as low absorption diamond contact. This section introduces the principle techniques that are employed in this work.

2.1 SWBXT

Synchrotron X-ray white beam topography (SWBXT) is a technique based on the kinematical and dynamical diffraction of x-ray beams interacting with crystal lattices. Synchrotron radiation is known to provide x-ray beam with high brightness and low divergence, which renders it a suitable source for x-ray topography and a powerful non-destructive tool to microscopically investigate the crystallographic orientations and defect structures of various crystals.

White beam X-ray topography images were obtained at beamline X19C at the National Synchrotron Light Source (NSLS), BNL. With a 2.5 GeV 100 mA electron beam in the synchrotron accelerator, the flux at the beamline is 4.16×10^{12} ph/sec for 4.9 keV photons. A 4~25 keV near-parallel white beam is incident on the sample in a transmission geometry (shown in Figure 3), where the x-ray white beam is incident on the sample, at a set Bragg angle, the diffracted beam is projected onto an x-ray film. The diffraction spot constitutes an x-ray topography and it records the variation in the diffracted beam intensity as a function of position in crystal. Local diffracted beam intensity can be affected by the distorted regions sounding a crystal defect and gives rise to contrast in white beam x-ray topography.

The thin diamond sample is oriented in the incoming synchrotron white beam on a precision goniometer in order to simultaneously record the [$\overline{2}\overline{2}0$] and [111] reflections of diamond crystal on a 20 cm × 25 cm film placed in the transmission position perpendicular to the incident beam with a 10 cm distance away from the crystal. The direct beam is blocked after the sample to allow correct exposure for the diffraction images to clearly appear on the film (see Figure 4 for typical topographs from these single crystal CVD diamonds and the most used reflections, the images were recorded with sample rotating along vertical axis and horizontal axis respectively for 20° counterclockwise). The exposure time various from 3~20 seconds according to the incident X-ray intensity (filters might be applied to mitigate the beam to reduce thermal

vibration if necessary to improve image clarity) and sample thickness. [30] The recorded topographic images can provide information include the types, locations and density of crystal defects to allow evaluation and screening of diamond samples for x-ray detector development.

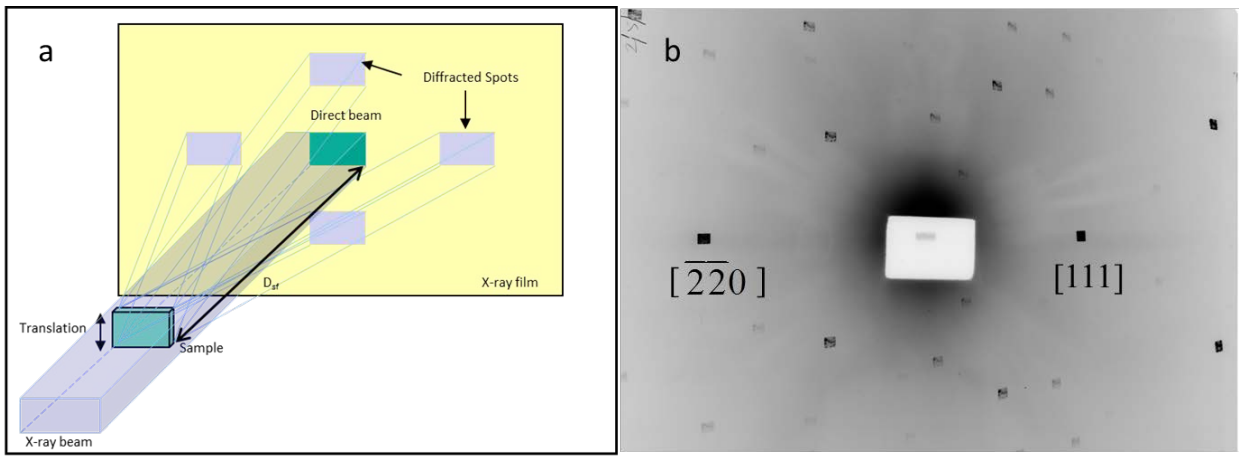

Figure 3 Schematics of Experimental set-up for projection topography; (b) Example projection recorded under the set up for single crystal diamond. Reflections of g=[-2-20] and g=[111] are labeled.

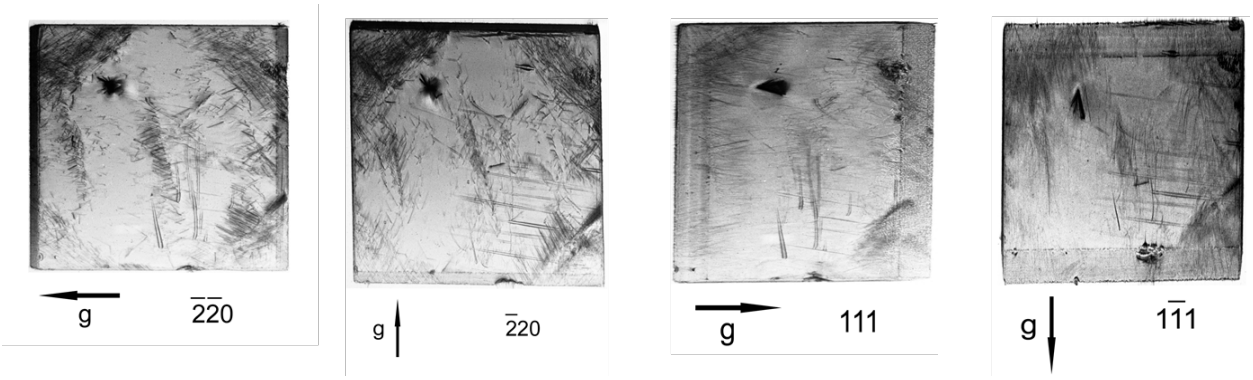

Figure 4 Typical topographs and the most used reflections from single crystal CVD diamond. Reflections of g=[-2-20] and g=[111] were recorded with sample rotating along vertical axis for 20° counterclockwise and g=[-220] and g=[1-11] were recorded with sample rotating along horizontal axis for 33° counterclockwise.

2.2 Optical lithography

Lithography is broadly applied in the fabrication and production of Micro Electro Mechanical Systems (MEMS) for micro-patterning thin film electrodes onto substrates. A typical pattern preparation process for our diamond device is described in Figure 5. Our lithography work is performed at Center for Functional Nanomaterials (CFN), BNL. Prior to lithography, diamond is ultrasonically cleaned in acetone, isopropanol followed by deionized water, and then both sides of the diamond plate are exposed under a UV ozone lamp for 4~6

hours to prepare oxygen terminated surfaces. Photoresist S1805 is spun onto diamond at 6000 rpm for 15 s and baked at 115 ºC for 90 s. Patterns are chosen from the pre-designed masks shown in Figure 6, SUSS MA6 contact aligner is used to expose the pattern onto the diamond and the exposure time is normally 10 s. But for near edge patterns, longer exposure time is needed. Sample is then developed in MF312 solution for 60s and the reaction stopped in DI water after 60 s. Metal (mostly platinum) is deposited onto diamond using DC sputtering for a set thickness of 30 nm. Lift-off is performed in acetone and for features smaller than 50 µm a gentle ultrasonic bath is required to fully remove resist and avoid electric shorting.

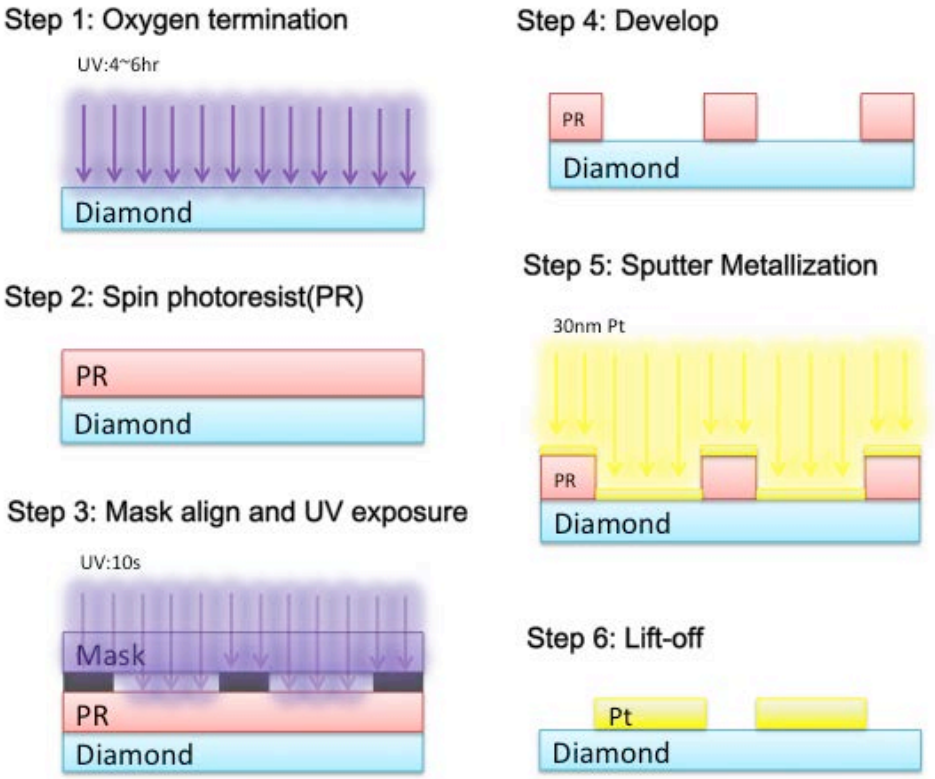

Figure 5 Sample preparation for oxygen terminated diamond surface and Pt micro-electrodes using optical lithography.

2.3 Mask design

A variety of electrode patterns were designed and assembled into a glass mask to adapt different experimental needs, including circular and square quadrant pads of varied sizes for x-ray position monitors and mesh electrode patterns with different metal coverage to study the field dependence of metal stripe size and spacing. Figure 6 gives an example of our mask design and several sample patterns. Patterns were designed using Layout software and the photo mask was made through a commercial company. Results of applications of diamond detectors applying some of these patterns are presented and discussed in the following sections.

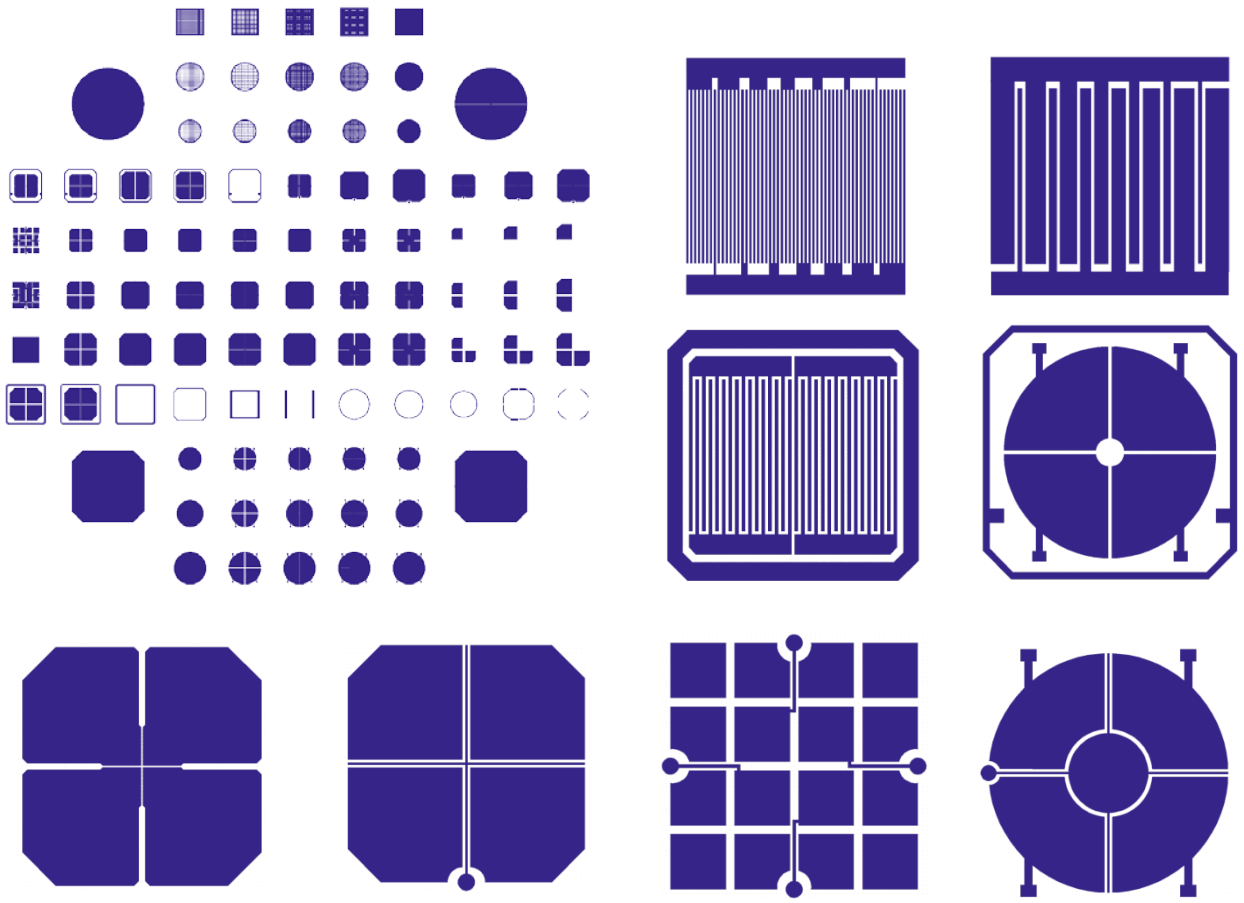

Figure 6 Photo masks and electrode patterns designed for diamond based electronics.

2.4 Charge transport in diamond

In a standard scheme of a diamond x-ray monitor, x-rays are absorbed at a depth determined by photon energy, exciting energetic electrons within the diamond. These electrons lose their energy through electron-electron scattering and excite electron-hole pairs. Under the applied bias, electrons and holes are separated, drift through the diamond and collected by contacts on both sides. So the current measured is proportional to the x-ray power absorbed. And this response to incident flux is linear over 11 orders of magnitude. [8, 31] Figure 8 gives an illustration of 2 scenarios which we normally encounter in our experiments. In the low energy scenario, x-ray power is absorbed and the charge carriers are created at the incident surface of the diamond. Depending on the type of bias applied, either type of charge carriers travels through the diamond and are collected by the contact. In the high energy scenario, x-ray goes all the way through the diamond and charge carriers are created in the bulk of the diamond and then collected in the biased contacts. The diamond attenuation length can be looked up in several x-ray data bases and a plot of attenuation length vs photon energy is given is Figure 7.[32]

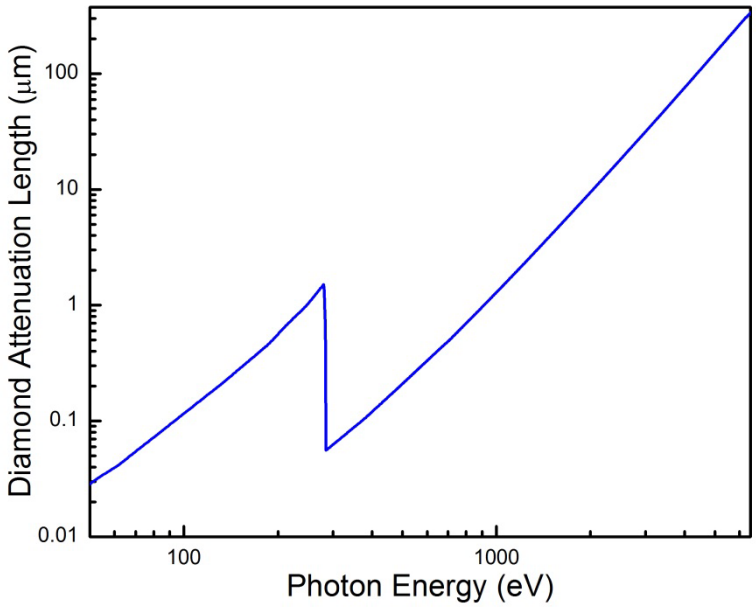

Figure 7 Diamond attenuation length vs photon energy from 50 eV to 6.5 keV.[32]

The first scenario is beneficial for studying the transport behavior of either electrons or holes. A detailed discussion of charge carrier transport behavior near diamond surface is presented in a recent paper[33] and in section 6, stating that the carrier loss due to diffusion into the contact is prominent under low electronic field in diamond. The second scenario is the most common scheme we encounter with the application of diamond x-ray monitors. Examples include the white beam positions monitors we designed and installed in Beamline X25, NSLS, operating at 5-20keV[21] and another diamond sensor tested at Beamline X23A, an x-ray absorption spectroscopy beamline which uses monochromatic beam ranging from 4.9keV to 30keV.[22]

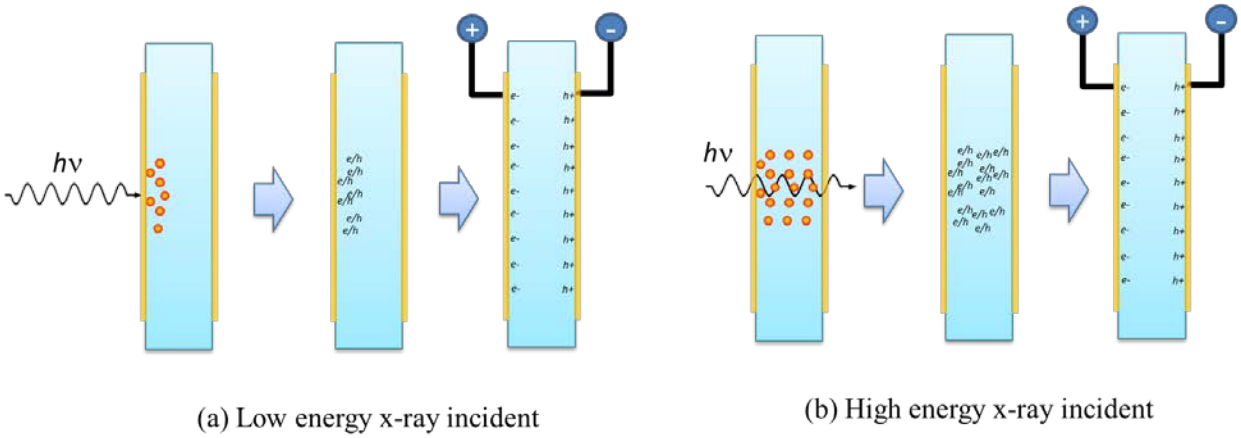

Figure 8 Charge transport in diamond with (a) Low energy photon and (b) high energy photon incident into diamond.

2.5 XBIC microscopy

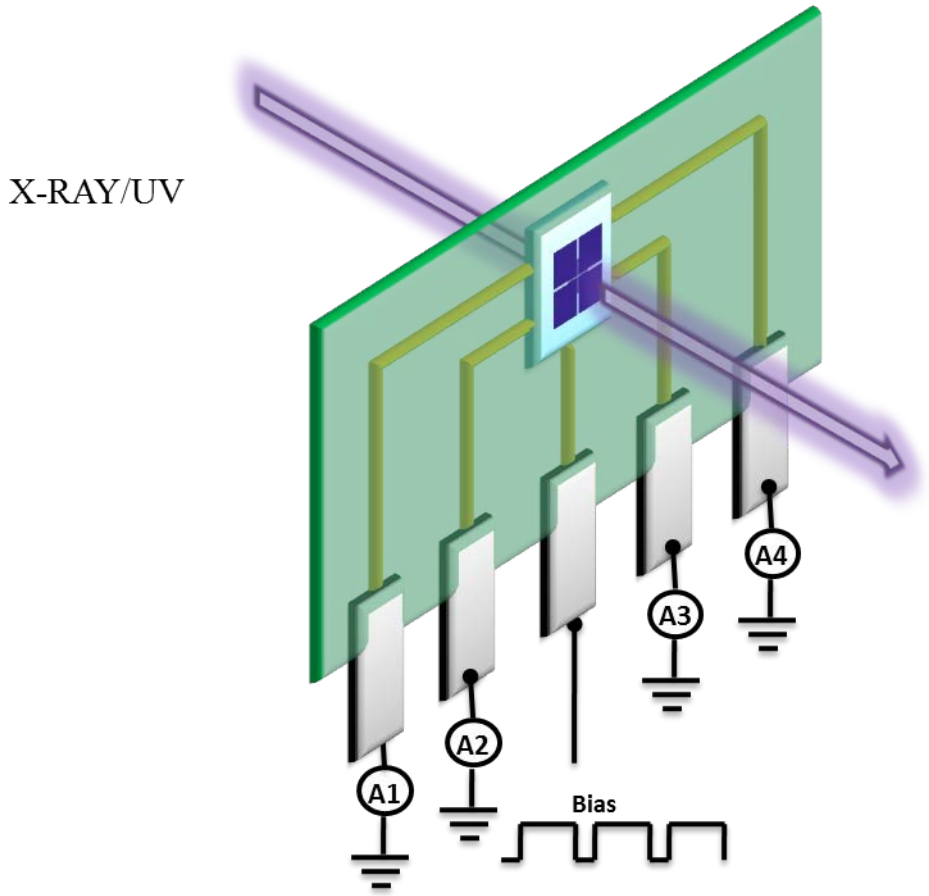

Figure 9 Schematic of diamond mounted onto a PCD circuit board with 4-channel output signal and one channel as applied bias with duty cycle set up. X-ray incident in the bias side of the diamond.

The x-ray beam induced current (XBIC) is a common measure of the overall device performance for our diamond detectors. A typical experimental scheme of testing a diamond detector in a beamline is shown in Figure 9, where the sample is mounted on a pre-designed circuit board, with one channel as bias and the other channels as output signal, and then on a precision X-Y stage motor. A current map can be obtained by raster scanning x-ray beam over the active region of the diamond sensor and a beam size as small as 5 μm with white beam incidence and 40~200 μm (beamsizes are adjusted according to beam flux at the testing energy to ensure distinguishable signal from background noise) for monochromatic beam can be used to diagnose local device response and position sensitivity.

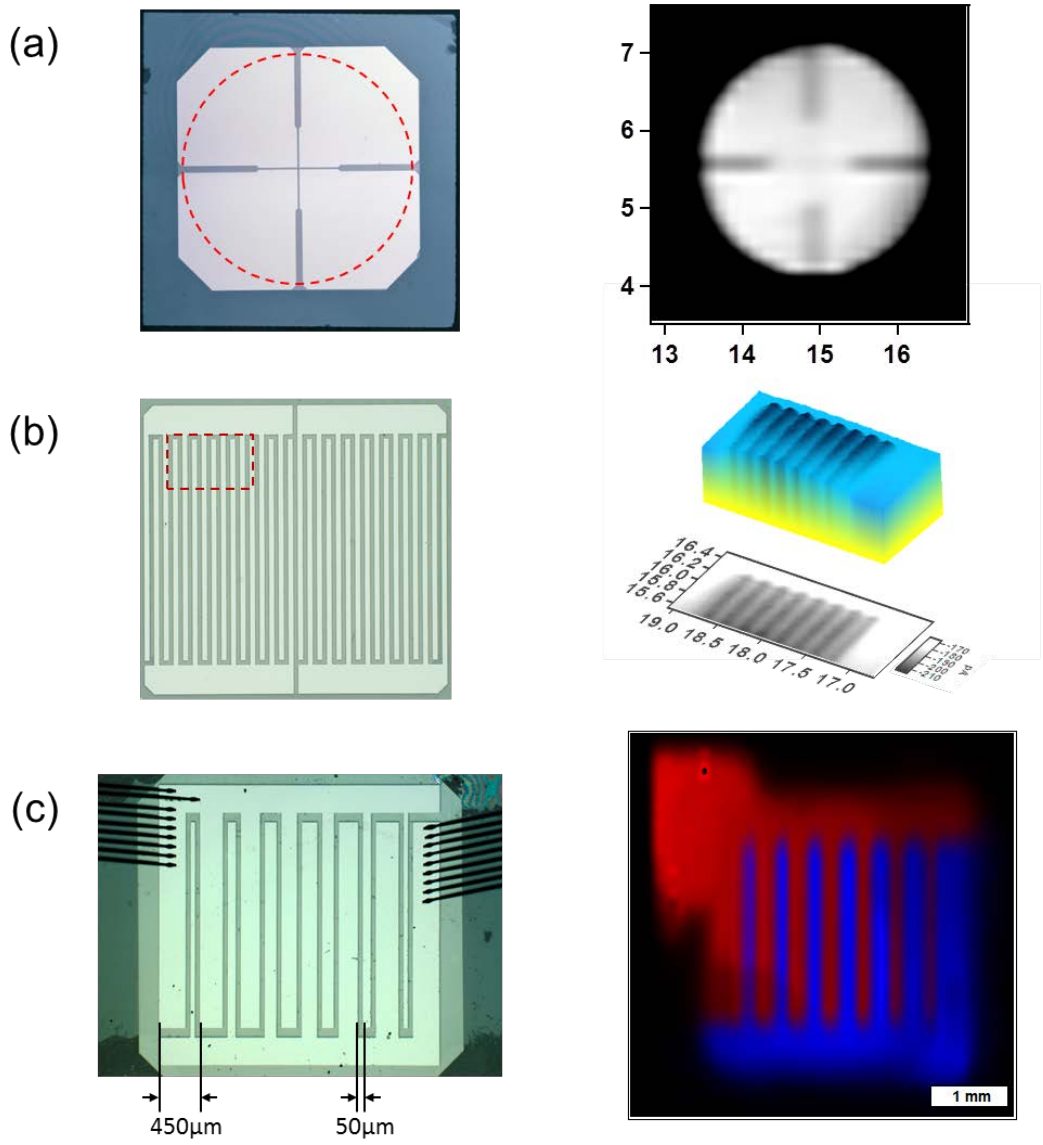

Figure 10 Examples of XBIC mapping for various electrode patterns. (a) quadrant pattern with 20µm streets. (b) Interdigitated finger patterns with even stripe size and spacing. (c) Interdigitated finger patterns with varied finger size.

Examples of XBIC mapping for various electrode patterns are shown in Figure 10. The quadrant pattern shown in Figure 10a is designed with 20µm streets in the central active area and extends to 80µm in the outer region. Interdigitated finger patterns with even and varied size and spacing are presented in Figure 10b and 10c. Current maps presented on the right side give examples of the frequently used mode and color scheme in the following sections.

2.6 Energy calibration

Previous work has come up with a simple model that well described the responsivity S of diamond monitors, which is expressed as

$$S = \frac{1}{W} e^{-\frac{t_M}{\lambda_M}} (1 - e^{-\frac{t_a}{\lambda_D}}) CE \qquad \textbf{Equation 1}$$

where W is the mean ionization energy of diamond (13.3 $\pm$ 0.5eV for these measurements). t_M and t_a are the thickness of the metal contact and the active thickness of the diamond. λ_D and λ_M are the photon energy dependent x-ray attenuation lengths of the diamond and the metal contact . CE function represents the collection efficiency of the device.

In order to evaluate the diamond detector response at different incident photon energies, the measured output current in diamond needs to be converted to responsivity by calibration with the incident x-ray power, e.g.

$$S_{\exp} = \frac{I_{diamond}}{P_{in}} \qquad \textbf{Equation 2}$$

Where $I_{diamond}$ is the measured current corrected by background and duty cycle, and P_{in} is the total power input into the diamond device. For device calibration, a Si detector is placed upstream to measure the input power. By fitting the experimental responsivity with the theory, we can obtain information such as mean ionization energy W, the thickness of the incident contact, the thickness of diamond, and most importantly, the collection efficiency of a device.

Energy calibration test is routine for our diamond detector measurements along with the current mapping and bias scan, using the same apparatus described in Figure 9.

2.7 Collection efficiency and pulsed biasing

If the charge carriers generated in the diamond are all collected through the contact (referred later as full collection), we consider the collection efficiency function CE=1. However, the collection efficiency can be decreased by several mechanisms. First mechanism is the carrier loss due to a competition between carrier drift and diffusion. After a charge carrier is generated, it will drift under applied bias and simultaneously diffuse isotropically.[20, 31] If carrier diffusion towards the incident electrode exceeds the drift mechanism, it will recombine in the metal and result in carrier loss.[33, 34] A simple approach to describe this carrier loss is to consider it as a layer of carbon that is absorbing the incident power but not contributing to the carrier generation, referred later as the dead carbon layer, for the reason that the carrier loss mechanism described above is exponentially dependent with the x-ray attenuation length in diamond. Therefore we can use the approximation of $CE = e^{-\frac{t_d}{\lambda_D}}$, where t_d is the thickness of the dead carbon layer and λ_D is the x-ray attenuation length of the diamond. Therefore Equation 1 can be modified as

$$S = \frac{1}{W} e^{-\frac{t_M}{\lambda_M}} e^{-\frac{t_d}{\lambda_D}} (1 - e^{-\frac{t_a}{\lambda_D}}) \qquad \textbf{Equation 3}$$

This model is later referred in the text as the dead diamond (DD) model.[34, 35]

A better and more physically correct approach to quantify this carrier loss is proposed as $CE = 1 - e^{-x/\beta}$, where x is the depth from the diamond surface and β is the characteristic recombination length of the carrier that is dependent of inner electric field in diamond. If this term is convolved with the exponential dependence of x-ray absorption, the responsivity can be expressed as

$$S = \frac{1}{W} e^{-\frac{t_M}{\lambda_M}} (1 - e^{-\frac{t_a}{\lambda_D}}) (\frac{1}{1 + \beta/\lambda_D}) \qquad \textbf{Equation 4}$$

where t_M, t_a, λ_D and λ_M stand for the same meaning as those are in Equation 1 and Equation 3.[33] This model is later referred in the text as the recombination length (RCL) model. The deduction of this equation will be described in detail in Section 6.

Another mechanism is the carrier loss due to crystal structural defects. Often times crystal defects such as growth dislocations, slip bands, impurities and inclusions will lead to either recombination of charge carriers inside the crystal (happens in natural diamond or optical grade diamond with high impurity level) or electron/hole trapped in the crystal and create local shut-down field (happens in diamond with low impurity level but relatively high dislocation density). In the latter case the applied bias will be compromised and results in sub-collection of charge carriers. [30]

Since structural defects are inevitable, a common approach to de-trap the carriers is to apply a bias with duty cycles (referred to as pulsed biasing). This way sample is periodically grounded to allow trapped carriers to recombine and turns off the shut-down field.

2.9 Schottky barrier

Schottky barrier is defined as the minimum work needs to be done by an electron to go through a metal-semiconductor junction. Figure 11 gives a schematic band diagram at diamond-metal interface where a Schottky barrier is formed after metal deposition. In order to calculate the Schottky barrier height, values like the difference between corelevels and Fermi level/valence band maximum (VBM) are needed. X-ray photoelectron spectroscopy is a useful tool to probe buried layers and study work function of a surface or an interface.[36, 37] Values obtained can be used to calculate the Schottky barrier height φ_B using Kraut's method[38] described in Equation 5.

$$\varphi_B = (E_{C1s}^{sample} - E_{MetalCore}^{sample}) + (E_{MetalCore}^{ref} - E_f^{ref}) - (E_{C1s}^{ref} - E_{VBM}^{ref}) \qquad \textbf{Equation 5}$$

Where E_f^{ref} is the Fermi level of the metal, E_{VBM}^{ref} is the valence-band maximum (VBM) of bulk diamond and $E_{MetalCore}^{sample}$ and E_{C1s}^{sample} are the metal core and carbon 1s of the sample respectively.

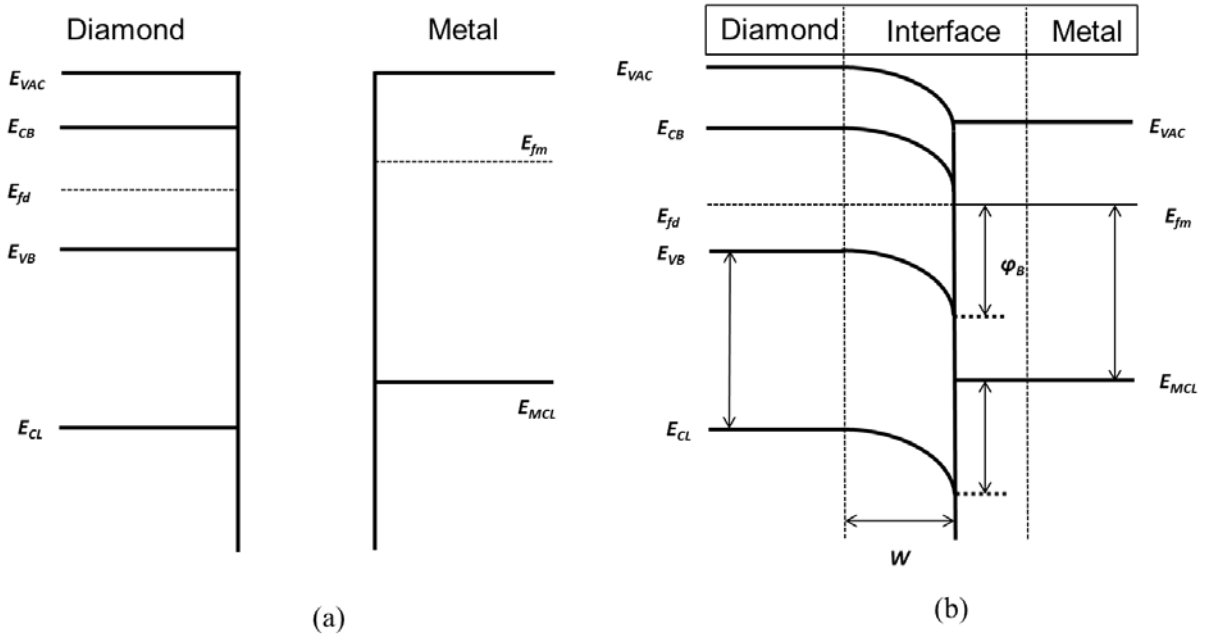

Figure 11 Schottky barrier formed at a diamond-metal interface: (a) band diagram for the diamond and metal before joining; (b) equilibrium band diagram at diamond-metal interface.

2.10 HAXPES

The accuracy of the barrier height determination depends greatly on the accuracy of the corelevel peak positions, the Fermi level and the VBM. In section 4, we compared the Schottky barrier height at the diamond-platinum interface before and after annealing as well as the unannealed silver-diamond interface using hard x-ray photoelectron spectroscopy (HAXPES). In section 8 we expand this method to study the core level and valence band structure of various boron-doped diamond samples prepared in different doping techniques. HAXPES measurements were performed at NIST beamline X24A at the NSLS with incident photon energy toned to be within 2.1~2.4keV. The beamline uses a Si (111) double crystal monochrometor to tune the incident photon energy and a hemispherical electron analyzer to collect emitted photoelectrons. The diamond plates are oriented towards the spectrometer normal (grazing incidence with respect to the x-ray beam) to provide the most bulk-sensitive measurements. Experiment set up at beamline X24A is shown in Figure 12.

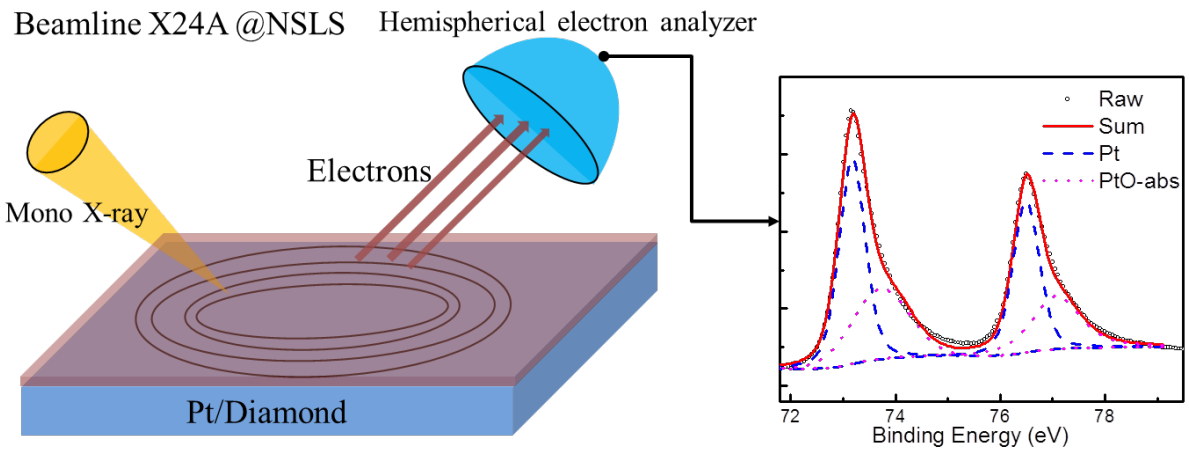

Figure 12 Experimental set-up for HAXPES measurement at beamline X24A, NSLS. Incident photon energy is tuned to be 2.1~2.4keV. The obtained spectrum is analyzed using XPSPeak4.1 and a typical corelevel spectrum with peak fitting is shown in the right plot.

Section 3 Structural defects induced photoconductive current in diamond

3.1 Introduction

Our observation and understanding of photoconductive current in diamond started in a test we employed at beamline X28, NSLS, a high flux beamline provides white beam x-ray with a flux intensity of 10^{16} photons/sec and a nominal photon energy of 10keV. When diamond was operated at the full flux of this beamline under DC bias, a higher current than its saturated level was detected. This current goes linearly with the applied voltage and can be recovered by running the device under a pulsed bias. 2D responsivity map shows that the higher current appears locally and is only within the area that was exposed to high flux x-ray beam. This test led us to the investigation of the mechanisms of this beam induced signal, which is referred using the term 'photoconductive gain' or 'photoconductive current'.[8, 35]

A proposed mechanism of the photoconductive gain we observed is described by Keister *et al*[39], stating that after electron-hole pairs are excited and charge carriers are separated, as we introduced in the last section, holes drift all the way through the diamond, while some of the electrons might be trapped by crystal defects as they drift through. These trapped electrons, especially the ones near the contact, have imaging holes accumulated near the interface. Hole injection will not be allowed if the contact is rectified (referred as Schottky contact). However, if the potential barrier is low enough (referred as ohmic contact), on average one hole will be injected into diamond for each trapped electron, keeping material charge neutral. Holes will continue to move through the device under applied bias and new holes will enter. This process will continue until electrons are naturalized. In general, the gain we measure is the hole lifetime divided by the hole transit time. This is the reason that the current goes linearly with the applied voltage.[8, 34, 40]

The observation of photoconductive current requires several conditions: one is that electrons to be trapped in diamond. We introduced in section 1 the possible trapping sites in a diamond single crystal. In this section diamond x-ray white beam topographs and corresponding photodiode current maps are compared and correlations are revealed between the growth dislocations in diamond and sites of photoconductive gain.

3.2 Experimental

Several electronic grade (~ppb nitrogen impurity) single crystal CVD diamonds with (100) surface normal and (110) side plane orientation are purchased from Element Six. Sample plates are laterally 4mm x 4mm with a nominal thickness of 500 μm. Atomic force microscopy (AFM) measurements show that the surface roughness of these samples are nominally within 2nm to 4nm.[41]

A CVD diamond grown on a HTHP substrate was cut along the <100> growth direction. Different from the industrial cut diamonds mentioned above, this sample has a surface plane of (110) and a side plane of (1-10), and the cut went all the way into the seed so a portion of the

high temperature high pressure(HTHP) diamond substrate remains in this diamond. Sample is 3mm x 2mm laterally and has a thickness of 500 μm.

White beam X-ray topography was performed at beamline X19C, NSLS, with the nearly parallel x-ray white beam incident on the sample in transmission geometry. Diamond sample is mounted in air on a precision motor and is rotated 20 degrees counterclockwise off its vertical axis to record the [$\bar{2}20$] and [111] reflections simultaneously, with an exposure time of 3~5 seconds. Reflection images are then enlarged by processing their negatives to achieve better resolution. For the vertical cut diamond, various reflections were recorded including [004]s, [220]s and [111]s with corresponding geometry. Due to its high dislocation density, grazing incidence is also used to record some of the topographs for this diamond.

Diamonds are then cleaned in an ultrasonic bath in acetone, ethanol and DI water, and then exposed under a UV lamp in air for 4~6 hours for each side respectively to further clean the diamond and prepare an oxygen terminated surface, which we believe plays a crucial role in maintaining a valid Schottky contact on diamond. The investigation regarding oxygen termination and the Schottky barrier at diamond-metal interface will be discussed in the next section. Platinum contacts of ~30nm thick are sputter coated onto both sides of each diamond over a 3mm x 3mm area on the (100) surface diamonds and 2mm x 1.5mm Pt layers of the same thickness are sputtered onto both sides of the vertical cut diamond.

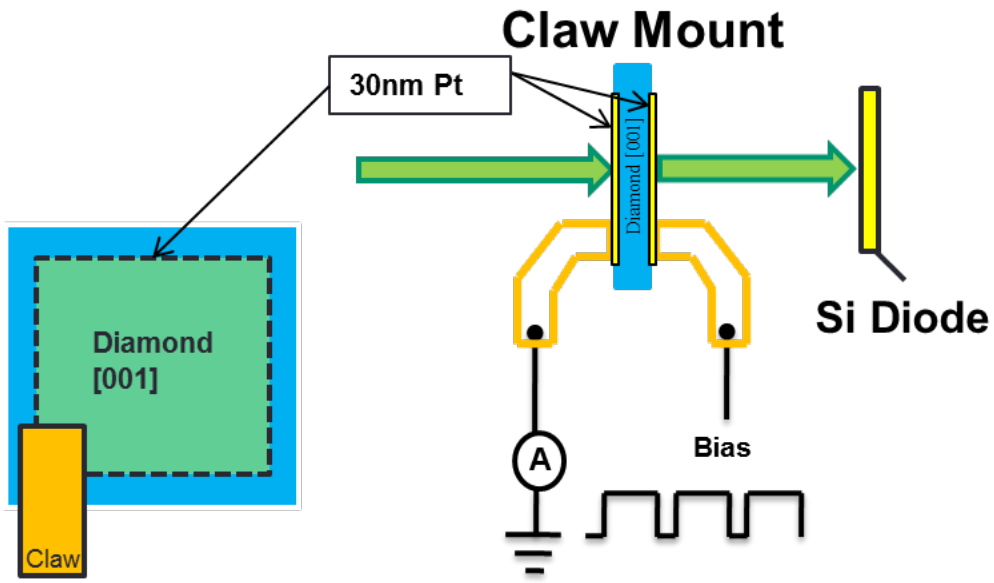

Figure 13 Schematics showing the apparatus of the 2D resposivity mapping

Samples were then mounted on a precision motor in various beamlines by a holder consists of 2 copper claws holding the diamond in place and making electric connections to the platinum contacts. Two dimensional responsivity maps are then obtained by raster scanning X-ray beam over a planar diamond active area and plotting the current at each coordination. Figure

13 gives an idea of the apparatus used this measurement. Beam size and mapping step size are adjusted according to the intensity of incident x-rays at different beamlines to ensure the distinguishable signal from the background noise, ranging from 40 microns to 200 microns in diameter.

A bias is placed on the X-ray incident side and the current is measured on the opposite side with a Keithley Electrometer, model number 6514. Typically a bias of ±100V is used, which supplies an electric field of 0.2V/μm and is well above diode saturation where full charge collection is achieved for these electronic grade high quality CVD diamonds. For the vertical cut diamond, a much higher electric field is needed to achieve full collection due to its crystal quality. By using an x-y translation stage, the sample is raster scanned in the X-ray beam. Two dimensional responsivity maps are calibrated using a silicon photodiode placed several inches downstream of the diamond sample. Contrast can be seen in the silicon photodiode signal due to X-ray photon loss in the diamond. Though small, the photon loss provides contrast outlining the diamond position. This is important to allow for proper alignment of the 2D responsivity maps with the X-ray topographs.

To study the effect of annealing, several as-deposited Pt samples were heated in a customized chamber at beamline X20C at the NSLS in a purified He atmosphere up to 600 °C at a rate of 3°C/sec. X-ray diffraction (XRD) spectra were collected for both before and after annealing. Similar measurements were then performed after samples being annealed.

3.3 Results and discussion

The recorded x-ray topographs are shown in Figure 14 with several prominent features circled and magnified. It can be noticed that at the corners of each image there are several broad dark bands running diagonally, mostly emanating from the crystal edges and running towards the interior. These features correspond to slip bands comprising dislocation pile-ups. Another noticeable feature on these images are small configurations of slip bands with appear to be emanating from inclusions/secondary phases (Figure 14). Dislocations are originated due to relaxation around these point defects and propagate in a way that Burger's vector is preserved to be 0. Inclusions in crystals are typically introduced during the growth process, from crucible materials or impurities in the growth chamber, formed both inside single crystal grains and along structural defects such as grain boundaries.[42] Both metallic and silicate phases of inclusions can be formed inside the diamond during synthesis process.[27]

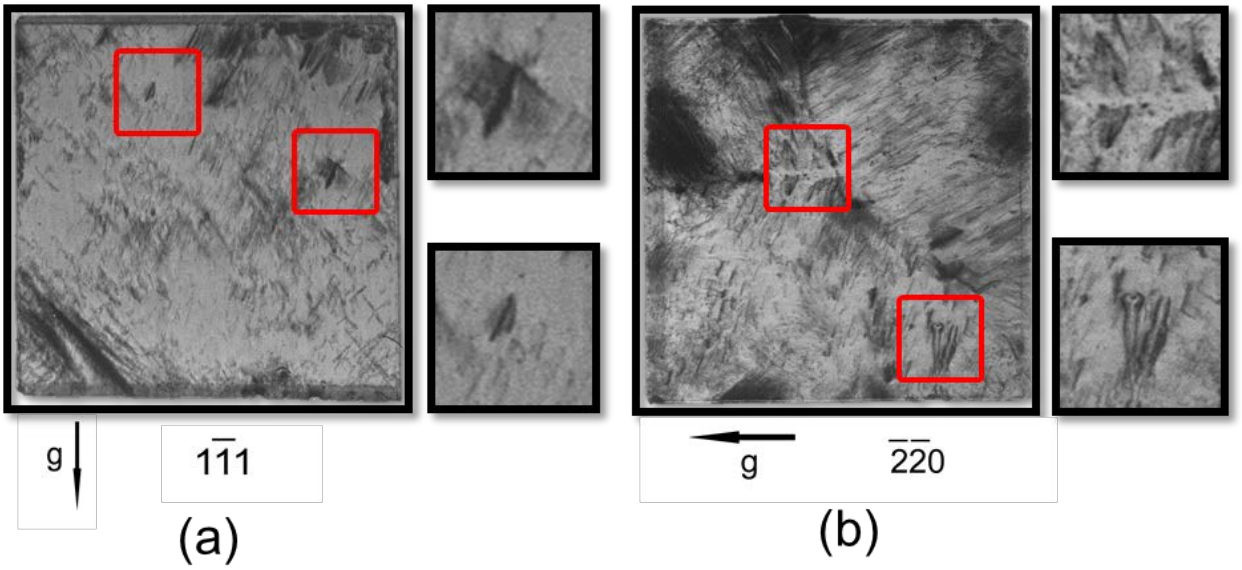

Figure 14 Topographs recorded from (a) sample A and (b) sample B. Features magnified indicating dislocation bundles that are originated from an inclusion or secondary phases.

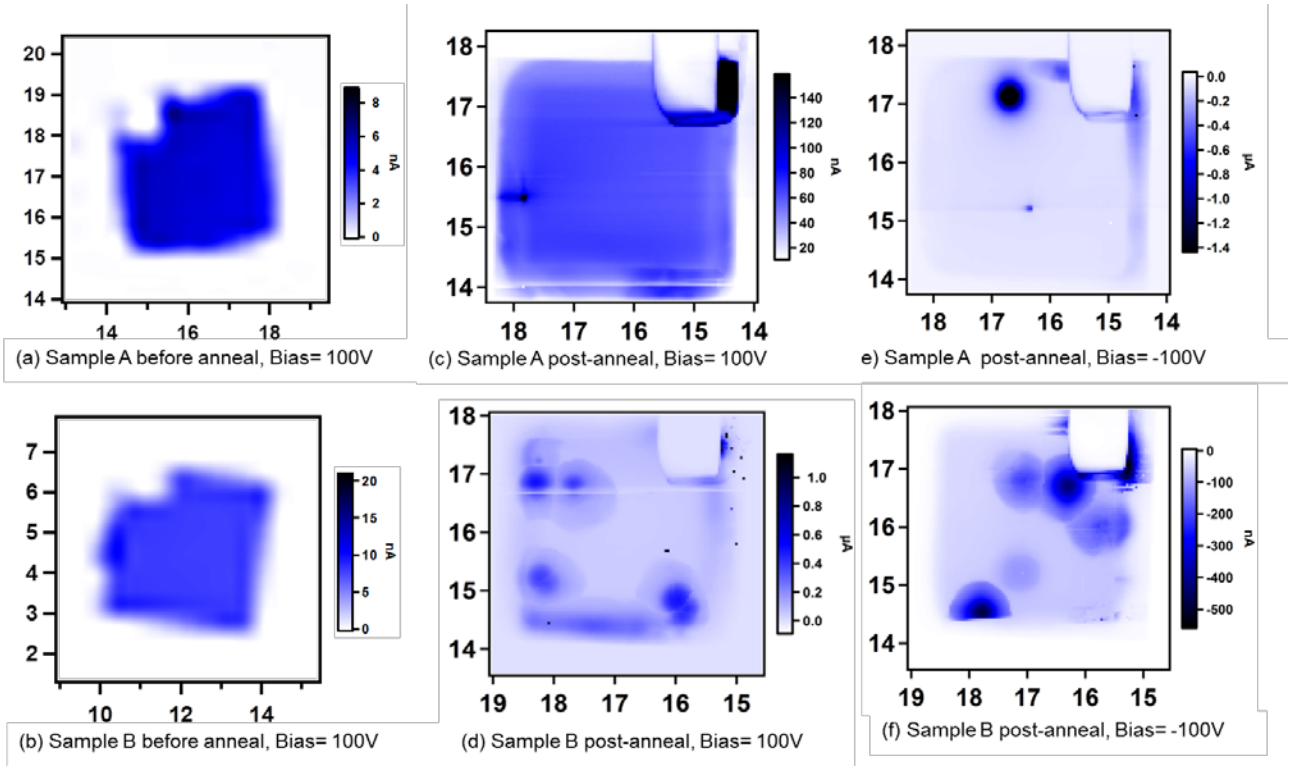

Figure 15 Comparison between diamond response maps (a), (b) prior and (c), (d), (e), (f) post annealing treatment. Maps are shown in in different biases to show bias dependence of photoconductive regions.

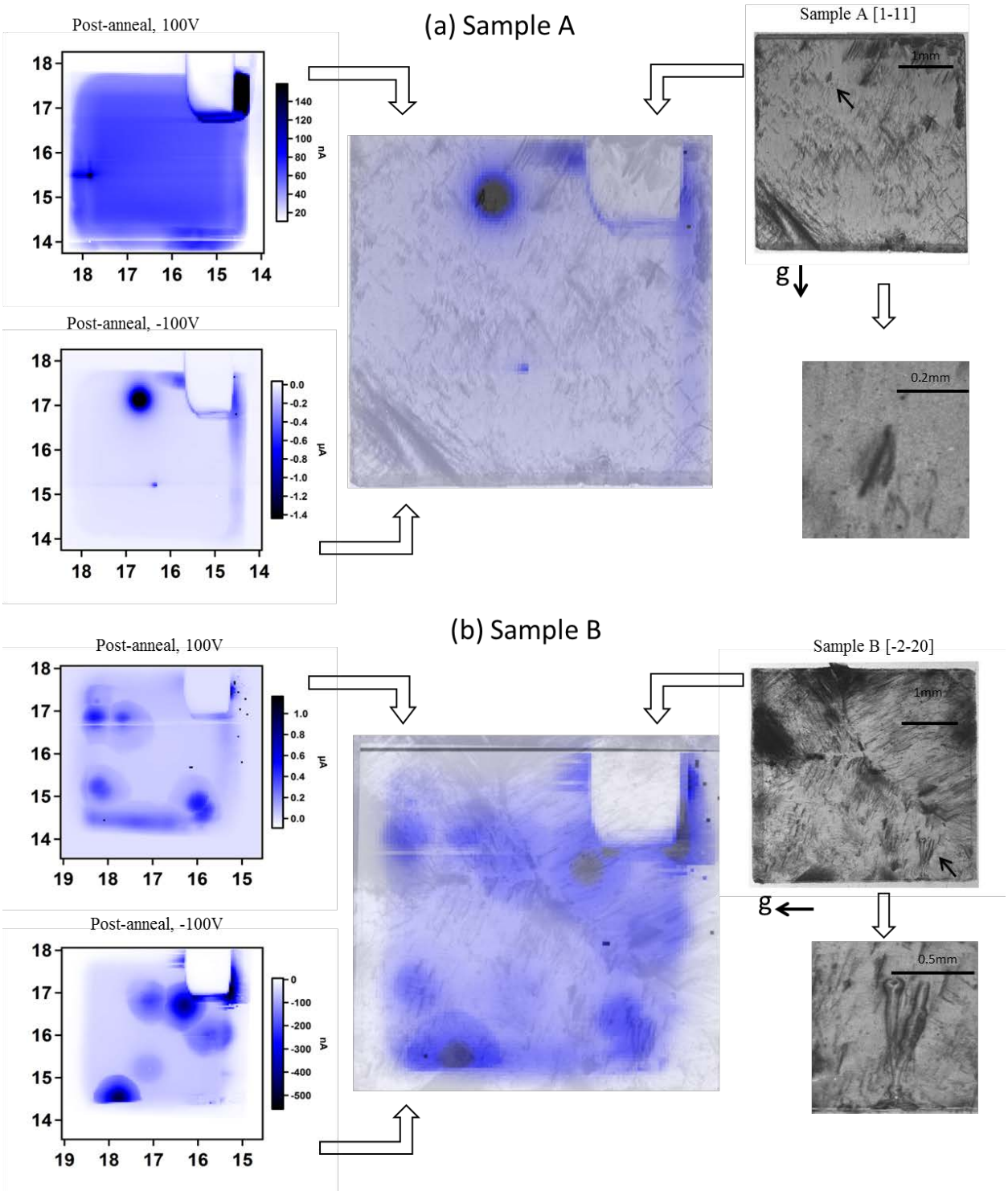

Figure 16 Topographs and responsivity maps overlaid to show correlation of photoconductive regions with structural defects for sample A and B. See text for detailed analysis.

Figure 15 gives an example of the comparison between diamond response maps prior and post annealing treatment. A uniform, featureless response map is shown in Figure 15a and 15b at opposite polarities, where the expected diode response is seen over the entire metalized region. In the post anneal case, however, diamond response map exhibits prominent regions which we believe is due to photoconductive current, as is shown in Figure 15c, 15d, 15e and 15f. From the comparison it is easy to tell that the presence of these photoconductive regions is bias dependent, e.g. the locations vary depending on whether holes or electrons are collected.[8] By annealing, the oxygen is desorbed or migrates into the platinum electrode and the Schottky barrier at the contact is either greatly reduced or removed completely, allowing charge injection. [30]

The responsivity maps are overlaid with the topographs, see Figure 16. The comparison between the two reveals that where there is a photoconductive region, there is a structural defect in the topographs. However, every inclusion does not appear to be cause photoconductive gain. We have also physically flipped the diamond so that the incident side becomes the exiting side -- this effectively changes the surface at which holes or electrons are collected. In this case the photoconductive regions first observed under positive bias would now be observed in negative bias and vice versa. Such observation would naturally lead to the conclusion that the depth of the inclusion determines whether it results in photoconductive gain, or say, electronically active. More specifically, inclusions near the hole-injecting surface will result in photoconductive gain. This explanation does not exclude the possibility that electrons are trapped elsewhere in the diamond, however, the electric field generated by these trapped electrons does not cause holes injection. Possibilities include small amounts of trapping at dislocations or impurities as well as inclusion buried deeper toward the center of the diamond.

The vertically cut sample is also mapped in the similar way in addition to our measurements discussed above. Figure 17 contains x-ray topographs of this sample in both transmission and reflection geometry. In these topographs, the interface between the CVD diamond and the HPHT diamond substrate is distinct, and the higher dislocation density in the CVD diamond can be noticed. While most of the dislocations are growing from the interface, some of the dislocation bundles are originated in the area above the substrate inside the crystal. Contrast discontinuity marked by arrows, indicates the origination of bundles of dislocations.

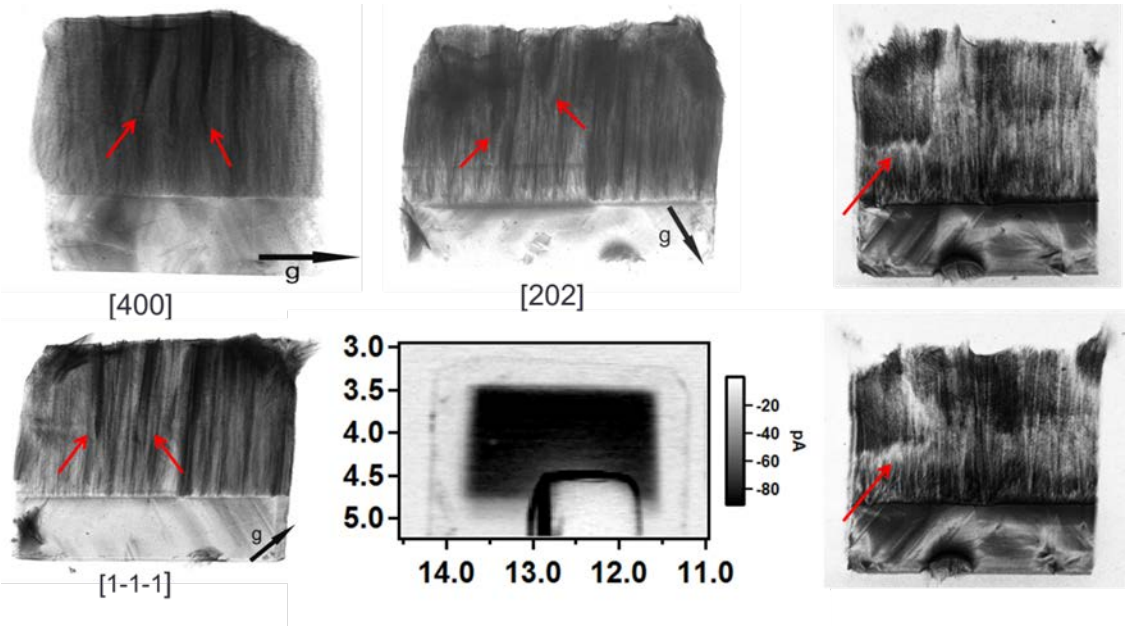

Figure 17 Vertical-cut Sample – Surface plane (110); Side plane:hkl:(1-10). Arrows are indications of dislocation bundles originated inside the crystal instead of coming from the substrate-diamond interface.

The responsivity map of this vertical cut diamond shown in Figure 17 gives a distinct separation between the CVD diamond and the substrate as well. Despite the lower density of dislocations, the substrate shows a poor response during the measurement. While the CVD diamond the gives a higher response than the substrate, the overall performance of this diamond as a diode is poorer than the ones previously measured. It can be noticed that although this diamond has a higher density of dislocation, no photoconductive gain is observed during mapping, which supports the idea we mentioned above that not all the structural defects are electronically active.

3.4 Conclusion

Regions of photoconductive gain are observed to correlate with inclusions in single crystal electronic grade diamond. Photoconductive gain is only observed for near-surface inclusions in diamond X-ray photodiodes created with injecting contacts. The adverse effect of near surface inclusions can be avoided with the creation of robust blocking contacts or by avoidance of annealing the diamond, i.e. for use in low flux operation where the diamond will not be heated. The nature of the inclusions is not known and they are identified only by the three-dimensional strain fields that appear in the topographs. There is a range of possibilities for their origin including voids, foreign material to non-diamond carbon.

Section 4 Annealing dependence of diamond-metal Schottky barrier heights probed by hard x-ray photoelectron spectroscopy

4.1 Introduction

In section 3 we have introduced the working principles of a simple diamond based detector as well as the observation of photoconductive current. We have suggested the correlation between these photoconductive spots and structural defects in diamond crystal.[41] However, there are two requirements for hole injection to happen: one is that the charge carrier trapping (electrons in this case) needs to happen close to the diamond surface, the other is that the Schottky barrier at diamond-metal interface is low enough so that holes from the metal contact can overcome. The typical preparation of the metal contact involves a prior oxygen termination of diamond surface and subsequent metallization to provide blocking contact (some refer as Schottky contact). It is suspected that post-deposition thermal annealing to temperatures above 600℃ can compromise the blocking nature of the contact and introduce photoconductive gain to the device by lowering the potential barrier at the diamond-metal interface. Such observation indicates that for a diamond beamline monitor with metal contacts to work properly under high-flux, high-heat load environment, careful thermal management is needed.

It is reported that non carbide-forming metallic contact such as platinum, along with prior oxygen termination, provides better blocking contact for the device.[35] The silver contact is featureless over a photon energy range of 4.5~25keV, which is beneficial for x-ray fluorescence measurements.[32] However for the diamond-silver interface (oxygen terminated), the blocking effect is observed to be much weaker, which might indicate a lower Schottky barrier height than diamond-platinum interface.

To address this problem a fundamental understanding of the Schottky barrier height and the modification after annealing are needed. There have been several works on studying the Schottky barrier heights of different metals on diamond, primarily using ultra violet photoelectron spectroscopy.[43, 44] This technique suffers from the inherent surface sensitivity issue and hence great care has to be taken for surface cleaning. Furthermore, during surface treatment extreme care must be taken to prevent any treatment from pinning the Fermi level.

In this section, we compared the Schottky barrier height at the diamond-platinum interface before and after annealing as well as the unannealed silver-diamond interface using hard x-ray photoelectron spectroscopy (HAXPES). Here we used the well-known Kraut's method for measuring the band offsets.[38] This method assumes that the energy separation between the valence-band maximum (VBM) and the core levels of the substrate remains unchanged after the metal deposition. The use of hard x-rays gives us the added advantage of probing buried layers.[36, 37] Thus we can simplify our measurement by directly measuring the semiconductor-metal interface.

4.2 Experimental

Platinum and silver were sputtered onto 4mm×4mm electronic grade (<5ppb N2) single crystal diamond plates purchased from Element Six, with a nominal thickness of 500μm and

(100) surface normal. Prior to the deposition, the diamond substrates were cleaned and oxygen terminated. For comparison, the metal layers were deposited to different thicknesses. To study the effect of annealing, as-deposited Pt samples (5nm and 30nm thick Pt on diamond surface) were heated in a customized chamber at beamline X20C at the NSLS in a purified He atmosphere to 600 °C at a rate of 3°C/sec. X-ray diffraction (XRD) spectra were collected for both before and after annealing. For 2D response map measurements, platinum was deposited to 30 nm on both sides of the diamond plate and the beam diameter was adjusted according to the intensity of incident x-ray to ensure a distinguishable signal from the background noise, ranging from 40 to 200μm. Typically a bias of ±100V is used which is well above diode saturation where full charge collection is achieved. Responsivity maps were calibrated using a silicon photodiode placed several inches downstream of the diamond sample. HAXPES measurements were collected at NIST beamline X24A at the NSLS with an incident photon energy set at 2139 eV. The beamline uses a Si (111) double crystal monochromator to tune the incident photon energy and a hemispherical electron analyzer to collect emitted photoelectrons. The diamond plates are oriented towards the spectrometer normal (grazing incidence with respect to the x-ray beam) to provide the most bulk-sensitive measurements.

4.3 Results and discussion

Prior to annealing, the responsivity is flat and featureless, see Figure 1a. The expected diode response is observed over the entire metalized region. However, after the sample has been annealed, small prominent regions exhibiting photoconductive gain appear in the responsivity map (Figure 18b). Schematic diagram of charge injection is shown alongside with the responsivity map in both cases. The presence of these photoconductive regions depends on the polarity of the applied bias (whether holes or electrons are collected). Annealing modifies the contact either by desorption of oxygen or by migration of the oxygen into the platinum electrode and lowering the Schottky barrier, which is demonstrated by the following measurements.[41]

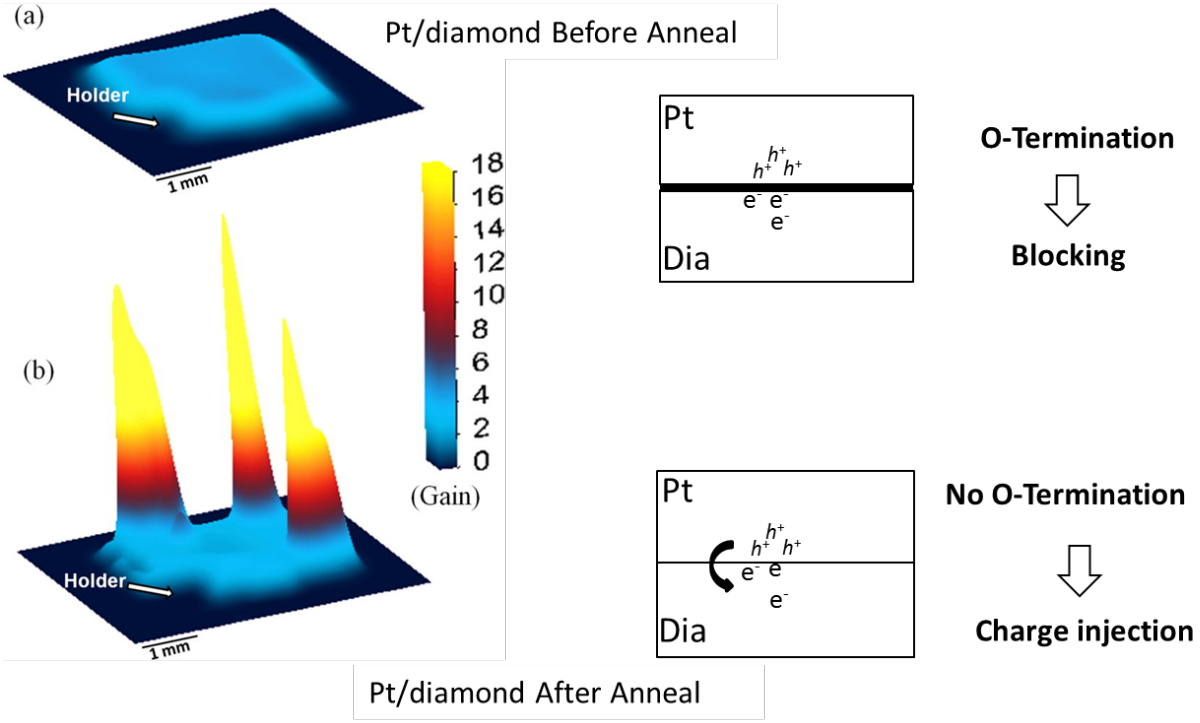

Figure 18 Diamond response (normalized by upstream monitor signal) (a) before and (b) after anneal. A bias voltage of -100V was applied for both measurements. Schematic diagram of charge injection is shown alongside with the responsivity map in both cases.

The XPS spectra of the Pt4f region and the corresponding C1s core-levels from the different thickness and annealed samples are illustrated in Figure 19a. The spectrum shows the characteristics spin doublet with a spin-orbit splitting of about 3.3 eV. The low binding energy of the Pt4f peak makes this measurement bulk sensitive at this photon energy. Careful inspection of the Pt4f peaks from the sample with 5 nm thick platinum reveals a distinct asymmetric peak shape towards higher binding energy. This asymmetry is attributed to some form of oxygen desorption/platinum oxides at the surface.[45, 46] As expected, this asymmetry becomes less prominent when the metal layer thickness increases. The C1s spectrum from the substrate is also shown in the same figure 2a. The reference C1s spectrum has one symmetric sharp peak represents the C1s of bulk, while the C1s spectrum from all the metalized carbon surfaces present 2 peaks with one sharp peak at higher binding energy assigned to the bulk and the peak at lower binding energy coming from non-diamond carbon contamination, possibly from prior sample treatment. The peak separation is measured to be 1.5eV, which is much larger than the reported separation of 0.9eV between and hybrids[47, 48] or 0.6eV between diamond and graphite.[49, 50] Assignment of the C features was confirmed by changing the take-off angle (between sample normal and detector) to lower angles to provide a more surface sensitive measurement. With increased surface sensitivity, the intensity of the lower binding energy component increases significantly (not shown), demonstrating that this feature is located on the surface and the high binding energy component is sub-surface. A 30nm Pt layer grown on a diamond plate was used as reference for platinum core-levels and the Fermi level.

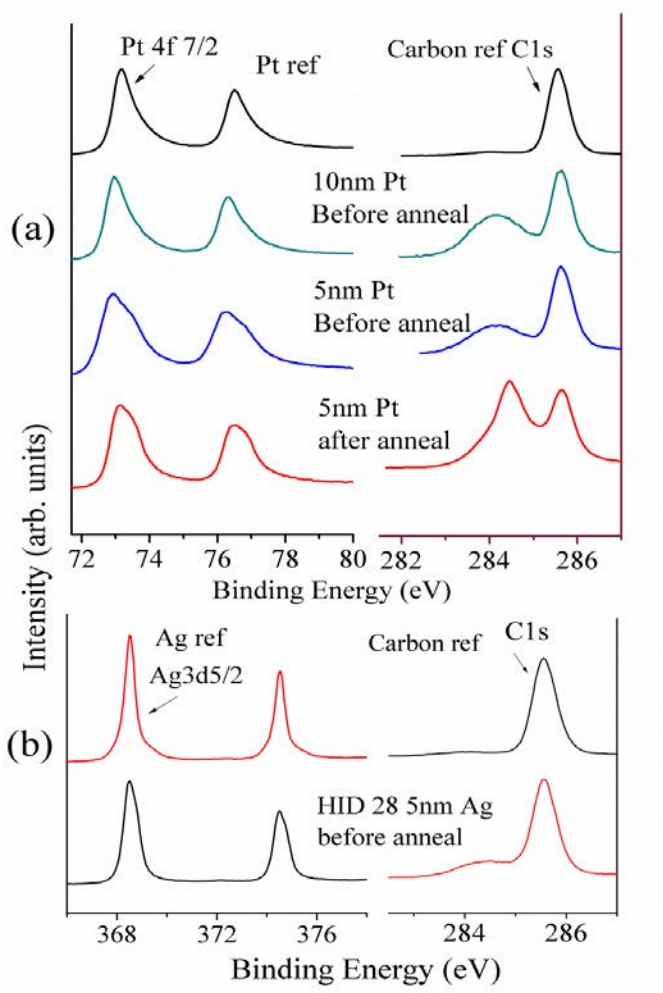

Figure 19 (a) HAXPES spectrum of Pt4f, (b): Ag3d (bottom left) and C1s core-levels (right). Arrows indicate the peaks used for band alignment. The core lines are referenced to the Fermi level of Au.

Our previous studies with Ag contacts on both oxygen- and bulk-terminated diamond showed regions of photoconductive gain. It was postulated that the oxygen termination did not provide a sufficient blocking contact with Ag to resist hole injection.[35, 41] To confirm this, a diamond was prepared with oxygen termination in a manner similar to that described previously, followed by sputter deposition of 5nm of Ag. Figure 19b shows the HAXPES spectra from Ag deposited on diamond. The Ag spectra show the $3d_{5/2}$ and the $3d_{3/2}$ doublet with a peak separation of about 6 eV. A piece of Ag foil is used as reference and the peak position of $Ag3d_{5/2}$ is used for later barrier calculations.

To precisely determine the peak positions, the measured spectra were analyzed using the program XPSPeak4.1. Prior to fitting the spectra were background corrected with a non-linear Shirley function.[51] Platinum 4f peaks were fit using mixed Gaussian- Lorentzian functions with a ratio of 0.3. After fitting, the peak area ratio of $4f_{5/2}$ and $4f_{7/2}$ is 1.3, close to a theoretical value of

1.33.[52] To obtain the Schottky barrier height of the diamond-metal we used Kraut's method described in Equation 5.[38]

The accuracy of the barrier height determination depends greatly on the accuracy of the peak position, the Fermi level and the VBM. The peak position can be measured accurately by fitting the obtained spectrum. However the same cannot be said about the position of VBM. For metallic samples (such as Pt and Ag) the location of an inflection point in the photoemission spectrum is the Fermi level (data not shown). While this method works well for metals, it is not appropriate for semiconductors. Significant numbers of studies of semiconductors have employed methods such as extrapolating the tangent line to the leading edge of the valence-band spectrum to zero intensity to define the VBM. However, this procedure introduces significant uncertainty in the position of the VBM, because the detailed structure of the VBM is quite complicated.

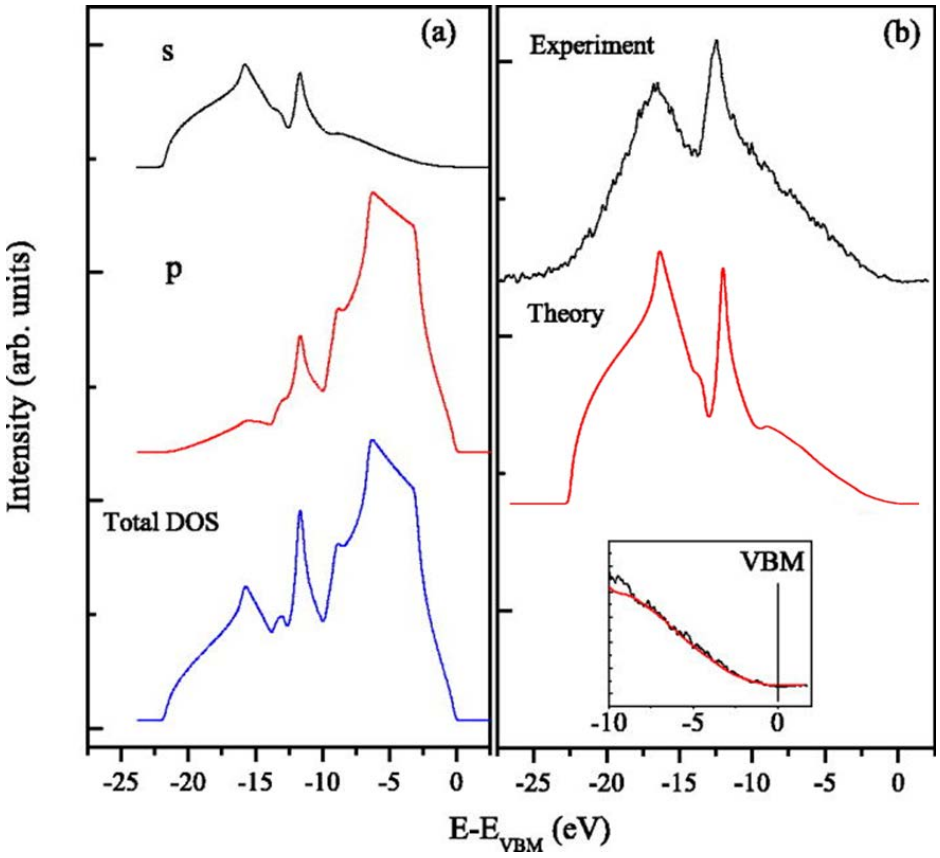

Figure 20 (a) Calculated partial and total DOS for diamond. (b) Colored curve is cross section applied total DOS for diamond at an incident photon energy of 2.15keV, convoluted with Gaussian (FWHM ω=0.26 eV). Dark curve indicates experimental valence-band structure of single crystal diamond. The feature peaks and VBM position are marked by dotted lines.

Following the work of Kraut et al[38], we determined the position of the VBM by theoretically calculating the density of states (DOS) using first-principles and then convolving with a Gaussian to account for experimental broadening.[43] Figure 20a shows the angular

momentum partial DOS (s and p states) as well as the total DOS calculated for diamond (100). A closer inspection of the experimental valence band (shown in figure 20b) however, shows a drastically different structure. This is due to the fact that photoelectron intensity is not proportional directly to the DOS, but rather the sum of the individual angular momentum resolved partial density of states, weighted by the photoionization cross sections. Thus to compare the theory and experiment, we have followed the discussion of reference[53] and constructed theoretical VB curves as the cross section weighted sum of angular momentum resolved partial DOS. The atomic cross sections were obtained from reference.[54] Figure 3b shows the comparison between theoretical and experimental VB for a clean diamond surface. It must be mentioned that prior to data collection, the diamond surface was cleaned in situ to remove surface graphite like carbon. To account for instrumental broadening, reconstructed theoretical data was convolved with Gaussian curve $\omega = 0.26$ eV full width at half maximum and the result resembles the experimental VB curve quite closely (Figure 20b). Using the measured peak position, Fermi level of the metals and the VBM of bulk diamond we calculated the Schottky barrier height and the results are listed in TABLE 3.

Table 2 Schottky Barrier height calculation for various diamond-metal interfaces.

Sample	$\Delta_{corelevel}$ [a] (eV)	φ_B [b] (eV)
10 nm Pt before anneal	215.27	3.2
5 nm Pt before anneal	215.31	3.24
5nm Pt after anneal	215.07	3.0
5nm Ag before anneal	82.21	2.77

[a] $\Delta_{corelevel}$ is $E_{C1s}^{Pt/Dia} - E_{Pt4f_{7/2}}^{Pt/Dia}$ for Pt on diamond and $E_{Ag3d_{5/2}}^{Ag/Dia} - E_{C1s}^{Ag/Dia}$ for Ag on diamond.

[b] φ_B is calculated using $(E_{C1s}^{Dia} - E_{VBM}^{Dia})$=283.54eV, $E_{Pt4f_{7/2}}^{Pt} - E_f^{Pt}$ =71.47eV, $E_{Ag3d_{5/2}}^{Ag} - E_f^{Ag}$ =368.52eV.

It must be noted that the barrier height of the Pt-diamond interface before annealing is higher than the barrier height after annealing, showing a difference of ~0.2eV; whereas there is no difference in barrier height for un-annealed diamond with different Pt thicknesses. This result can be interpreted as the degradation of the blocking contact during the process of heat treatment up to 600 °C corresponding to the known oxygen desorption temperature.[46] This difference is close to an observed chemical shift (towards higher binding energy) from clean Pt to Pt heated up to 300°C in O_2,[46] which might be attributed to the lowered Schottky barrier in our measurement. The lowered barrier will lead to an increased probability for charge carriers travelling through the diamond-metal interface[34]. In this case, such change in barrier height agrees with the previous diamond responsivity measurements that higher photoconductive gain was observed for diamond detectors after the annealing process.[35, 41] We note that a change in

texture due to annealing was observed in the Bragg-Brentano XRD measurement for both 30nm and 5nm Pt coatings. Both coatings had a (111) surface texture when sputtered. In both post-anneal XRD curves the Pt (111) and Pt (200) phase were sharpened and the intensity of the Pt (200) peak was increased; in the 30 nm case the (111) peak is two orders of magnitude stronger than the (200), while for the 5 nm film post anneal they are comparable in intensity. As it is understood that such change in texture will not affect the Pt 4f binding energy,[46, 55] the previous interpretation of the lowered barrier height remains valid. For the silver contact, the calculated Schottky barrier is lower than that of diamond-platinum interface both before and after annealing, which also agrees with the observation for diamond detectors using silver as a contact material.[35]

4.4 Conclusion

The barrier height of the diamond-platinum interface decreases by ~0.2eV after thermal annealing, which suggests that annealing is a feasible cause of increased photoconductive gain observed for diamond devices under similar treatment in prior investigations. The Schottky barrier (and blocking nature) at the diamond-metal interface plays a central role in maintaining a device free of photoconductive gain. A barrier height decrease of ~0.2eV is sufficient to compromise the oxygen termination in a diamond-platinum contact. The barrier height is independent of the thickness of the contact. It is also demonstrated that the diamond-platinum interface provides a higher Schottky barrier and therefore a better blocking contact than the silver contact. Even with oxygen termination, the Schottky barrier in the diamond-silver contact is not sufficient to eliminate the observation of photoconductive gain.

Section 5 Thin diamond x-ray position monitor

5.1 Introduction

In order to build an inline device such as x-ray beam position monitor, to provide quantitative and simultaneous information of beam position, flux and timing, certain factors like device absorption, signal loss and collection efficiency need be accounted for calibration. While for applications such as the white beam position monitors installed in beamline X25 and the flux monitor in beamline X23A,[21, 22] the devices are operated at a photon energy range where the absorption of the device is negligible. However, for the applications in the soft x-ray range, a diamond device 0.5 mm thick will lead to significant signal loss.[32] Therefore, reducing diamond thickness becomes a feasible approach to adapt our device to soft x-ray applications.

In the previous sections we have addressed the correlation between crystal structural defects in bulk diamond and photoconductive current which might compromise device performance.[41] Despite the fast development of CVD diamond growth industry, structural defects are still inevitable with current technology. We have compared the x-ray topographs of diamond before and after slicing and polishing (Figure 21). The original thickness of the diamond shown in this figure is ~ 0.5 mm, while after slicing the diamond thickness was reduced to 70μm. Results indicated that thinner diamond has less density of dislocations and gives less inclusion-like defects and therefore becomes a better candidate of our device.

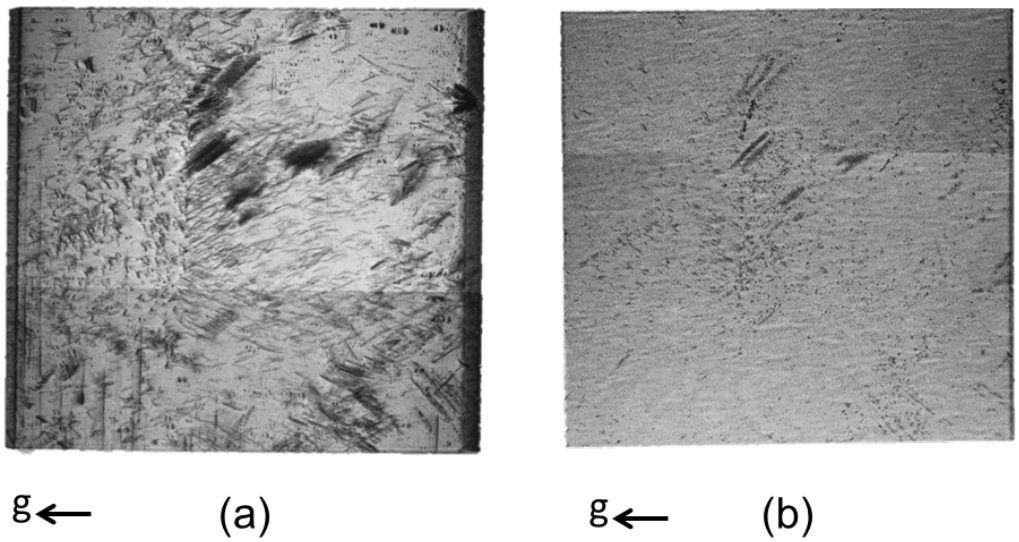

Figure 21 White beam x-ray topographs of CVD diamond (a) before and (b) after slicing and polishing.

5.2 Experimental

The diamonds used in this test are originally from a 4mm by 4mm electronic grade (<5 ppb N2) CVD single crystal diamond purchased from Element Six, which was laser cut in

half and mechanically polished down to two diamond plates with nominal thickness of 30 microns. The laser cutting and polishing was done by Delaware Diamond Knives. Sliced diamond plates retained surface plane as (100) and side plane as (110).

White beam x-ray topography at Beamline X19C, NSLS has been used to characterize structural defects for the diamonds with similar experimental set up described in section 2. Aluminium filter was applied in the beam path to reduce incident beam intensity and minimize the thermal oscillation of the sample. Sample was then cleaned and prepared with oxygen termination on both sides. One diamond was metalized with a quadrant-patterned Pt layer as front electrode and a solid Pt layer as back contact in a plasma sputter system with a programed sputter thickness of 10nm. The other diamond was treated similarly but was coated with sliver contact because for x-ray florescence applications sliver is featureless within the needed energy range.[32]

The metalized samples were then mounted on pre-designed circuit boards using conductive epoxy (shown in Figure 22), and the quadrant pads in the front are connected using aluminum wire bonds. Bias scan, 2D responsivity mapping at selected photon energies and energy calibration for this detector were performed at beamline U3C and X8A covering a photon energy range of 0.1keV to 6.5 keV. Detectors were mounted in the end station with base vacumm of 10^-7 Torr, with quadrant side (signal collecting channel) facing incoming beam, while the bias was applied on the back contact at the exit side of the beam. In order to ensure full collection, various duty cycles were applied for different energy ranges.

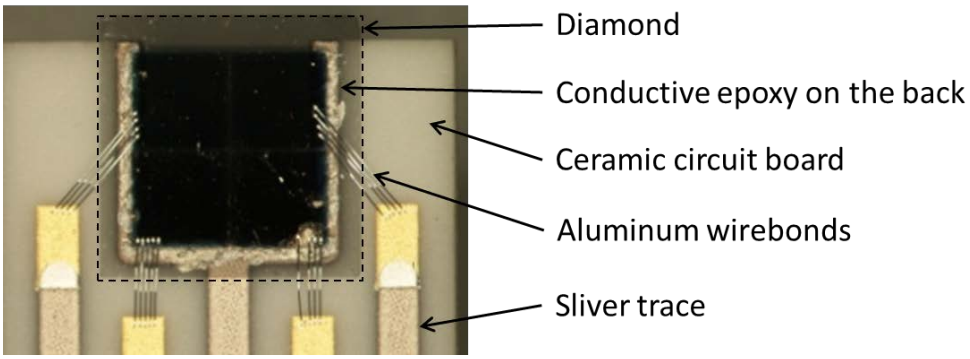

Figure 22 The metalized diamond mounted on a pre-designed circuit board using conductive epoxy. The quadrant pads in the front are connected to the circuit board using aluminum wire bonds.

5.3 Results and discussion

In Figure 23, results of the white beam x-ray topographs of the thinned diamonds present far less dislocations than the diamonds we tested in section 3, which is over 300 μm thick. Within the central active area in the images, samples are near featureless while along the edges traces of slip bands are still visible, with less contrast than thick diamonds. Aside from slip bands, there is very few indication of any carrier trapping sites in these images. X-ray topography proves that thinning the diamond effectively reduces structural defects in the crystal.

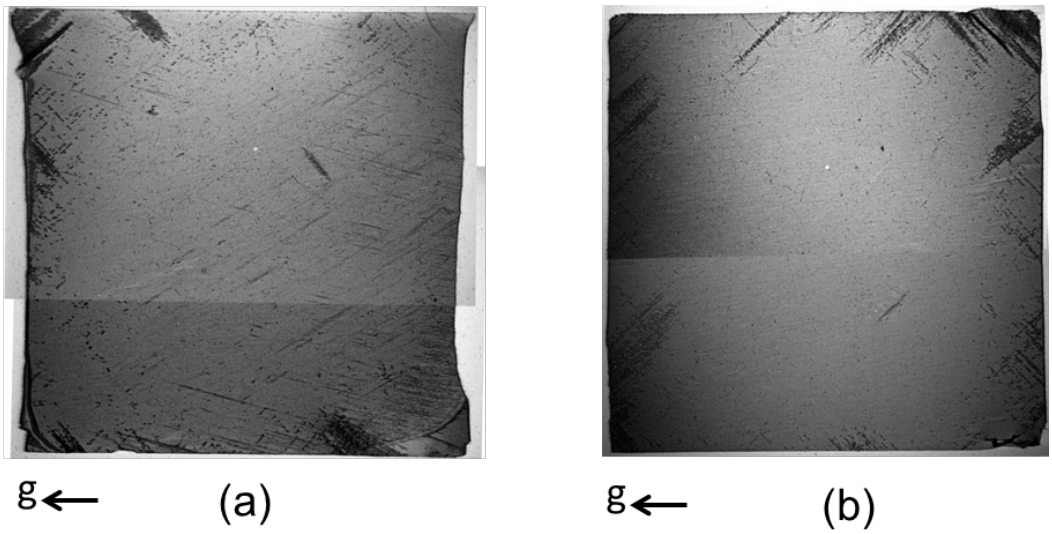

Figure 23 White beam x-ray topography of the 2 sliced diamond plates. The reflection selected is g=[-2-20] for both diamonds.

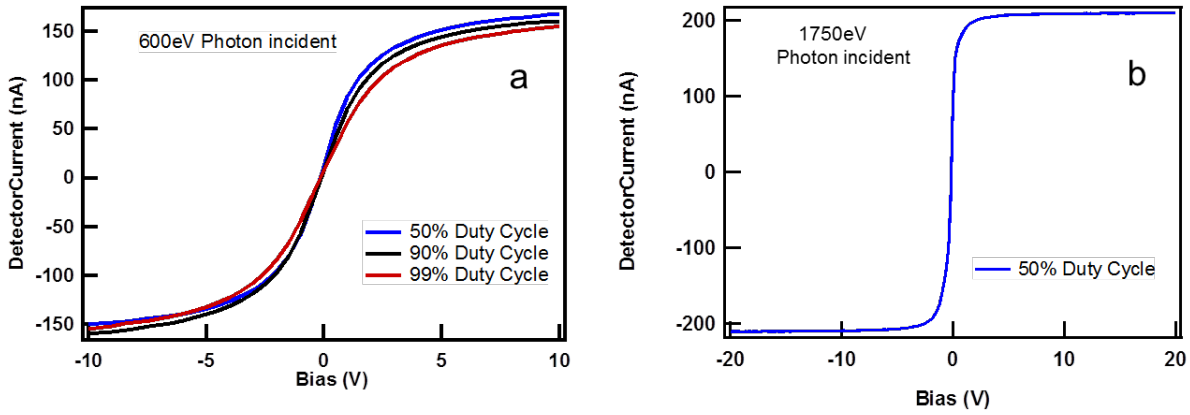

Figure 24 Bias scan of thin diamond with thickness of 25μm with Ag contact collected at incident photon energy at (a) 600eV with varied duty cycles and (b) 1750eV with 50% duty cycle.

Selected bias scans are compared in Figure 24 and Figure 25, measured at beamline U3C and X8A with varied conditions to achieve signal saturation. A collection of I-V curves collected with 600eV incident photon energy and normalized for duty cycles for one of the thin diamond are compared in Figure 24a. At 600eV, electron-hole pairs are excited near the surface of the diamond and one type of carriers need to travel across the bulk crystal, which is a routine method for us to investigate behavior difference for charge carriers. Therefore, the symmetric behavior for positive and the negative side of these curves indicates a similar collection efficacy for both

types of carriers. In addition, the comparison between different duty cycles at same photon energy indicates that the charge trapping effect in this diamond is much weaker than what we observe in thicker diamonds with higher dislocation density. (Figure 40 in Appendix III gives an example of asymmetric behavior of charge carriers in another diamond, with a more extreme charge trapping effect that the lower duty cycles reach saturation level mush faster than higher duty cycles.) Aside from symmetry, it can be noticed that at low incident photon energy, the slope of the I-V curves are much smaller than the curve taken at a higher photon energy, indicating that when electron hole pairs are generated closer to the diamond surface, a much stronger effect of carrier loss into the contact will occur.[33]

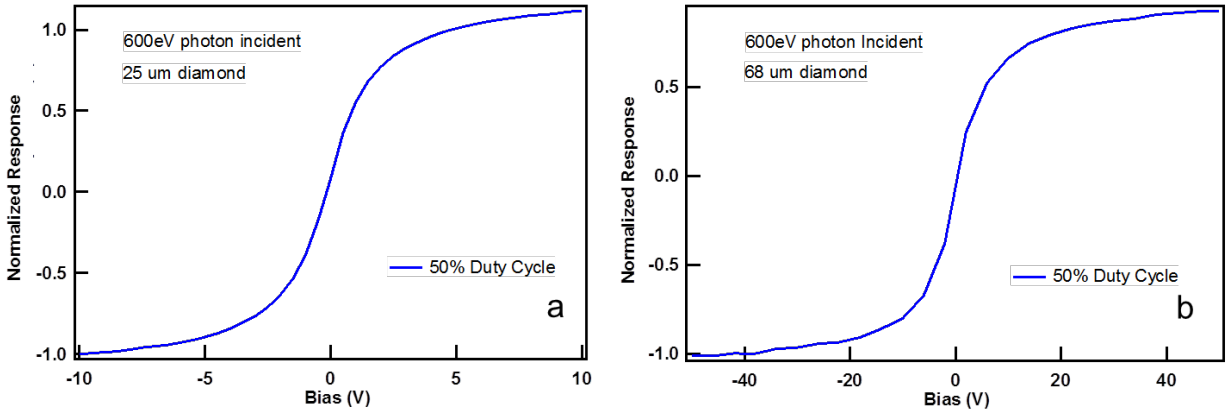

Figure 25 Bias scan of (a) thin diamond with thickness of 25μm and (b) diamond with thickness of 70μm, with incident photon energy at 600eV and biases are applied at 50% duty cycle.

Aside from reducing the dislocation/defect density, it is also intuitive that thinner diamond will generate a higher electric field in diamond than the thicker ones given the same working voltage. Figure 25 shows the comparison between the bias scans for a 25μm thick diamond and a 70μm thick diamond both collected at 600eV photon energy. Both diamonds are from the same vender with similar crystal quality. In Figure 25a, the thin diamond reaches its saturation level at around 10V, while in Figure 25b the sample reaches saturation at around 40V. While the 2 sample requires similar electric field to reach saturation, the device made out of the thin diamond can be operated at a much lower voltage at the same given photon energy.

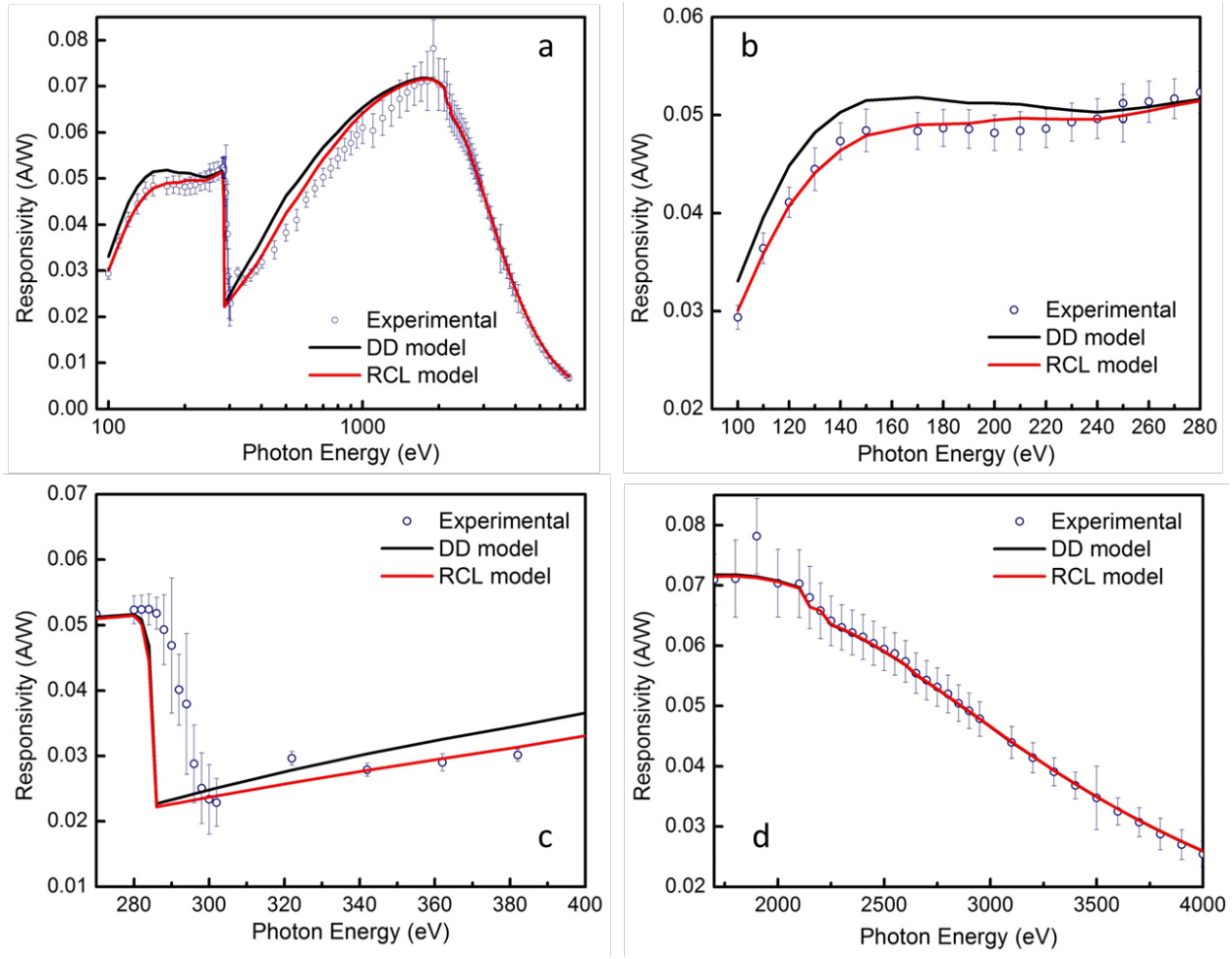

Figure 26 Photon energy vs diamond responsivity for thin diamond x-ray monitor covering a photon energy range from 0.1keV to 6.5 keV, with experimental data (circular symbol) compared with dead diamond (DD) model (dark line) and recombination length (RCL) model (red line) calculated using Equation 3 and Equation 4 respectively. a) Full range of diamond responsivity; b) subset of Pt filter feature; c) subset of carbon K edge feature; d) subset of Pt edge feature.

Results of diamond responsivity vs photon energy were corrected by background and duty cycles and the full data covering an energy range from 0.1 to 6.5keV is presented in Figure 26, along with the calculated results using dead diamond (DD) model from Equation 3 and the recombination length (RCL) model from Equation 4 we have introduced in Section 2.6 and 2.7.[33] By fitting the experimental diamond responsivity with the models mentioned above, we are able to accurately determine the thickness of the diamond sample and the incident Pt electrode. The DD model is calculated using the pair creation energy W= 13.3eV,[20, 35] a diamond thickness of 33μm, a 10nm thick Pt incident electrode and a dead diamond layer with the thickness of 50nm. In the calculation of the RCL model, the recombination length is fitted to be 80nm with all other parameters being the same as the DD model.

The experimental diamond responsivity presents 3 characteristic features: at 100eV ~250eV the shape of the curve is dominated by platinum attenuation length, the carbon edge feature with some trailing structures at 280eV~ 300eV and the platinum M edge at 2170eV. [32]These features are shown in figure 26b, 26c and 26d respectively. We can see that in the comparison of the platinum feature the RCL model gives a better fit to the experimental data than the DD model with the expected Pt thickness of 10nm. The recombination length is dependent with the electric field in the diamond and in this case is determined to be 80nm.[33] Figure 26c compares the carbon edge feature with the 2 models. The diamond carbon K edge is found to be ~290eV instead of 284eV from CXRO database, which is from sp^2 carbon K edge. Other than the edge shift, the RCL model again presents a better fit of the post carbon edge slope from 300eV to 400eV. As photon energy increases, the recombination effect no longer affect the charge collection and the 2 models merge at around 2keV (figure 26d), after which diamond thickness become the dominant factor that affects the responsivity. Fitting over this region gives a diamond thickness of 33 μm.

5.4 Conclusions

In summary, thin diamonds have less x-ray absorption and can be designed to adapt needs in soft x-ray applications. Reduced thickness will lead to reduced structural defects and therefore charge trapping effect in thin diamonds is much weaker than what we observe in thicker diamonds with higher dislocation density. Compared to a thicker diamond with similar crystal quality, the device made out of the thin diamond can be operated at a much lower voltage to achieve signal saturation at the same given photon energy.

Section 6 Carbon edge response of diamond devices

6.1 Introduction

In previous sections we have introduced possible solutions to the problems we encountered in the process of developing diamond x-ray detectors including avoiding generation of photoconductive gain and improve device performance based on previous investigations. We have congregated the efforts and developing in collaboration with Sydor Instruments. *LLC* commercialized diamond electronics. One of the prototypes of these detectors is fabricated and put into investigation of diamond carbon edge responses. The specifics of this detector are described in Appendix I.

We have described in Section 2.6 the competition between carriers drifting away from the incident electrode and carriers historically diffusing back, resulting in a net carrier loss. This carrier loss results in a field dependence of charge collection efficacy of a diamond device. The post carbon edge diamond response represents this bias dependence most prominently due to shallow x-ray absorption. In this section we measured diamond responses over the carbon K edge region at various biases, observations are made and results are discussed.

6.2 Experimental

Diamond response is collected using the diamond prototype detector (see Appendix I for sensor fabrication details) at beamline U3C at NSLS. The beamline has an energy range from 50 eV to 1000 eV with a 1.5 eV energy resolution, utilizing two gratings to cover the entire range, G1 (50 eV to 270 eV) and G2 (280 eV to 1000 eV). Near the carbon absorption edge, the flux is ~ 7×10^8 photon/sec in a spot size of 10mm wide × 1mm high. The detector is placed on a precision motor stage in a beamline vacuum chamber with a base pressure of 1×10^7 Torr.

The x-ray size, defined by a 800 μm circular aperture, is incident on the patterned side of the detector. A pulsed bias (square wave with 90% duty cycle) is placed on the back side of the detector and the current through the diamond is measured using a Keithley 6517A electrometer.[56] All four quadrant channels are tied together outside the vacuum chamber; the positioning capabilities are not under investigation in this section.

6.3 Results and discussion

The charge transport at the interested photon energy range corresponds to the low energy incident scenario described in Section 2.4 and illustrated in Figure 8a. Soft x-ray power is absorbed and the charge carriers are created at the incident surface of the diamond. Depending on the type of bias applied, either type of charge carriers travels through the full thickness of the bulk diamond and are collected by the contact.

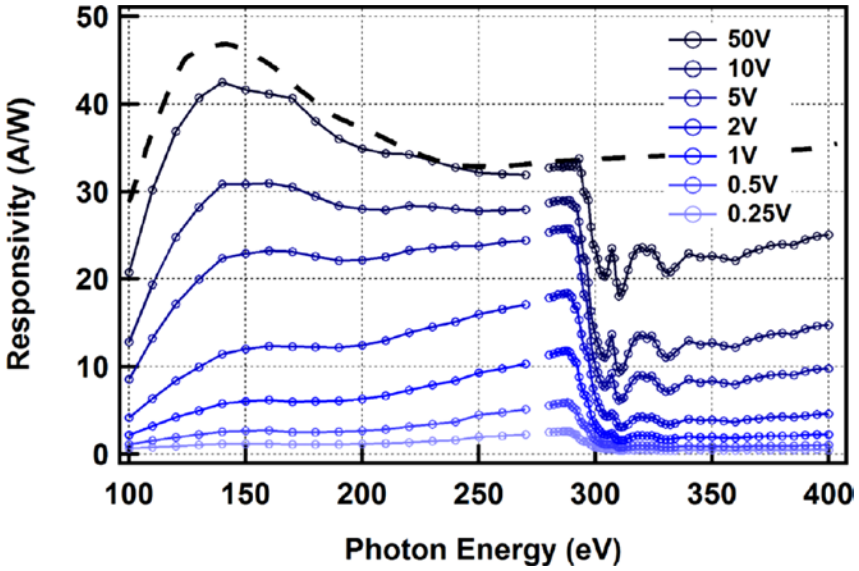

Figure 27 (a) Responsivity of the diamond x-ray detector vs. energy for a range of electric fields. The color scheme remains the same for Figure 28. The dotted line represents the charge collection in the absence of any diffusion loss.

The responsivity is measured from 100 eV to 400 eV for a range of applied bias and is shown in Figure 27. The rising feature from 100 eV to 200 eV which is characteristic of the platinum attenuation length[32] and the region from ~290 eV to 350 eV which is near the carbon K-edge with some trailing structure are presented. There is also an overall reduction in the magnitude of the signal as the bias is decreased below full charge collection. However, because sub full collection is the result of trapping in the bulk and the incident soft x-rays are absorbed very close to the incident electrode, this reduction should not depend on the photon energy. By normalizing the responsivity data to a response at a given energy (we have chosen 270 eV for G1 and 280 eV for G2), we can compare the fraction of the total x-ray generated charge carriers which escape the incident electrode (not lost to diffusion) versus applied bias.

Before analyzing the details of the detector response, a model of the diamond response will be presented which includes the bias dependent carrier loss due to diffusion, which is a simplified approach proposed by Keister et al.[39] It has been determined using Monte Carlo simulations that the collection efficiency of x-ray generated charge carriers follows an exponential dependence with the depth from the incident surface,[31] $CE = 1 - e^{-x/\beta}$, where x is the depth from the diamond surface and β is the characteristic recombination length of the carrier that is dependent of inner electric field in diamond.

Higher electric field will reduce β, i.e., with higher field, charge carriers are recovered closer to the incident electrode. Convolving this with the exponential dependence of the x-ray absorption in the diamond, the responsivity can be calculated by taking the fraction of collected carriers to the total amount of carriers generated by the x-rays as follows:

$$S = \frac{1}{W} \times \frac{\int_0^\infty I_0 e^{-\frac{x}{\lambda_D}} (1 - e^{-\frac{x}{\beta}}) dx}{\int_0^\infty I_0 e^{-\frac{x}{\lambda_D}} dx} \qquad \textbf{Equation 6}$$

where S is the responsivity, W is the mean ionization energy, I_0 is the initial x-ray intensity, and λ_D is the attenuation length in diamond. Evaluating these integrals and including a term for the transmission through the thin platinum electrodes and the total diamond thickness, the full responsivity is given as

$$S = \frac{1}{W} e^{-\frac{t_{Pt}}{\lambda_{Pt}}} (1 - e^{-\frac{t_D}{\lambda_D}}) (\frac{1}{1 + \beta/\lambda_D}) \qquad \textbf{Equation 7}$$

where t_{Pt}, t_D are the thickness of the incident electrode and the bulk diamond; and λ_{Pt} stand for the Pt attenuation length.[33] This expression is the same form as Equation 4 in section 2.7.

The first exponential term accounts for the loss in the platinum electrode using the corresponding attenuation length λ_{Pt}. The term $1 - e^{-\frac{t_D}{\lambda_D}}$ accounts for the absorption of the overall thickness of the diamond. Given the photon energy range we use in this measurement, this term will always equal to 1, which means all the x-ray is absorbed by the diamond. The term $\frac{1}{1 + \beta/\lambda_D}$ shows that the collection efficacy depends on the ratio of the recombination length and the attenuation length in diamond. If the recombination length $\beta = 0$, this term goes to 1 and no carbon edge feature would be observed in the response of this diamond detector.

Figure 28a presents the comparison between the platinum feature in the detector response with the calculated model. At high electric field where β is small compared to λ_D, the responsivity follows the expected curve and the platinum is only acting as a filter (shown as a dotted line in Figure 28a). As the field decreases (increasing β), the loss of carriers is dominated by diffusion loss into the electrode and the responsivity no longer takes the shape of a platinum filter. The lower limit is shown where β is large compared to λ_D, also shown as a dotted line in Figure 28a.

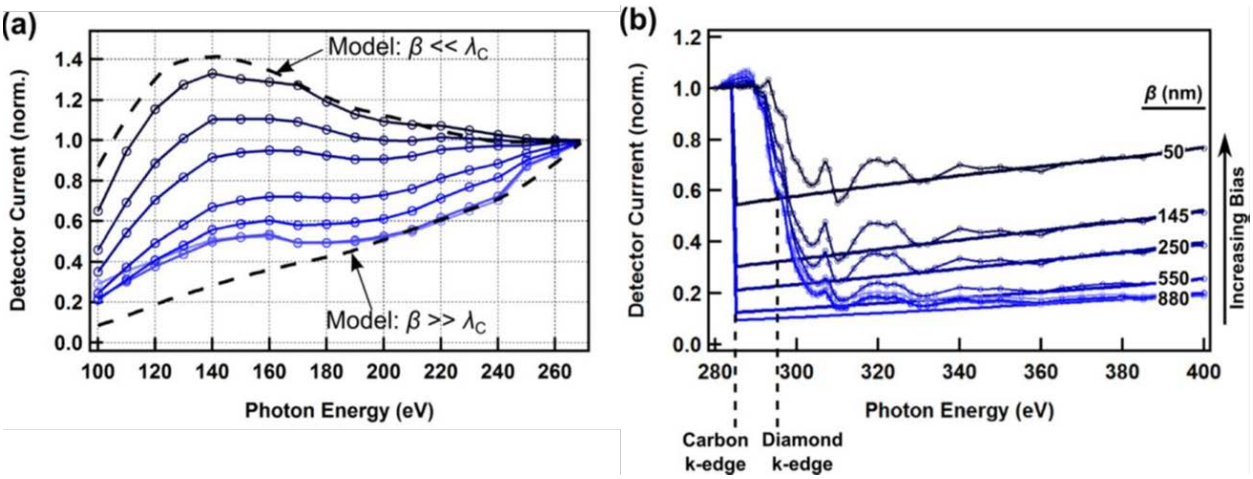

Figure 28 Voltage dependence of the detector response vs energy. (a) Responsivity showing the voltage evolution of the platinum feature. The solid lines show the model with the given value of b. (b) Responsivity across the carbon edge.

We also compared this model to the normalized carbon edge feature in Figure 28b. There are two prominent features: one notable feature is the discrepancy between the locations of the carbon K-edge in the model and our diamond response. This is because the model uses the attenuation length of sp^2 carbon provided by the Center for X-ray Optics database[32] with carbon K-edge at 284 eV. However, the data is presenting an edge at ~6 eV higher in photon energy which is reported as the diamond K-edge.[57, 58] Another feature is that as the bias is lowered, the step size at the carbon edge increases, indicating an increased loss of charge carriers. This strongly suggests that the carbon edge feature in the detector response is related to abrupt reduction (going from 1.5 μm to 55 nm crossing the edge) of the x-ray attenuation length increasing the loss of carriers due to diffusion, not from a dead carbon layer. In this shallow region, diamond response is more sensitive to the carrier loss due to the two competing mechanisms and a stronger inner field will pull more carrier away from the incident electrode before they are lost by diffusing back. The values of β are obtained by aligning the model with the diamond response between 360eV to 400eV due to a lack of post carbon edge fine structure in the model.

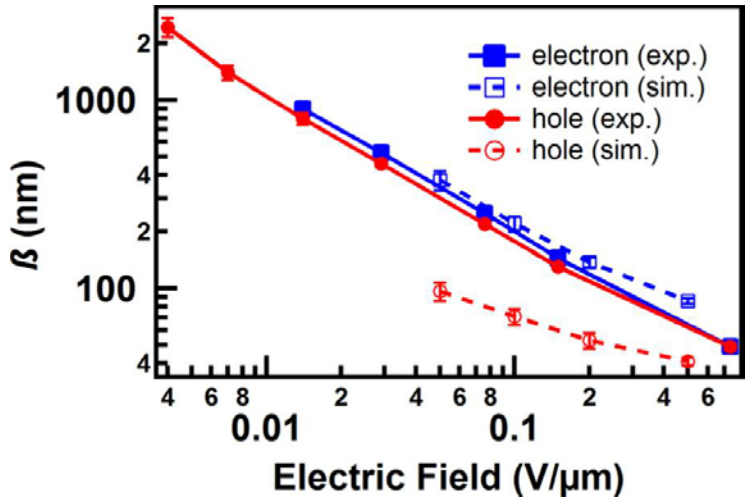

Figure 29 Comparison of the measured and simulated recombination lengths.

In Figure 29, The experimentally determined values of β are compared with the recombination length obtained by fitting the simulation results from Dimitrov et al.[34] From the comparison we can tell that the results from the simulations for electrons are in agreement with the experimental values (except for the larger deviation at the highest bias simulated), while the the values for β from the hole simulations are lower than the experimental ones. To obtain this level of agreement with the experimental data, we had to include the effects of both the transverse and longitudinal electron effective masses ($m_{l\Delta} = 1.4m_0$ and $m_{t\Delta} = 0.36m_0$ with m_0 the electron mass in vacuum[59]). A reduced treatment of electron transport using a scalar value for the electron effective mass (removing the effective mass anisotropy) changes the observed drift-diffusion properties by as much as 50%, thus decreasing the agreement with the experimental data. A possible reason for the deviation at higher bias values could be due to limitations of using a single electron band (and energies close to the bottom of the six equivalent valleys) to model the electron transport. At higher applied bias, the electron energies increase leading to hot electron transport requiring extensions of the model.

The deviation between experimental and simulation results for holes could rise from the use of heavy holes only in the simulations, and to a lesser degree to the assumption that each heavy hole energy ε satisfies $\varepsilon / \varepsilon_{so} \gg 1$, where ε_{so} = 6 meV is the split-off energy of the lowest valence band.[59] Thus, in our simulations, the holes have a mass $m_h = 1.08m_0$. We expect that including light holes in the simulations together with extensions to model both the energy regimes $\varepsilon / \varepsilon_{so} \gg 1$ and $\varepsilon / \varepsilon_{so} \ll 1$ will improve the agreement with the experimental data. Including light holes in the modeling will lead to creation of holes with masses as low as $m_l = 0.19m_0$ (see, e.g., Table V in Jacoboni and Reggiani) and significantly higher initial hole velocities. A larger number of holes will be lost at the incident electrodes due to diffusion of holes with higher initial velocities. Thus, collection efficiency of these holes will decrease resulting in increase of the overall value for β of holes and improved agreement with the

experimental data. We are considering to add modeling of light hole transport in the simulations to check how much this effect will improve the agreement with the experimental data.

6.4 Conclusion

In summary, the model of charge transport in diamond which includes an electric field dependent charge collection has been experimentally supported by the observation of three main features in the responsivity versus photon energy data. First, the rise of the platinum edge feature in range of photon energy is from 100 eV to 200 eV. Second, both the existence and the appearance of the carbon k-edge feature at a higher than expected photon energy typically associated with the diamond establish that this feature does not arise from a dead carbon layer. And finally, the bias dependence changes the magnitude of the carbon K-edge drop, demonstrating that higher fields are associated with higher charge collection consistent with the model. Carrier loss at the incident electrode has particularly strong implications for the diamond amplified photocathode where primary electrons are used to generate charge carriers in the diamond and are absorbed very close to the incident surface. A detailed understanding of this mechanism is needed to mitigate carrier loss in this case. This also opens up the possibility of a relatively simple and easy to use NEXAFS detector to study a variety of diamond-like carbon contacts such as in nitrogen doped UNCD where the charge generation and transport mechanisms are not fully understood.

Section 7 Non-metal contact I--Nitrogen doped ultrananocrystalline diamond (nUNCD)

7.1 Introduction

It is found that the traditional noble metal contact such as Platinum and Titanium will result in a signal loss due to the relatively high absorption of x-ray (High Z value.[56]) We have discussed in the previous sections about these non-carbide forming metal contacts and our effort to reduce the beam loss in engineering the thickness and the coverage of the electrode. We have also started our discussion in the possibilities of using boron doped diamond layer as diamond electrodes instead of traditional metal contact. In this section, we will continue this topic and discuss another option of non-metal contact-- nitrogen doped ultrananocrystalline diamond (nUNCD).

The UNCD thin films exhibit similar physical properties to single crystal diamond in the aspects of mechanical, thermal and resistance to radiation damage. Current UNCD thin films are grown by microware plasma chemical vapor deposition (MPCVD) or hot filament chemical vapor deposition (HFCVD) with mixed H2/Ch4 or Ar/CH4 plasma chemistries. Nitrogen is introduced to UNCD thin film to improve its electrical conductivity to semi-metallic level, and therefore can be considered as a replacement of metal to function as an electrode various applications like biomedical devices, biosensors, and in our case the x-ray detectors. [60]

In this section, a diamond device prepared with uUNCD on both sides as electrodes is studied and results are compared with the device fabricated with traditional platinum contact.

7.2 Experimental

In order to improve the performance of the monitor, nitrogen doped ultrananocrystalline diamond (nUNCD) is grown on single crystal CVD diamond as a contact at Argonne National Laboratory (ANL).

X-ray white beam topography and birefringence images were recorded for this sample respectively. X-ray topography was performed at Beamline X19C and birefringence images were taken using a polarized microscope. Sample was then tested in the similar measurements described in the previous sections. 2D responsivity maps and calibrated response vs photon energy of this diamond were collected at various beamlines cover a photon energy range of 0.2~28keV. Beamline U3C provides monochromatic beam of photon energy from 0.2 to 1keV, while beamline X8A provides x-ray from 1~6.5keV and beamline X15A from 6.5 ~2.8keV, with an intensity ranged from 10^{-9}~10^{-6} W/mm^2. [56] Measurements at U3C are performed in a vacuum level of 10^{-7}torr and at X8A in a vacuum of 10^{-6} torr due to the high absorption rate of air for low energy photons, and is in air at X15A. Incident x-ray power is calibrated using silicon photodiodes at both U3C and X8A (with thickness of 25 μm and 52 μm respectively), while air-filled ionization chamber is used at X15A. Various biases in the saturated range of either DC level or in the form of square wave with adjustable magnitude, frequency and duty cycle, were

applied on tested diamond plates to assure full collection of desired charge carriers (positive bias for hole collection and negative bias for electron collection).

7.3 Results and discussion

Figure 30 shows the compared results of the 2 imaging techniques. The nUNCD contact is completely transparent under the white beam at X19C (Figure 30a). The dark circled area in Figure 30b indicates the nUNCD contacts on both sides of the diamond. Prominent contrast of slip bands as described in section 3 was observed in both topography and birefringence images.

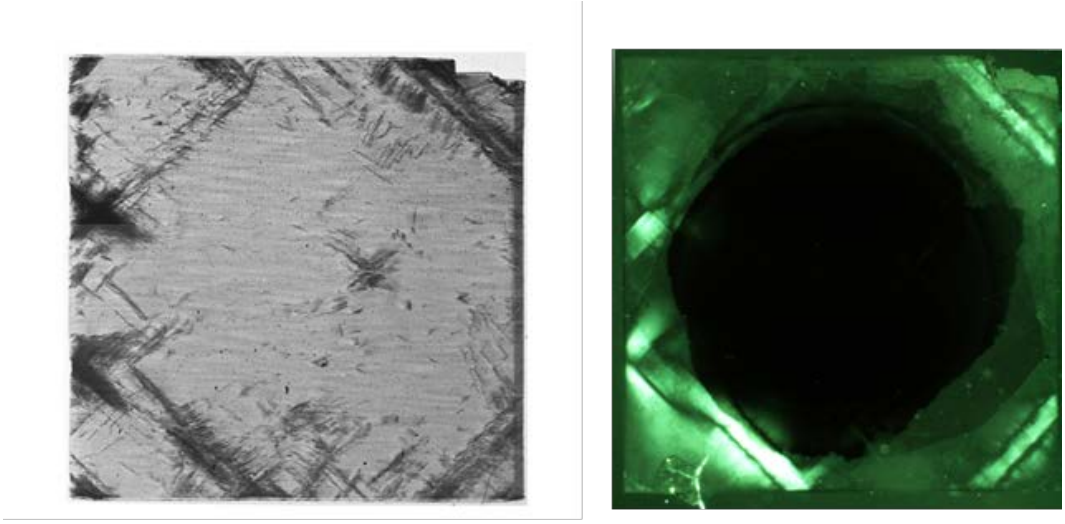

Figure 30 (a) X-ray topography and (b) birefringence images of the nUNCD coated diamond.

2D responsivity maps of this diamond are collected at various beamlines at different energies. The values of x-ray attenuation length of diamond (the depth into the diamond measured along the surface normal where the intensity of x-rays falls to 1/e of its value at the surface) at these energies are listed in Table 3.[32] According to x-ray database CXRO, a minimum energy of 1350eV is needed for a photon to travel all the way through a 300 μm thick diamond. Since it is difficult to control the growing process of the nUNCD layer, the thickness of this contact may vary in a range of 200nm to 500nm.

Table 3 X-ray attenuation length of diamond at various energies from CXRO X-Ray Database [32]

Beamline	U3C		X8A		X6B	X15C	
Photon Energy (eV)	350	1000	2000	4000	19000	19000	White Beam
X-ray attenuation length (microns)	0.0878	1.2888	9.4507	75.6276	7129.76	7129.76	N/A

Responsivity maps collected at the listed energies and representative results of these measurements are presented in Figure 31. Both positive and negative biases were applied with duty cycles for electron detrapping.

From Table 3, we can tell that at low energies, most of the incident beam is absorbed by the nUNCD layer. This is verified in Figure 31a and 31b. A halo ring is observed in the response maps at low energies, indicating a thicker area in the center of the contact where a larger absorption of the incident beam occur, resulting in a weaker signal than the edge area. Figure 31(c) and (d) are showing a relatively flat response over the contact, though photoconductive gain was observed at the edge of the contact. Similar features are observed in responsivity maps collected at other energies for this diamond.

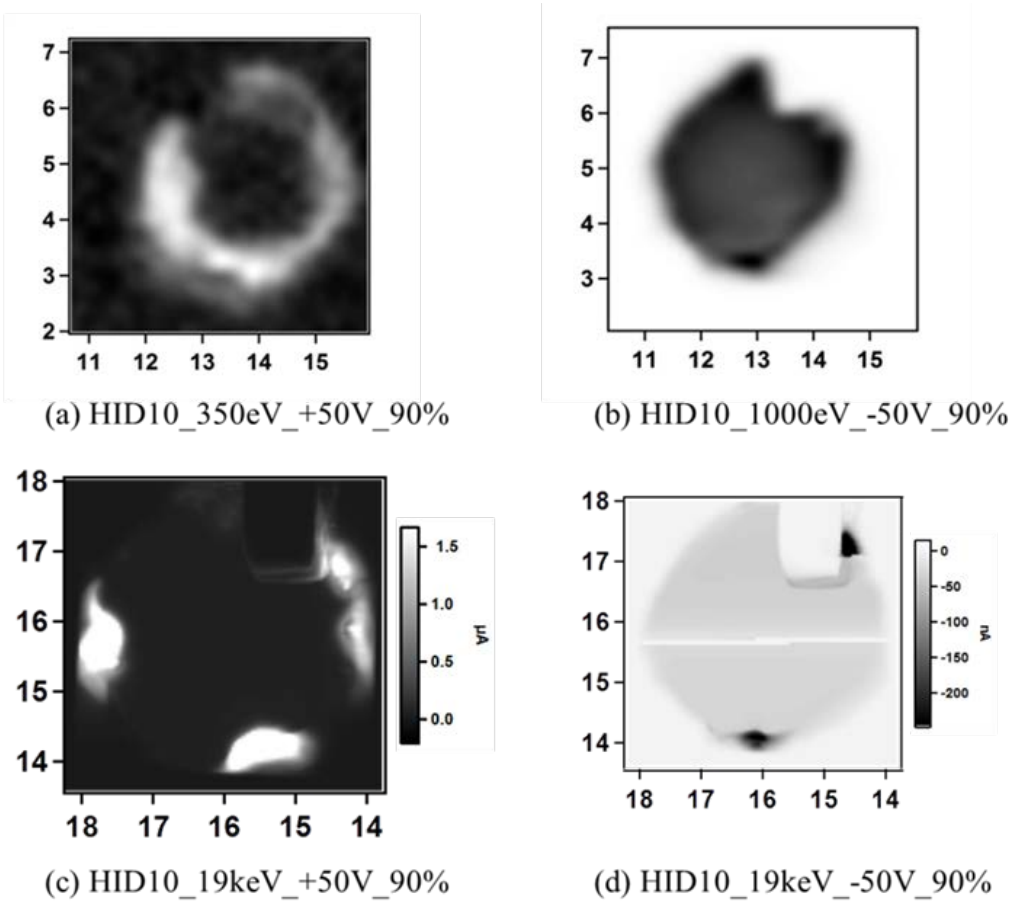

Figure 31 2D responsivity maps for diamond with nUNCD grown as a contact. Measurements were taken at (a) 350eV and (b) 19keV.

In section 2 we have introduced a proposed model to describe diamond device response. Equation 3 is established under the circumstances of metal contacts on both sides of the diamond. For this particular uUNCD contact diamond, Equation 1 can be modified as

$$S = \frac{1}{W} e^{-\frac{t_{UNCD}}{\lambda_D}} (1 - e^{\frac{t_{dia}}{\lambda_D}}) \qquad \textbf{Equation 8}$$

where t_{nUNCD} and t_{dia} are the thickness of the nUNCD layer and the diamond plate. The effect of the dead carbon layer can be included in the thickness of the nUNCD layer.

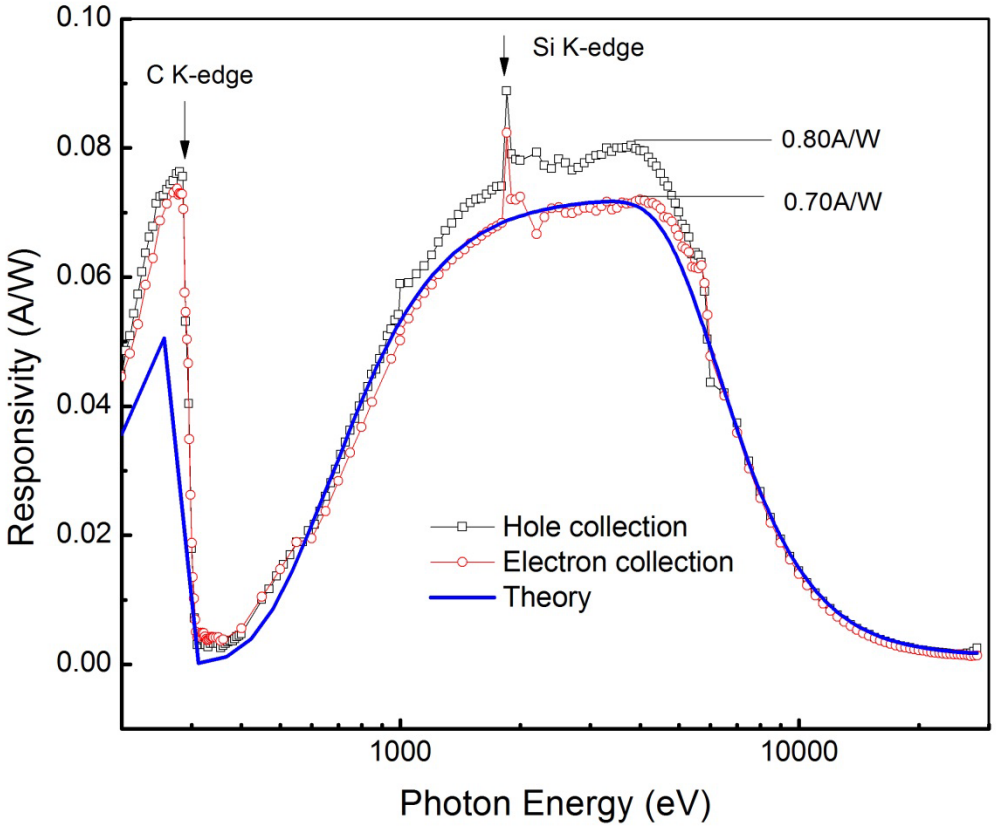

Figure 32 Responsivity of a 0.3mm thick diamond HID10 coated with nUNCD diamond on both sides as contacts. Symbols are measured resposivity of electrons and holes as carriers. Calculated plot (lines) using Equation 6 and a responsivity curve of another diamond with Pt contacts measured under the same conditions are present as reference.

Current mode responsivity data for Platinum coated (~30nm) diamond and nUNCD coated CVD diamond tested under monochromatic x-rays are presented in Figure 32. It is reported for Platinum coated diamond, a bias of 100V is found to be sufficient to extract over 95% of the available photocurrent. For nUNCD diamond, this voltage is found to be 50V for both carriers (See figure 33). The calculated theoretical responsivity using Equation 6 is plotted as a reference using mean ionization energy W=13.8eV, which is a value with 4% difference from the reported value 13.3eV. In other words, the measured curve fits the theoretical model within a range of 4%, which is also observed in the previous study.[8] The fitting thickness of the filter is using 400nm, including a combined effect of the nUNCD layer and the dead carbon layer

inside the diamond. The latter was theoretically predicted and also observed for Pt contact diamond. [61]

A slight photoconductive effect is observed in the responsivity maps, energy scans and the bias scans for this diamond, when positive bias is applied and holes are collected. In Figure 32, the electrons and holes give similar responsivity at low energy range, and holes gives slightly higher responsivity in higher energy range, with the peak responsivity value close to 0.08 A/W, which exceeds the predicted highest diamond responsivity for other detectors we've tested, which is around 0.07 A/W. In the bias scan shown in Figure 33, the positive side of the plot also gives an observable sign of photoconductive gain.[8, 41] This observation indicates that at the nUNCD-diamond junction, the potential barrier might not be high enough to block holes from injection.

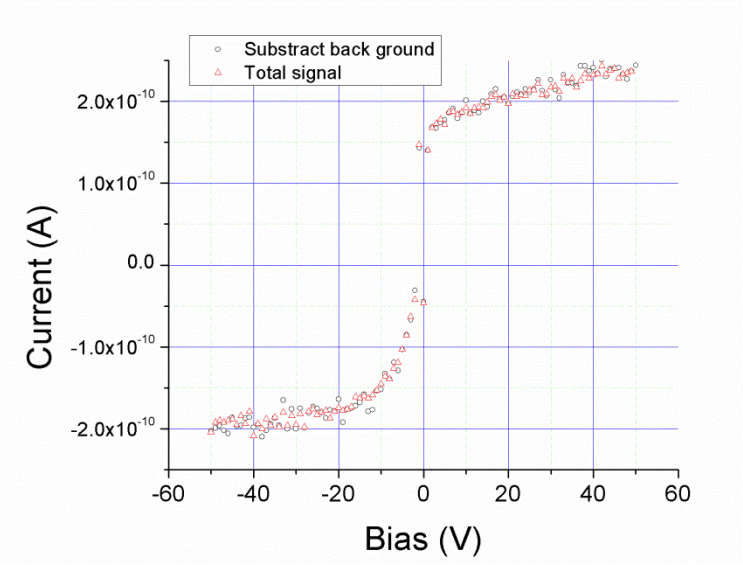

Figure 33 Bias scan for HID 10 at Beanline X8 at 2keV. It is noticed that the collection of holes is slightly photoconductive.

The responsivity of diamond with nUNCD contact is compared with a calibrated diamond detector that is 68µm thick and has 20nm Pt contacts on both sides, in an energy range of 0.2 to 6keV where both data sets overlap. (Figure 34) We have discussed in detail the effects of Pt layer has on diamond device responsivity. In Figure 34b, where the 2 plots are magnified at the carbon edge, the nUNCD diamond has a higher response while the Pt filter gives a lower response in the Pt diamond detector. However, the nUNCD sees a much more dramatic effect in the post carbon area, where the attenuation length for diamond drops to its lowest value and carriers are lost either due to beam power absorbed in the nUNCD itself or the carrier diffusion that happens very close to the diamond-nUNCD interface (corresponding to a small recombination length).[33]

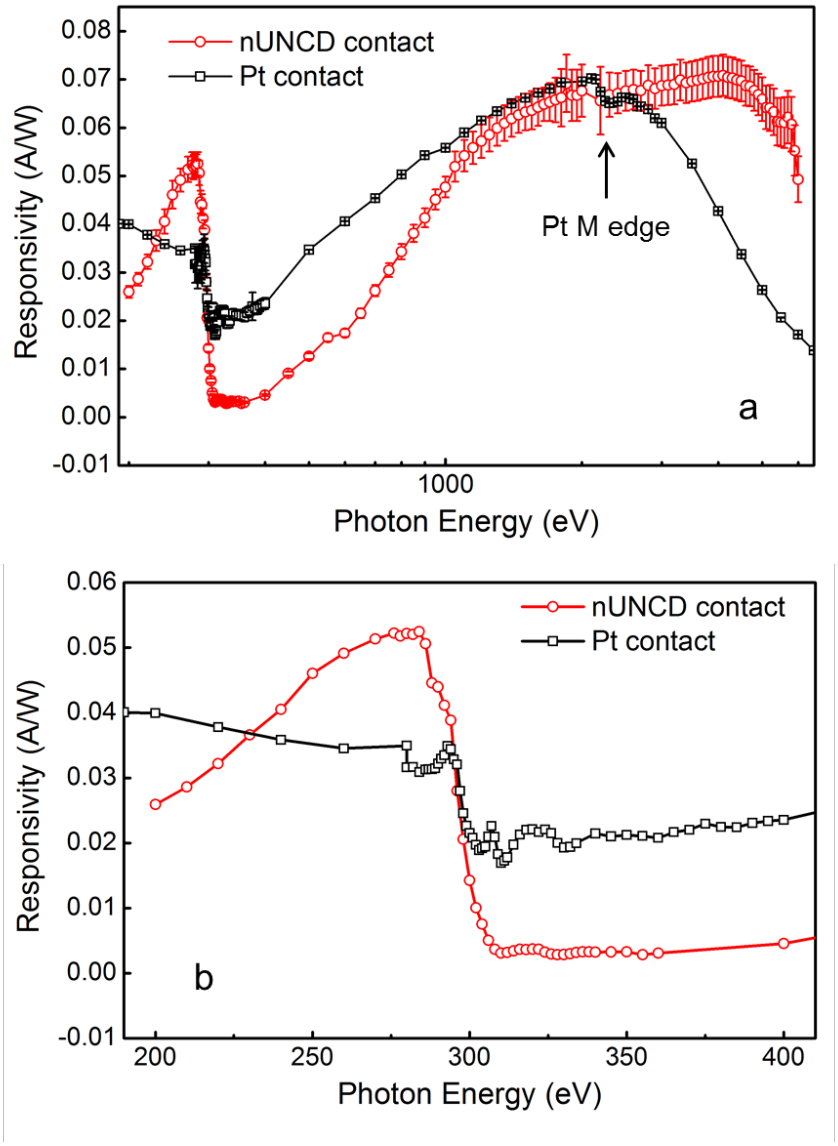

Figure 34 (a) Diamond responsivity of nUNCD as a contact compared with that of Pt as diamond contact from an energy range of 0.2~6 keV. (b) Comparison between the 2 samples at carbon edge.

7.4 Conclusion

The nitrogen doped UNCD contact diamond has a flat response and does not suffer from annealing. Photoconductive gain observed on the edge indicating an improvement is needed for the surface treatment and growth process. The nUNCD as a contact for diamond based beamline monitor is found to be more sufficient than the traditional noble metal contact such as Pt and Ti at low energy ranges due to less x-ray absorption and potentially can be designed as a diamond device for soft x-ray applications. The charge generation and transport mechanisms are not fully understood in the nUNCD contact and therefore further investigation is needed to adapt this low absorption contact for diamond detectors.

Section 8 Future Work

Extended work is needed to further improve our knowledge on both material science and engineering side of diamond detector research.

Results are presented in this paper in the characterization of the potentially electronically meaningful defects in diamond. We can see from the report that not all the photoconductive response that is not desired is coming from the structural defects inside the diamond but from the treatment of the surface of the photodiode. We are developing a new method of contact coating and trying to eliminate this factor from the study. If we can rule out the interference of surface treatment and isolate the electronically active center in the diamond, the correlation between structural defects and ununiformed responsivity will become clearer.

For the energy calibration of the diamond based x-ray monitors, aside from the traditional noble metal contact, new types of contact will be designed to avoid the signal loss from diamond to the metal contact. The investigation on non metal contact needs to continue on many aspects including improvement on device fabrication as well as further measurements to study its material science.

Proposed work also involves design and testing new electrode patterns for more sophisticated diamond based electronics, including pixelated and time resolved diamond radiation detectors for the 3^{rd} and 4^{th} generation synchrotron facilities. Better design and engineering to improve diamond devices with nUNCD contact also needs to be investigated to utilize the potential merits that nUNCD contacts have to build a more robust, radiation resist diamond device.

References

1. R. J. Keddy and T. L. Nam, Radiat Phys Chem **41** (4-5), 767-773 (1993).
2. H. Kagan, Nucl Instrum Meth A **546** (1-2), 222-227 (2005).
3. I. Ben-Zvi and e. al, in *Proceedings of Workshop on the Physics and Applications of High Brightness Electron Beams, Erice, Sicily* (2005).
4. D. R. Kania, L. S. Pan, P. Bell, O. L. Landen, H. Kornblum, P. Pianetta and M. D. Perry, J Appl Phys **68** (1), 124-130 (1990).
5. H. Kagan, Nucl Instrum Meth A **541** (1-2), 221-227 (2005).
6. H. Pernegger, S. Roe, P. Weilhammer, V. Eremin, H. Frais-Kolbl, E. Griesmayer, H. Kagan, S. Schnetzer, R. Stone, W. Trischuk, D. Twitchen and A. Whitehead, J Appl Phys **97** (7) (2005).
7. P. Bergonzo, D. Tromson and C. Mer, J Synchrotron Radiat **13**, 151-158 (2006).
8. J. Bohon, E. Muller and J. Smedley, J Synchrotron Radiat **17**, 711-718 (2010).
9. J. Morse, B. Solar and H. Graafsma, J Synchrotron Radiat **17**, 456-464 (2010).
10. E. Berdermann, M. Pomorski, W. de Boer, M. Ciobanu, S. Dunst, C. Grah, M. Kis, W. Koenig, W. Lange, W. Lohmann, R. Lovrincic, P. Moritz, J. Morse, S. Mueller, A. Pucci, M. Schreck, S. Rahman and M. Trager, Diam Relat Mater **19** (5-6), 358-367 (2010).
11. P. Bergonzo, D. Tromson, C. Mer, B. Guizard, F. Foulon and A. Brambilla, Physica Status Solidi a-Applied Research **185** (1), 167-181 (2001).
12. H. Pernegger, Phys Status Solidi A **203** (13), 3299-3314 (2006).
13. M. Franklin, A. Fry, K. K. Gan, S. Han, H. Kagan, S. Kanda, D. Kania, R. Kass, S. K. Kim, R. Malchow, F. Morrow, S. Olsen, W. F. Palmer, L. S. Pan, F. Sannes, S. Schnetzer, R. Stone, Y. Sugimoto, G. B. Thomson, C. White and S. Zhao, Nucl Instrum Meth A **315** (1-3), 39-42 (1992).
14. V. D. Kovalchuk, V. I. Trotsik and V. D. Kovalchuk, Nucl Instrum Meth A **351** (2-3), 590-591 (1994).
15. C. White, Nucl Instrum Meth A **351** (1), 217-221 (1994).
16. A. BenMoussa, J. F. Hochedez, U. Schuehle, W. Schmutz, K. Haenen, Y. Stockman, A. Soltani, F. Scholze, U. Kroth, V. Mortet, A. Theissen, C. Laubis, M. Richter, S. Koller, J. M. Defise and S. Koizumi, Diam Relat Mater **15** (4-8), 802-806 (2006).
17. A. BenMoussa, A. Theissen, F. Scholze, J. F. Hochedez, U. Schule, W. Schmutz, K. Haenen, Y. Stockman, A. Soltani, D. McMullin, R. E. Vest, U. Kroth, C. Laubis, M. Richter, V. Mortet, S. Gissot, V. Delouille, M. Dominique, S. Koller, J. P. Halain, Z. Remes, R. Petersen, M. D'Olieslaeger and J. M. Defise, Nucl Instrum Meth A **568** (1), 398-405 (2006).
18. S. Vatnitsky and H. Jarvinen, Phys Med Biol **38** (1), 173-184 (1993).
19. S. M. Vatnitsky, V. S. Khrunov, V. I. Fominych and E. Schuelell, Radiat Prot Dosim **47** (1-4), 515-518 (1993).
20. J. W. Keister, J. Smedley, E. M. Muller, J. Bohon and A. Heroux, Nucl Instrum Meth A **649** (1), 91-93 (2011).
21. E. M. Muller, J. Smedley, J. Bohon, X. Yang, M. Gaowei, J. Skinner, G. De Geronimo, M. Sullivan, M. Allaire, J. W. Keister, L. Berman and A. Heroux, J Synchrotron Radiat **19**, 381-387 (2012).
22. B. Ravel, K. Attenkofer, J. Bohon, E. Muller and J. Smedley, Rev Sci Instrum **84** (10) (2013).

23. S. Schubert, M. Ruiz-Oses, I. Ben-Zvi, T. Kamps, X. Liang, E. Muller, K. Muller, H. Padmore, T. Rao, X. Tong, T. Vecchione and J. Smedley, Apl Mater **1** (3) (2013).
24. A. E. Mora, J. W. Steeds, J. E. Butler, C. S. Yan, H. K. Mao, R. J. Hemley and D. Fisher, physica status solidi (a) **202** (15), 2943-2949 (2005).
25. M. P. Gaukroger, P. M. Martineau, M. J. Crowder, I. Friel, S. D. Williams and D. J. Twitchen, Diam Relat Mater **17** (3), 262-269 (2008).
26. H. Klapper, Mater Chem Phys **66** (2-3), 101-109 (2000).
27. A. R. Lang, R. Vincent, N. C. Burton and A. P. W. Makepeace, J Appl Crystallogr **28**, 690-699 (1995).
28. P. M. Martineau, M. P. Gaukroger, K. B. Guy, S. C. Lawson, D. J. Twitchen, I. Friel, J. O. Hansen, G. C. Summerton, T. P. G. Addison and R. Burns, J Phys-Condens Mat **21** (36), - (2009).
29. D. Araujo, M. P. Alegre, A. J. Garcia, J. Navas, M. P. Villar, E. Bustarret, P. N. Volpe and F. Omnes, Diam Relat Mater **20** (3), 428-432 (2011).
30. E. M. Muller, J. Smedley, B. Raghothamachar, M. Gaowei, J. W. Keister, I. Ben-Zvi, M. Dudley and Q. Wu, in *Diamond Electronics and Bioelectronics — Fundamentals to Applications III, edited by P. Bergonzo, J.E. Butler, R.B. Jackman, K.P. Loh, M. Nesladek (Mater. Res. Soc. Symp. Proc)* (Warrendale, PA, 2010), Vol. 1203.
31. D. A. Dimitrov, R. Busby, J. R. Cary, I. Ben-Zvi, T. Rao, J. Smedley, X. Chang, J. W. Keister, Q. Wu and E. Muller, J Appl Phys **108** (7), 073712 (2010).
32. B. L. Henke, E. M. Gullikson and J. C. Davis, Atom Data Nucl Data **54** (2), 181-342 (1993).
33. E. M. Muller, M. Gaowei, I. Ben-Zvi, D. A. Dimitrov and J. Smedley, Appl Phys Lett **104** (9), (2014).
34. D. A. Dimitrov, R. Busby, J. R. Cary, I. Ben-Zvi, T. Rao, J. Smedley, X. Chang, J. W. Keister, Q. Wu and E. Muller, J Appl Phys **108** (7) (2010).
35. J. Smedley, J. W. Keister, E. M. Muller, J. Jordan-Sweet, J. Bohon, J. Distel and B. Dong, MRS Online Proceedings Library **1203**(2009).
36. P. S. Lysaght, J. Barnett, G. I. Bersuker, J. C. Woicik, D. A. Fischer, B. Foran, H. H. Tseng and R. Jammy, J Appl Phys **101** (2) (2007).
37. A. K. Rumaiz, J. C. Woicik, G. A. Carini, D. P. Siddons, E. Cockayne, E. Huey, P. S. Lysaght, D. A. Fischer and V. Genova, Appl Phys Lett **97** (24) (2010).
38. E. A. Kraut, R. W. Grant, J. R. Waldrop and S. P. Kowalczyk, Phys Rev Lett **44** (24), 1620-1623 (1980).
39. J. W. Keister, J. Smedley, E. M. Muller and J. Bohon, Aip Conf Proc **1234**, 93-96 (2010).
40. H. Y. Fan, Physical Review **92** (6), 1424-1428 (1953).
41. E. M. Muller, J. Smedley, B. Raghothamachar, M. Gaowei, J. W. Keister, I. Ben-Zvi, M. Dudley and Q. Wu, MRS Online Proceedings Library **1203** (2009).
42. C. Szeles, S. E. Cameron, J. O. Ndap and W. C. Chalmers, Ieee T Nucl Sci **49** (5), 2535-2540 (2002).
43. J. Wu, R. Cao, X. Yang, P. Pianetta and I. Lindau, J Vac Sci Technol A **11** (4), 1048-1051 (1993).
44. J. van der Weide and R. J. Nemanich, Phys Rev B **49** (19), 13629-13637 (1994).
45. K. S. Kim, N. Winograd and R. E. Davis, J Am Chem Soc **93** (23), 6296 (1971).
46. G. N. Derry and P. N. Ross, Surf Sci **140** (1), 165-180 (1984).

47. Y. Mizokawa, T. Miyasato, S. Nakamura, K. M. Geib and C. W. Wilmsen, Surf Sci **182** (3), 431-438 (1987).
48. J. Diaz, G. Paolicelli, S. Ferrer and F. Comin, Phys Rev B **54** (11), 8064-8069 (1996).
49. C. T. Chen and F. Sette, Phys Scripta **T31**, 119-126 (1990).
50. P. A. Bruhwiler, A. J. Maxwell, C. Puglia, A. Nilsson, S. Anderson and N. Martensson, Phys Rev Lett **74** (4), 614-617 (1995).
51. D. A. Shirley, Phys Rev B **5** (12), 4709 (1972).
52. M. Peuckert and H. P. Bonzel, Surf Sci **145** (1), 239-259 (1984).
53. J. C. Woicik, E. J. Nelson, L. Kronik, M. Jain, J. R. Chelikowsky, D. Heskett, L. E. Berman and G. S. Herman, Phys Rev Lett **89** (7) (2002).
54. M. B. Trzhaskovskaya, V. I. Nefedov and V. G. Yarzhemsky, Atom Data Nucl Data **77** (1), 97-159 (2001).
55. J. W. Davenport, R. E. Watson, M. L. Perlman and T. K. Sham, Solid State Commun **40** (11), 999-1002 (1981).
56. J. W. Keister and J. Smedley, Nucl Instrum Meth A **606** (3), 774-779 (2009).
57. A. Laikhtman, I. Gouzman and A. Hoffman, Diam Relat Mater **9** (3-6), 1026-1031 (2000).
58. Q. Yang, S. Yang, Y. S. Li, X. Lu and A. Hirose, Diam Relat Mater **16** (4-7), 730-734 (2007).
59. C. Jacoboni and L. Reggiani, Rev Mod Phys **55** (3), 645-705 (1983).
60. O. Auciello and A. V. Sumant, Diam Relat Mater **19** (7-9), 699-718 (2010).
61. J. W. Keister, J. Smedley, D. Dimitrov and R. Busby, Ieee T Nucl Sci **57** (4), 2400-2404 (2010).
62. D. R. Kania, M. I. Landstrass, M. A. Plano, L. S. Pan and S. Han, Diam Relat Mater **2** (5-7), 1012-1019 (1993).
63. A. T. Collins and A. W. Williams, J Phys Part C Solid **4** (13), 1789 (1971).
64. W. Tsai, M. Delfino, D. Hodul, M. Riaziat, L. Y. Ching, G. Reynolds and C. B. Cooper, Ieee Electr Device L **12** (4), 157-159 (1991).
65. E. Bustarret, E. Gheeraert and K. Watanabe, Physica Status Solidi a-Applied Research **199** (1), 9-18 (2003).
66. G. Chicot, T. N. T. Thi, A. Fiori, F. Jomard, E. Gheeraert, E. Bustarret and J. Pernot, Appl Phys Lett **101** (16) (2012).
67. L. Diederich, O. M. Kuttel, P. Ruffieux, T. Pillo, P. Aebi and L. Schlapbach, Surf Sci **417** (1), 41-52 (1998).
68. C. H. Goeting, F. Marken, A. Gutierrez-Sosa, R. G. Compton and J. S. Foord, Diam Relat Mater **9** (3-6), 390-396 (2000).
69. S. Ghodbane, D. Ballutaud, F. Omnes and C. Agnes, Diam Relat Mater **19** (5-6), 630-636 (2010).
70. S. Ghodbane, D. Ballutaud, A. Deneuville and C. Baron, Phys Status Solidi A **203** (12), 3147-3151 (2006).
71. S. Ferro, M. Dal Colle and A. De Battisti, Carbon **43** (6), 1191-1203 (2005).
72. R. Graupner, F. Maier, J. Ristein, L. Ley and C. Jung, Phys Rev B **57** (19), 12397-12409 (1998).
73. C. Saby and P. Muret, Diam Relat Mater **11** (3-6), 851-855 (2002).
74. D. Ballutaud, N. Simon, H. Girard, E. Rzepka and B. Bouchet-Fabre, Diam Relat Mater **15** (4-8), 716-719 (2006).

75. M. Gaowei, E. M. Muller, A. K. Rumaiz, C. Weiland, E. Cockayne, J. Jordan-Sweet, J. Smedley and J. C. Woicik, Appl Phys Lett **100** (20) (2012).
76. J. R. Zeidler, C. A. Hewett and R. G. Wilson, Phys Rev B **47** (4), 2065-2071 (1993).
77. F. Fontaine, C. UzanSaguy, B. Philosoph and R. Kalish, Appl Phys Lett **68** (16), 2264-2266 (1996).
78. B. Ittermann, K. Bharuth-Ram, H. Metzner, M. Fullgrabe, M. Heemeier, F. Kroll, F. Mai, K. Marbach, P. Meier, D. Peters, H. Thiess, H. Ackermann, H. J. Stockmann and J. P. F. Sellschop, Appl Phys Lett **71** (25), 3658-3660 (1997).
79. H. X. Zhang, Y. B. Jiang, Q. B. Meng, Y. J. Fei, P. R. Zhu, Z. D. Lin and K. A. Feng, Appl Surf Sci **150** (1-4), 43-46 (1999).

Appendix I Fabrication and calibration of a prototype BPM

This detector started with an Element Six Electronic Grade single crystal diamond with a (100) surface orientation and (110) side plane supplied by Stony Brook University/BNL. It was cut and polished by DDK to be a nominal thickness of 70μm with lateral dimensions of 4.0 mm ×4.0 mm. This was later measured at beamline X8A to be 68 μm, data to be shown later. Sample was chemically cleaned and oxygen terminated on both sides by resting under an ozone lamp for over 4 hrs for each side. The patterns were prepared by optical lithography following similar steps described in section 2.2, with ~20nm Pt sputtered onto both sides. The front pattern is a 3.1mm x 3.1 mm square quadrant with 20micron streets in the center area while the outer streets are 80 microns wide (see Figure 35a). The diamond sensor was mounted onto a predesigned 5 channel circuit board, with Al wires bonding the quad pads to the board (see Figure 36). The board was assembled into a vacuum compatible case with SMA connectors. The size of the final detector is around 2 inch by 2 inch. The back side pattern is a solid square pad with the same lateral dimensions as the front electrode.

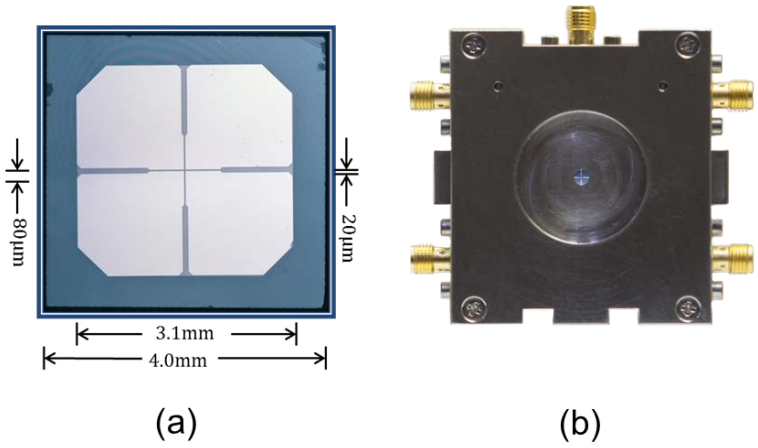

Figure 35 (a) Sensor front pattern: 3.1mm x 3.1 mm square quadrant with 20micron streets in the center area while the outer streets are 80 microns wide. (b) Stainless steel case with SMA connctors.

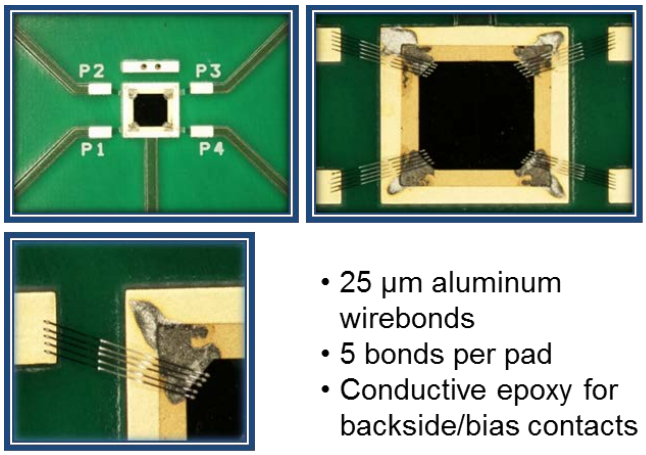

Figure 36 The predesigned 5 channel circuit board, with Al wires bonding the quad pads to the board.

Sample was then tested at beamline U3C and X8A, NSLS, BNL, where this diamond was installed on a X-Y precision motor with the wirebond side being incident to the beam. Bias was applied to the beam incident side and signal is collected on the beam exit side to avoid photoemission. Pulsed bias was applied for the measurements below 3 keV to ensure full collection.

A map of photocurrent taken at beamlime X8A were shown in Figure 37a, with a incident photon energy of 4keV at -5V DC bias. With applied bias this diamond gives a uniform response over the entire active area. As we purposely lowering the bias to 0.3V, the structure of the front pattern is observed. (Figure 37b).

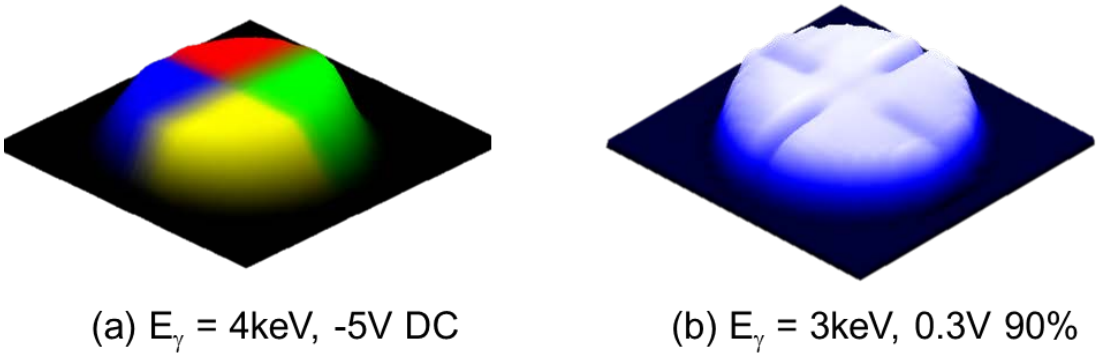

Figure 37 a) Current map of IIa diamond at 80V, DC. The shape and position of the diamond (solid line) and the contact (dotted line) are indicated in the figure. b) Bias scan from X15A, at 19keV.

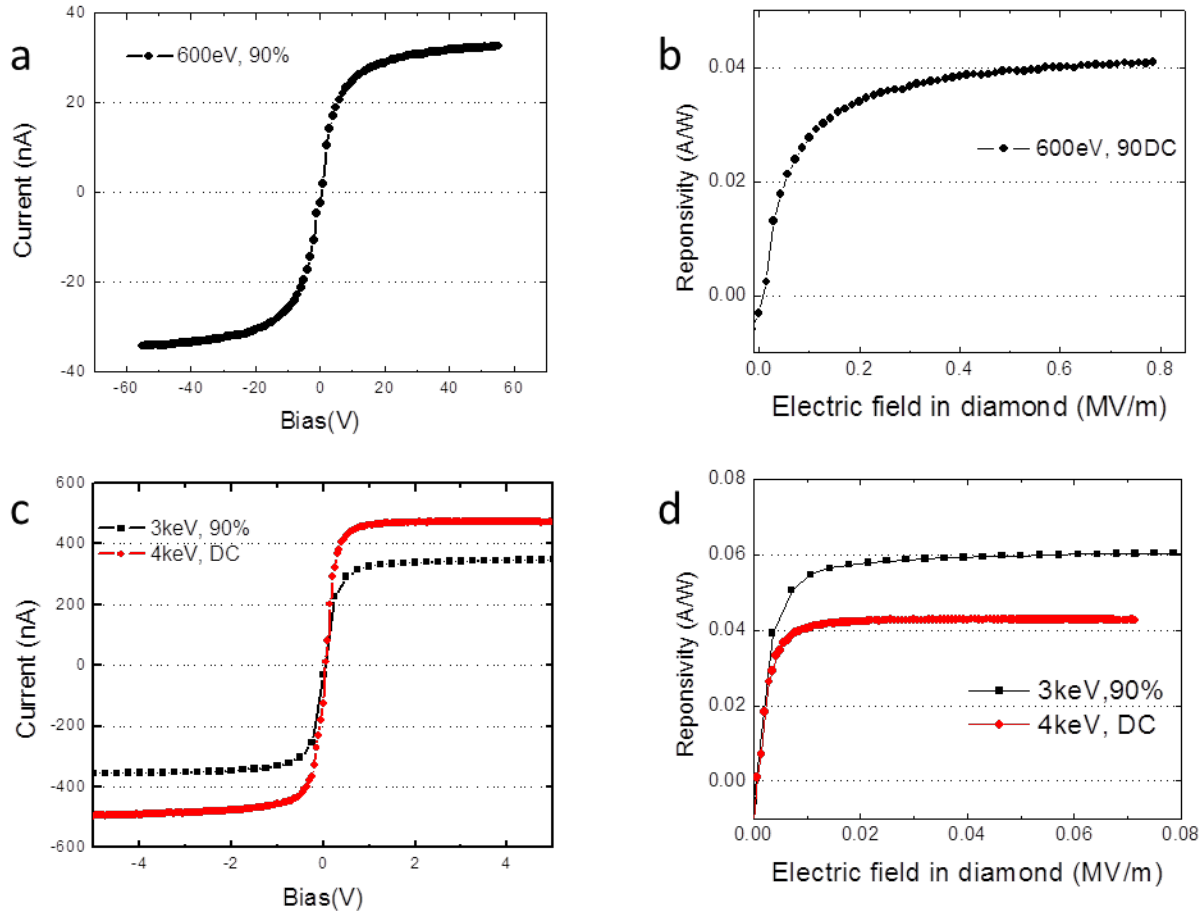

Figure 38 Bias scans from U3C and X8A at various photon energies. Diamond response is plotted with (a)(c) applied bias and (b)(d) electric field in diamond.

Results of bias scans and energy scan taken at beamline U3C and X8A are shown in Figure 38 and Figure 39. A collection of I-V curves taken with different incident photon energies and duty cycles indicate symmetric response for both electron and hole collections. At 600eV, a applied bias of 40V, which can be converted to a inner electric field of ~0.5MV/m is need for this diamond to reach saturated response, while at a incident photon energy above 3keV, a bias of 2V or a field of ~0.02MV/m is sufficient for the device to work at saturated level.

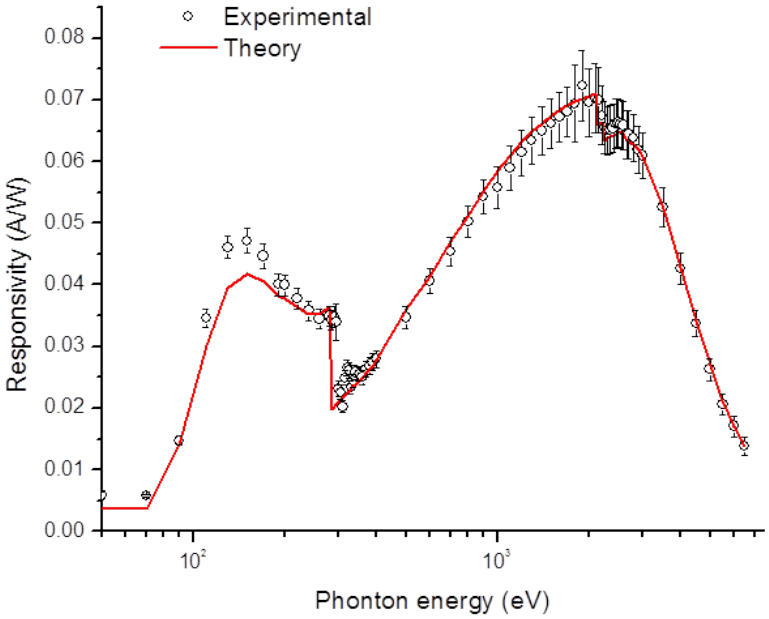

Figure 39 Energy scan of DP12, shown in responsivity. Theory curve is calculated using diamond thickness as 90µm and Pt thickness is 30nm.

The responsivity of this diamond from 50eV to 6.5keV is shown in Figure 39, with a pulsed bias of 50V, 50% duty cycle applied on the beam incident side. A theory curve calculated using Equation 4 assuming full collection for a 68µm diamond with 22nm incident Pt contact is aligned with the sample responsivity for comparison, which gives a well matched curve with the experimental responsivity.

Specification List

- Diamond Thickness: 68µm
- Front Platinum Thickness: 20 nm
- Back Platinum Thickness: nom. 20 nm
- Suggested Operating Voltage: 5 ~10 V DC
- Leakage Current: < 5 pA
- Response at 5 keV: 0.015 A/W

Appendix II Beamlines used in this work @NSLS

Experiments for testing diamond based electronics involve intense use of facilities both at National Synchrotron Light Source (NSLS) and Center for Functional Nanomaterial (CFN) in Brookhaven National Laboratory. Table 4 lists the specifics for beamlines at NSLS that are involved in this work.

Samples are mounted at beamline U3C, X8A and X15A by a holder consists of 2 copper claws holding the diamond in place and making electric connections to the platinum contacts. These beamlines provide a combined photon energy range of 50eV to 60keV for our detector calibration. At beamline U3C and X8A, samples were mounted at end stations which are differentially-pumped high vacuum chamber with a base pressure of 1×10^{-7} torr, while the test at X15A was performed in air.

Table 4 Specifics of beamlines at NSLS that are involved in this work (http://www.bnl.gov/ps/)

Beamline	Technique Used	Photon energy
U3C	XBIC	50-1000 eV
X8A	XBIC	1.0-6.5keV
X15A	Diffraction enhanced imaging	10-60keV
X19C	X-ray topography	6-40 keV
X20C	X-ray diffraction, time resolved	7-11 keV (Si(111));4-11 keV (multilayers)
X23A	X-ray absorption spectroscopy	4.7-30 keV
X24A	X-ray photoelectron spectroscopy	1.8-6 keV
X25	Macromolecular crystallography	5-20 keV
X28	X-ray Footprinting	Focused White Beam

Appendix III IIa_DP12 Diamond Test Report

Sample DP12 is one of the 3 diamonds bread sliced and polished from the original 600μm IIa diamond. Size of this diamond is measured to be 4.25mm × 3.53mm. Sample was chemically cleaned and oxygen terminated on both sides by resting under an ozone lamp for over 4 hrs for each side.

This diamond is prepared into a single channel device following similar steps as the previous IIa diamond. Same square Pt electrodes were sputtered on both sides of the diamond with dimensions measured to be 2.6mm × 2.6mm × 30nm. Sample was then mounted on a PC circuit board using silver paint and the surface electrode was wirebonded with aluminum wires.

Sample was then tested at beamline X15A and X8A, NSLS, BNL. Results are discussed in the following sections.

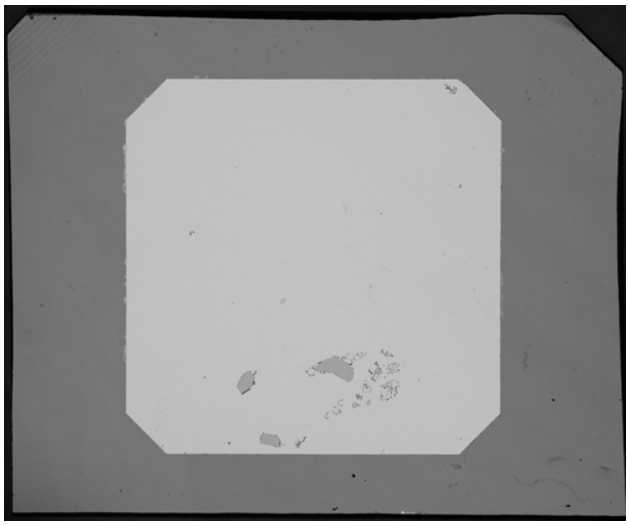

Figure 40 DP12 after metallization. Diamond size: 4.25mm × 3.53mm; Pt electrode size: 2.6mm × 2.6mm.

Experimental

At beamline X15A, sample was mounted on an X-Y micro-motor stage with 19keV x-ray beam incident on the signal side. Beam size is controlled by slits and was determined to be 500μm × 500 μm. A DC bias was applied on the beam exit side of the sample. Beam flux was calibrated by a 10cm ion chamber upstream and a Si diode downstream.

At beamline X8A, this diamond was installed in the beamline calibration stalk with the wirebond side being incident to the beam. Bias was applied to the beam incident side and signal is collected on the beam exit side to avoid photoemission (at X15A because the beam is going all the way through the diamond). Pulsed bias was applied in this test for DC biasing was showing signs of photoconductive gain and charge trapping. Beam goes through a 1/16 aperture and flux

was calibrated by an upstream Si diode and a series of bias scans and energy scans were conducted at various incident photon energies ranging from 1keV to 6.5keV.

Results and discussion

A map of photocurrent taken at beamlime X15A were shown in Figure 41a, with a DC bias held at 80V. The shape and position of the diamond and contact are overlaid with the response map.

Within the range of the contact, the diamond signal is uniform and is measured to be ~500pA, which corresponds to a minimum thickness of 90µm for this diamond according to our calculation. Leakage current is ~1.5pA. It can be noticed from Figure 41a that outside the range of the contact there is a ring of higher response with irregular shape. This is from the backscattering of the silver paint under the diamond, which is irrelevant for this test.

Bias scan shown in Figure 41b was measured in DC condition with the beam positioned in the center of the diamond. Signal saturation was reached around 40V and the saturation current is around 500pA.

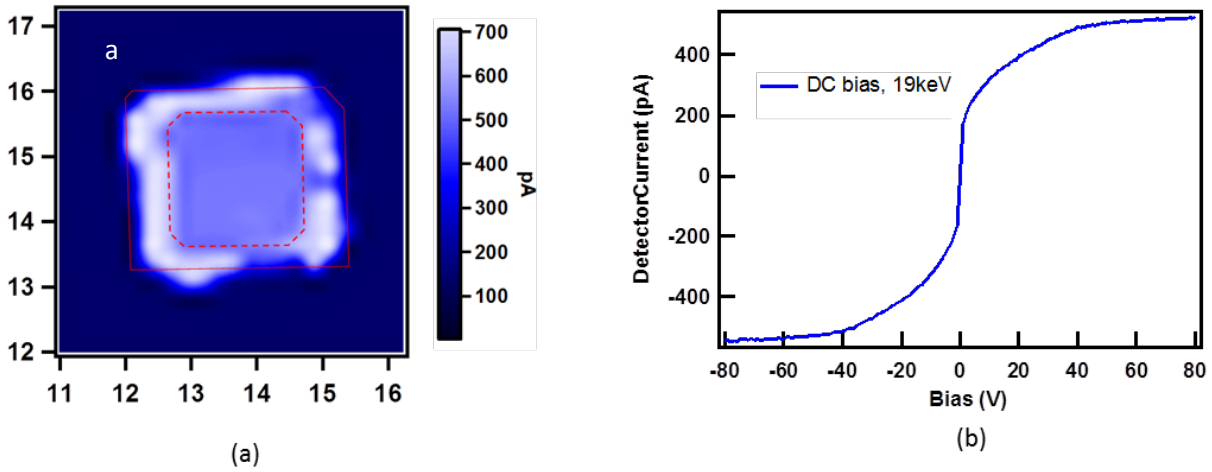

Figure 41 a) Current map of IIa diamond at 80V, DC. The shape and position of the diamond (solid line) and the contact (dotted line) are indicated in the figure. b) Bias scan from X15A, at 19keV.

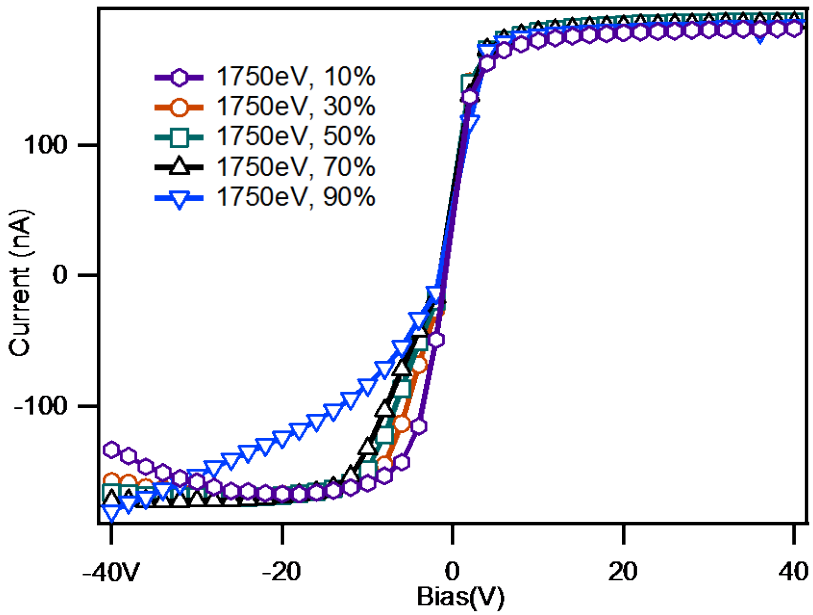

Figure 42 Bias scans from X8A, at 1750eV, bean aperture 1/16".

Results of bias scans and energy scan taken at beamline X8A is shown in Figure 42 and 43. A collection of I-V curves taken with different duty cycles are normalized and compared in Figure 42. It should be mentioned that in these series of tests, the leakage current is measured to be ~1nA, whereas in the previous X15 tests it was ~2pA. This increase in leakage might be caused by handling the sample and switching beamlines. We do not consider it related to the diamond itself. The positive side of these curves represents hole collection and the negative side represents the collection of electrons. From the comparison we can tell that in this diamond the collection for holes saturates around 10V regardless of duty cycle, which has significantly improved from the DC test shown in Figure 41b, while the saturation voltage for electrons varies quite much with changing duties cycles, i.e. at 10% duty cycle the signal saturates much faster than 90% duty cycle. This variation is a sign of charge trapping, possibly due to structural defects like dislocations generated during crystal growth. We have observed much worse charge trapping for the original IIa diamond in the same test, i.e. poor electron collection with low duty cycles at much higher bias. This establishes that thinner diamond can be a compensation for poor crystal quality for our purposes.

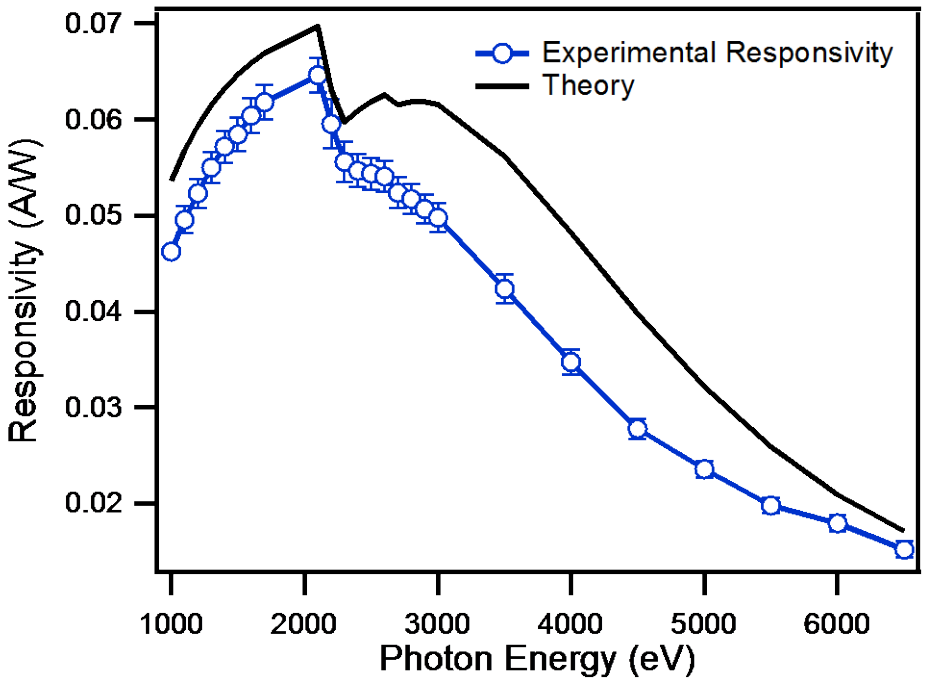

Figure 43 Energy scan of DP12, shown in responsivity. Theory curve is calculated using diamond thickness as 90µm and Pt thickness is 30nm.

The responsivity of this diamond from 1keV to 6.5keV is shown in Figure 43, with a pulsed bias of 40V, 50% duty cycle applied on the beam incident side. A theory curve calculated assuming full collection for a 90µm diamond with 30nm Pt contact is aligned with the sample responsivity for comparison. As can be see form the figure, this diamond is not getting full collection at the applied condition for this energy range and the deviation from the theory curve starts to become prominent when x-ray penetrates the full thickness of this diamond (~3keV).

Conclusions

From the above analysis we can tell that after thinning and polishing, IIa diamond behaves much better than the original diamond and will function as a diamond detector if pulsed bias is applied and full collection is not required.

Specification list:

- Diamond thickness: above 90µm
- Suggested operating voltage: 40V, 50% duty cycle.

Appendix IV Investigation in Pt thickness and coverage

Introduction

At lower energy range, the absorption of metal contact could also play a role in the device signal loss. Therefore, reducing diamond and metal contact thickness becomes a feasible approach to adapt our device to soft x-ray applications. This section summarizes our effort on designing and fabricating platinum coated diamond x-ray detectors to improve device responsivity in real applications, including testing Pt layers with various thicknesses and reducing the coverage of metal electrodes.

Experimental

Our test pieces were electronic grade single crystal CVD diamonds originally coming from the same batch of diamonds purchased from Element Six, and were thinned and polished to a nominal thickness of 100 microns. Samples are cleaned and oxygen terminated to prepare for patterning. Pt electrodes of 5 nm, 10 nm and 15 nm thick with lateral sizes of 1.5mm by 1.5mm were sputtered on the same side of a diamond plate using shadow masking, while a ~20 nm Pt solid electrode was sputtered on the other side of the diamond. The layout of the pads is illustrated in Figure 44a.

A mesh electrode pattern shown in figure 44b was selected to study the effect of Pt coverage. The stripe size and spacing of the mesh pattern are designed to be 100 μm, with lateral dimensions of 3mm by 3mm. Patterning was done at the Center for Functional Nanomaterials at BNL using standard optical lithography and the sputtered Pt electrodes are 30nm thick on both sides of the diamond.

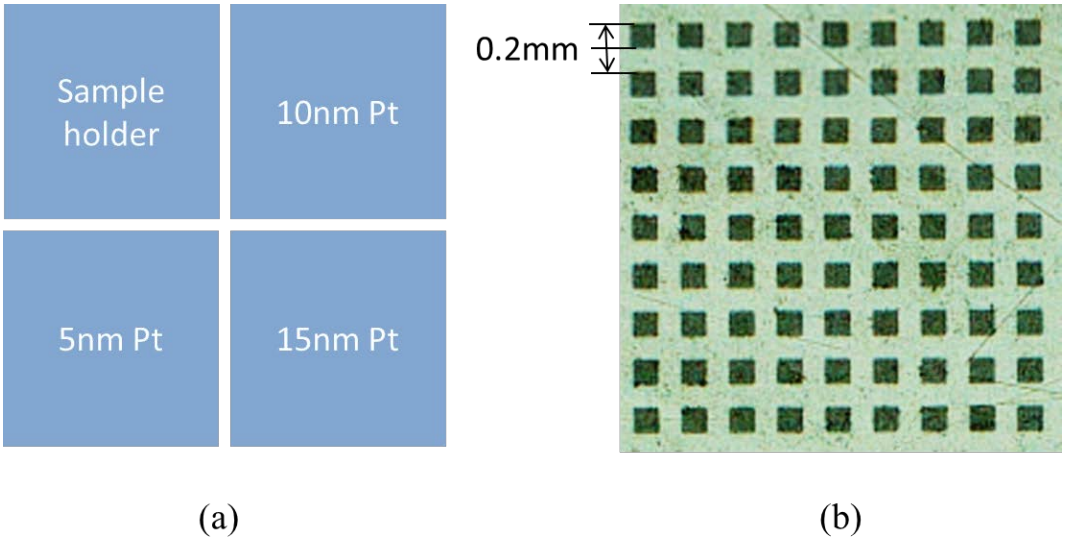

Figure 44 (a) Layout of Pt contacts on diamond surface with various thicknesses. (b) Mesh electrode pattern with 100μm stripes and spacing.

Both samples are mounted on pre-designed PCD boards and tested in the end station at beamline U3C and X8A at NSLS, following our routine measurements of 2D responsivity mapping and energy calibration. Diamond responsivity was mapped for each pad with different thicknesses with a beam diameter of 1/128th inch (200 μm) with applied bias of -50V, 50% duty cycle at 1750eV. Energy calibration was collected with a 1/32nd beam at the center of each pad at -50V with 50% duty cycle from 0.1~ 6.5 keV. In order to study the bias dependence of charge collection for the diamond with Pt mesh electrode, a series of responsivity maps are collected at 600eV at beamline U3C applying different biases with same duty cycle. Energy calibration at a photon energy range of 0.1 ~ 1keV is also collected for this sample to compare with the solid electrodes.

Results and discussion

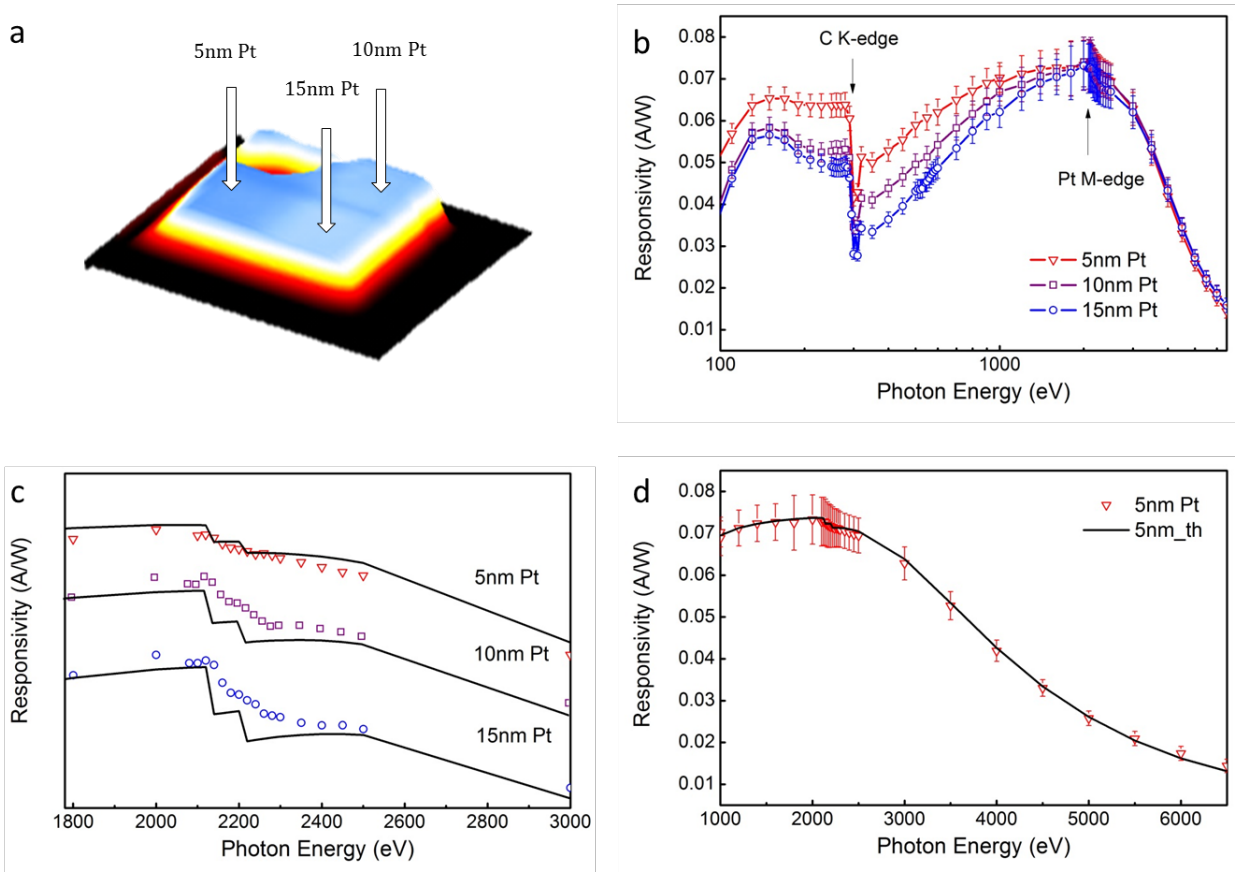

Figure 45 (a) 2D responsivity map of Pt electordes with different thicknesses. (b) comparison between the energy scans taken for different areas on sample surface with different Pt thicknesses.(c) theory fitting for Pt edge d) thickness fitting for diamond thickness.

The responsivity map of Pt electrodes of different thicknesses is shown in Figure 45a and from the figure we can tell that the current increases as the beam scans over the area with thinner Pt electrodes. This effect is also observed in the lower energy range in the comparison between the energy scans from the 3 areas, as Pt thickness has more impact under 1000eV, see Figure 45b.

According to the comparison in Figure 45, the most prominent difference in diamond responsivity rising from Pt thickness variation is observed below 200eV, where Pt attenuateion length various most in this range. After around 2keV, where the Pt layer becomes almost transparent and the change in attenuation length is negligible, the 3 curves start to merge and the difference in diamond responsivity is no longer observable. A better approach to accurately determine the Pt thickness is to fit the theoretical model with the experimental data at the Pt edges at 2122eV and 2202eV,[32] using the equation we introduced in section 2 and section 4. As is shown in figure 45c, the 3 theory curves calculated using using Equation 4 in the RCL model for Pt thicknesses of 5nm, 10nm and 15nm respectively match quite well with the step sizes at Pt edges in the diamond experimental responsivity. In figure 45d, the curve from 1keV to 6.5 keV scanned in the area with 5nm Pt electrode was used to determine the diamond thickness using the same RCL model and the thickness is calculated to be 65 μm.

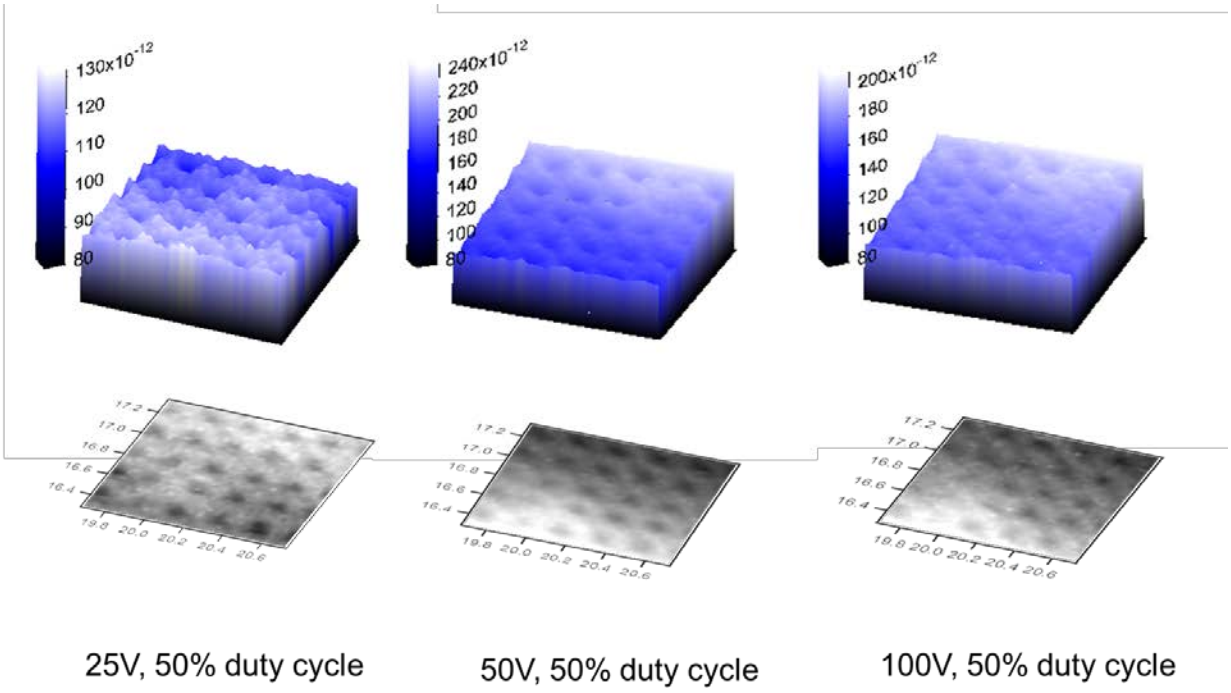

Figure 46 Field dependence of the Pt mesh electrode.

A series of response maps of the Pt mesh electrode taken at different applied bias with same 50% duty cycle are shown in Figure 46. From the comparison illustrated we can tell that the collection of the charge carriers are not uniform over the mesh area, where the signal is always higher at the Pt covered area than the vacant area, indicating an ununiform electric field near the mesh electrode surface in the diamond. This non-uniformity is more prominent at low biases (25V, 50% duty cycle). As bias rises, the 'wells' in the response map were gradually filled up, indicating a recovered uniformity in the electric field distribution in the diamond.

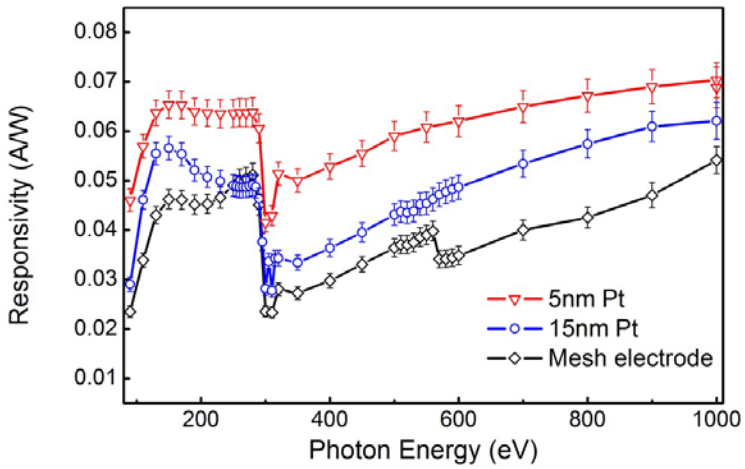

Figure 47 Energy scans taken for 5nm and 10nm Pt electrodes compared with that from the Pt mesh electrode from 0.1~1keV.

The energy scan comparison between thin Pt contact mesh electrodes shown in Figure 47 indicates that a continuous contact works better than the patterned mesh electrode in mainly two aspects. First is that the overall responsivity is higher for the continuous contact. With the same 30nm sputter thickness, the mesh electrode will have less beam loss and therefore more carriers are created in diamond than the solid contacts. However, with 100 μm spacing in this patterned electrode, the carrier loss has a more significant effect, resulting in a lower total responsivity. Another impact of carrier loss in the mesh electrode is that when beam flux changes dramatically, this diamond device loses its linearity. In Figure 30, a detailed scan from 500 eV to 600eV with 10eV interval in the 30nm Pt electrode and the mesh electrode responsivity indicates that the mesh curve has a noticeable step around 560 eV, while the plots for the continuous contacts are smooth. At 560 eV, a programmed filter change occurred in the beamline optics, resulting in beam flux increase. For the diamond with a continuous contact, the responsivity is linear. In fact it was reported in our previous tests that diamond has linear behavior over a beam flux changing 11 orders of magnitude.[8] However, for the mesh electrode, as beam flux increases, more carriers are lost in the bare diamond, resulting in a lower responsivity when calibrated.

Conclusion

Thinner Pt electrode has lower beam absorption under 2keV, leading to higher responsivity in the according energy range. The most prominent difference in diamond responsivity rising from Pt thickness variation is observed below 200eV.

Lower metal coverage will reduce the uniformity of the electric field in diamond, causing an ununiformed special charge collection. The linearity of diamond response will be compromised using the designed electrode pattern. In order to improve charge collection special uniformity and maintain device linearity, electrode needs to be redesigned with features with smaller dimensions.

Appendix V Transmission-mode diamond white BPM at NSLS

Introduction

Simultaneous monitoring of flux, position and timing of intense white beams from third- and fourth-generation light sources can provide an unprecedented tool for beamline and accelerator diagnostics. X-ray beam position monitors based on high-purity synthetic single-crystal diamonds have made great strides towards this goal (Bergonzo et al., 2001; Bohon et al., 2010; Morse *et al*., 2010; Berdermann *et al*., 2010). The flux measurements in such devices are linear over 12 orders of magnitude, from low-power monochromatic light to highpower focused white beams (Keister & Smedley, 2009; Bohon *et al*., 2010). As opposed to position measurements by blades (Shu et al., 1994), which only indicate the location of the beam center of mass based on the diffuse tails, a transmission-mode position monitor provides the location of the actual center of mass of the beam. This paper describes the design, construction and calibration of diamond white-beam position monitors (wBPMs) in the context of the National Synchrotron Light Source (NSLS) X25 beamline, as well as characterization of the correlated motion of the electron beam with the photon beam. The two wBPMs discussed are permanently installed and the flux, position and trajectory of the white beam are continuously monitored.

Beamline layout

The NSLS at Brookhaven National Laboratory operates at 2.8 GeVand a current up to 300 mA. Beamline X25 is a facility beamline dedicated to macromolecular crystallography and is part of a suite of beamlines operated by the PXRR group (Macromolecular Crystallography Research Resource group) and the NSLS. Over the past few years, major upgrades at the beamline have increased the available flux in order to enable use of smaller beams to match the progressively smaller size of samples brought to the beamline. Figure 48 shows the layout of the X25 beamline. Prior to the installation of the wBPMs, the only beam diagnostic tools available were ionization gauges in the experimental hutch, downstream from all optical components. No device other than a fluorescent screen was available for the white beam, not only at X25 but at any beamline at the NSLS. Beamline X25 originally had a tungsten-blade beam position monitor (BPM) installed in the front-end which suffered an internal short circuit and is no longer in service. In addition, preliminary testing of a diamond-blade BPM for the Advanced Photon Source was carried out at X25 where our first wBPM is installed. The diamond-blade BPM has limited utility as it would have to block the user beam to have signal; this illustrates that blade-type BPMs are not appropriate downstream of apertures. Being able to ascertain the quality of the incident beam on critical optical components such as the monochromator or focusing mirror is crucial in controlling the position stability of the beam at the sample.

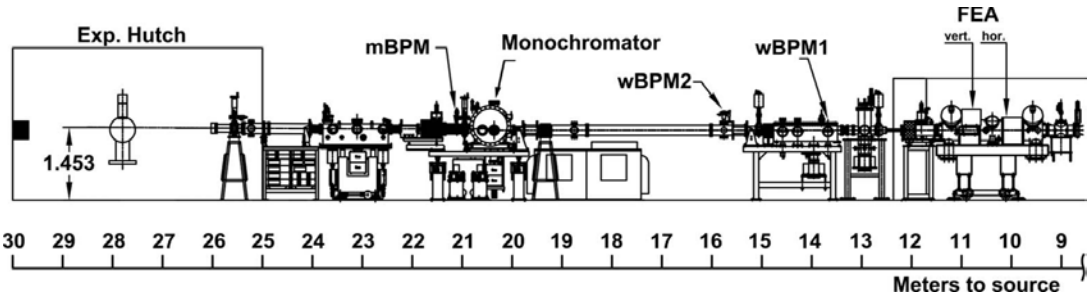

Figure 48 Layout of the NSLS X25 beamline highlighting the locations of the water-cooled upstream wBPM, compact downstream wBPM and the monochromatic mBPM. The undulator is not shown, but all distances are referenced to the center of the undulator position.

An in-vacuum miniature gap undulator (Ablett & Berman, 2007) consisting of 18 mm periods (55 in total) can deliver 4.6 $\times 10^{11}$ photons/s across an energy range of 5 keV to 20 keV. This value is for experiments performed at 11.284 keV with a 100 µm × 100 µm aperture in the experimental hutch exposing the sample. Awater-cooled aperture defines the size of the emitted photon beam. A thin graphite filter (295 µm thick) and a Be window (254 µm thick), attenuating only the low-energy photons, are the only optical elements between the source and the two wBPMs. These monitors are installed in the white beam at 13.5 m and 15.82 m from the center of the undulator source. The original blade-based BPM installed at the front-end was limited to qualitative measurements of the beam position because of stray low-energy radiation from a neighboring bending magnet (Berman *et al.*, 1992). The diamond wBPMs are located after the Be window and graphite filter, and thus are not influenced by this radiation. Downstream of the second wBPM is a sagittally focusing silicon (111) double-crystal monochromator, followed by a commercial foil monochromatic beam position monitor (mBPM) and a focusing mirror, before entering the experimental hutch. The flux of the monochromatic beam is measured using ion chambers placed inside the hutch immediately after a Be window.

Mechanical design

The broad profile of the X25 undulator beam easily fills the maximum usable aperture size defined by the front-end apertures (FEAs) at 10 mm horizontally and 1 mm vertically. The FWHM of the full energy integrated beam at the position of the upstream diamond BPM is 8 mm horizontally and 2.4 mm vertically. At the time of development, there were no commercially available electronic-grade single-crystal diamonds large enough to accommodate the entire beam. To solve this problem, a novel design consisting of two horizontally tiled diamonds was employed to increase the overall width. Typically, a 3 mm × 1 mm white beam, defined by a water-cooled aperture, is used for crystallography experiments, but a larger beam is sometimes required for experiments needing larger flux. The physical separation of the tiled diamonds is estimated to be approximately 50 µm.

Four 100 µm thick electronic-grade single-crystal (001) synthetic chemical vapor deposition (CVD) diamonds from Diamond Detectors Ltd [grown by Element 6 (London, UK)] were selected from a batch of eight. They were screened using white-beam X-ray topography performed at NSLS X19C. Diamonds with the fewest defects known to cause photoconductive

gain in these devices (Muller *et al.*, 2010) were selected. The diamond plates were then subjected to a standard chromic acid etching procedure to remove adventitious carbon from the surface. To supplement the oxygen surface termination left by the chromic acid etching procedure, the diamond plates were placed under an ultraviolet lamp in air for several hours. Platinum electrodes, 30 nm thick, were sputtered through a shadow mask in the pattern shown in Figure 49(a); this thickness has proven to be sufficient for handling the current expected in these devices. Platinum contacts on oxygen-terminated diamond are known to greatly reduce hole injection into localized near-surface defects, suggestive of a blocking nature (Muller *et al*., 2010). Each diamond has two electrodes on the incident surface; the pair of diamonds completes the quadrant. The two wBPMs have different exitside metallization geometry. On the upstream wBPM, each diamond has one solid 30 nm thick platinum electrode with a total size matching that of the front two electrodes. The downstream detector has the same pattern of platinum electrodes on the exit side as the incident side.

Phosphor-bronze clamps hold the diamonds against a copper mount with a 1 mm overlap, providing both structural support and heat sinking. Electrical contact is made to the platinum pads using opposing phosphor-bronze clips. In the center of the device, the two diamond edges are placed in contact; the pad metallization is 200 μm from the edge of each diamond, making a total horizontal separation of ~400 μm. Two thermocouples (k-type) are used to monitor the temperature of the detector; one is placed just below the diamonds on the phosphor-bronze clamp and one several centimeters away on the copper housing. A copper mask is installed on the upstream wBPM, exposing only the diamonds and shielding the outer components while allowing a 3 mm path above the diamonds. The downstream wBPM includes a similar mask, but made of molybdenum. The opening in the mask is ~8 mm horizontally and ~12 mm vertically, allowing a beam bypass above the diamonds similar to that for the upstream wBPM. The wBPMs have similar mounting near the diamonds, and are installed on a manipulator stage with horizontal and vertical motions for alignment. The upstream wBPM is mounted on a water-cooled copper block, making it bulky but very temperature stable. The downstream wBPM was designed for compactness, with no water cooling, instead relying on heat dissipation from the copper block and a copper rod support. The entire assembly for the second wBPM can fit through a standard 2.75 inch ConFlat flange.

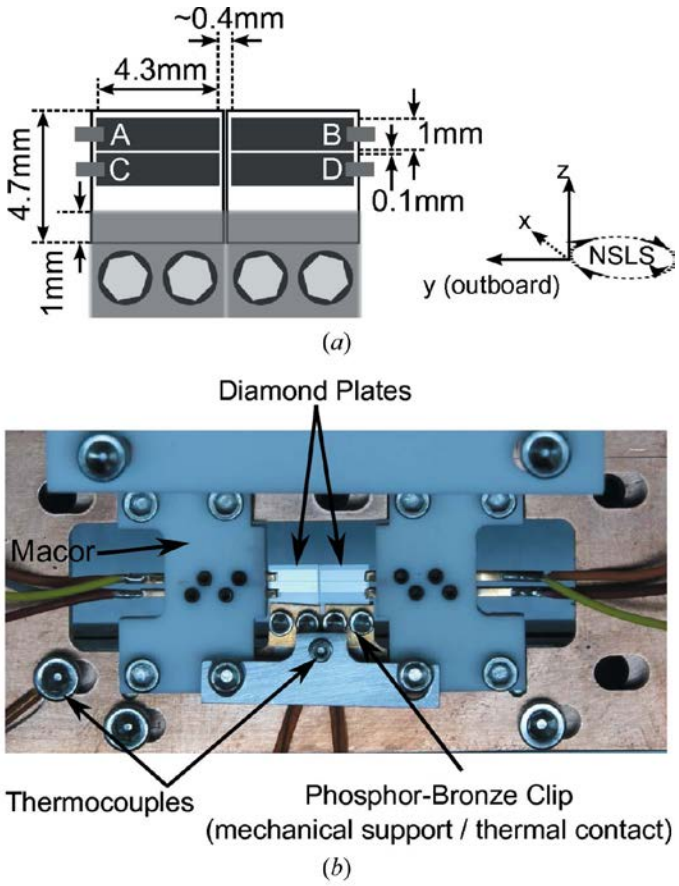

Figure 49 (a) Diagram of the electrical and thermal contacts to the diamonds as well as the dimensions of the platinum metalization. The overlap of the diamonds with the copper block is nominally 1 mm, clamped by a phosphor-bronze clip. (b) An overview photograph of the upstream water-cooled diamond wBPM, showing the intermediate electrical contacts and the Macor electrical isolation.

Response uniformity and flux linearity

Prior to installation in the white beam, the electrical response in transmission mode for each diamond plate was characterized as described elsewhere (Keister & Smedley, 2009). It is important that the detector be free from regions of photoconductive gain to ensure predictable response dependent only on the absorbed X-ray flux. X-ray beam induced current (XBIC) mapping was performed at X25, where a 50 µm × 50 µm monochromatic beam (10 keV) was raster scanned across the plates (Figure 50a). A 50 V bias was placed on the back electrode and the current was measured from each pad with Keithley electrometers (model numbers 6514 and 6517A). The data shown are from the upstream wBPM. The reduced response in the unmetalized portion of the wBPM arises from the reduced electric field in this fringing region where full charge collection is not achieved. While some detrimental photoconductive gain was observed when using a positive bias, a uniform response with no photoconductive gain was exhibited in negative polarity.

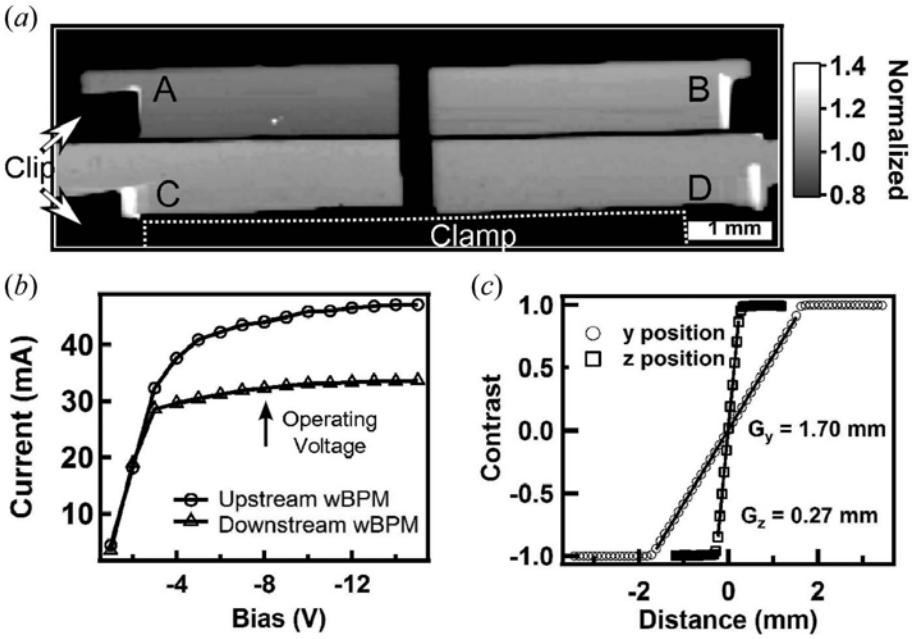

Figure 50 (a) XBIC image of the downstream diamond detector showing uniform response over the entire device (-50 V applied to the exit side of the diamond). The detector is rotated to avoid artifacts arising from the scan direction. The dark regions are caused by the electrical clips making contact with the platinum pads and by the phosphor-bronze clamp. The data are normalized to the expected value for full charge collection. (b) The sum of the current on the four pads versus the applied bias. The detectors are operated above the saturation region where there is full collection of the generated charge carriers. (c) Position calibration performed at beamline X28C.

During regular operation at the beamline, only negative bias is applied to back electrodes of the wBPMs, avoiding the photoconductive gain observed under positive bias. To minimize the ohmic heating in the devices, the lowest possible voltage is used while still remaining in saturation (at an operating voltage of 8 V, the measured charge collection efficiency is 96%) as shown in Figure 50(b). The wBPMs were tested for flux linearity at NSLS X28C; see Fig. 1 (Bohon et al., 2010), then calibrated at X25 to take into account the different incident beam sizes used. When both wBPMs are in use in the beam, the signal decreases by 33% on the downstream wBPM, as expected, owing to absorption of the lowenergy photons by the first set of diamonds. The wBPMs absorb a significant fraction of the total X-ray power, but they do not significantly reduce the photons at energies where the beamline typically operates (11 keV to 13 keV). This is in agreement with theoretical values (CXRO) (Henke et al., 1993), which predict that each device will reduce the number of relevant photons by only 5.4%.

The individual current for each quadrant is measured through a custom-built current-to-voltage amplifier capable of handling up to 3 A per channel. The voltage is read with an Acromag IP330 data acquisition board on an AVME 9668 carrier card. The data are harvested continuously at the full bandwidth of the IP330 of 67 kHz and averaged into 1 Hz bins suitable

for correlation with the experiments performed at the beamline. A flat data file is created with all the diagnostics values from the wBPMs, monochromatic BPM and ion gauges along the beamline. A plot is deposited in the experimental database showing the beam position and intensity for the users to correlate with their experimental data. The values are made available throughout the NSLS facility via an EPICS Channel Access gateway.

Thermal considerations

The temperature increase in the wBPM has two main contributions: X-ray power directly absorbed in the device and ohmic heating. The amount of X-ray power absorbed in the diamond depends on the energy spectrum of the undulator beam and the thickness of the diamond; fortunately, our results indicate that the temperature rise owing to absorption is negligible. The downstream wBPM temperature only drops a few degrees Kelvin when the X-rays are incident on them with the bias turned off; the temperature of the water-cooled upstream wBPM remains stable. Ohmic heating, however, places a significant heat load on the device. Again, this is why the wBPMs are operated at a low bias. After applying the nominal bias of 8 V, the upstream water-cooled wBPM, as expected, is very thermally stable and shows only slight, negligible motions with changing heat loads. The downstream wBPM, however, does have some noticeable motion with changing heat load (warm-up period after powering on the device). No change in temperature is observed when there is bias on the device but no incident light.

The front-end slits were opened completely to determine the maximum total optical flux (and power) in the white beam incident on the detectors. The horizontal extent of the beam is larger than the 8.0 mm horizontal aperture of the protective wBPM masks. The measurable vertical extent of the beam is limited by the total height of the active area on the plates (2 mm). With a synchrotron ring current of 265 mA and the undulator gap closed to 5.68 mm, fully illuminating the detector, total currents of 748 mA and 610 mA were observed in the upstream and downstream wBPMs, respectively. This corresponds to ~80 W of total X-ray power incident on the first wBPM. The temperature at the diamond position under these conditions reached 384 K after several minutes of illumination.

Position calibration

The position of the X-ray beam is determined from the separation of charge carriers between the four quadrants of the wBPM, measured individually. The y and z positions of the beam are determined using the following formulae,

$$y = G_y \frac{(I_B + I_D) - (I_A + I_C)}{I_A + I_B + I_C + I_D} \qquad \textbf{Equation 9}$$

$$z = G_z \frac{(I_A + I_B) - (I_C + I_D)}{I_A + I_B + I_C + I_D} \qquad \textbf{Equation 10}$$

where y is defined as the horizontal outboard direction and z is the vertical direction. I_A, I_B, I_C and I_D are the currents collected from each of the four pads. Gy and Gz are the calibration constants in units of mm for a give beam size in the y and z directions, respectively.

The initial calibration, performed at X28C, was used to test the position and flux linearity, as well as thermal performance. Beamline X28C produces focused X-ray white beam capable of delivering almost 90 W mm^{-2} to the focal point (Sullivan et al., 2008); however, full flux was not used in this test. A 4 mm x 1 mm aperture blocked the unfocused white beam to create a similar profile beam as that for X25. Each diamond detector was placed in a nitrogen enclosure to limit the ozone production by the X-ray beam which may degrade the electrodes. The devices were scanned through the beam in both the horizontal and vertical directions using precision motors. The sensitivity constants, *Gy* and *Gz*, were obtained from the inverse of the slope in the active region of the detector, as shown in Figure 50(c). The sensitivity factors are unique for a specific beam shape and intensity profile. From this calibration graph, it can be determined that there is a large region over which the position calibration is linear, specifically, nearly 4 mm in the horizontal and 0.5 mm in the vertical dimensions.

Noise and stability

A measurement of the position noise was also performed at X25 on both wBPMs [Figure 51(a) and 51(b)]. The two wBPMs are initially centered with respect to the beam; position and angle are measured with respect to this alignment. The r.m.s. noise which includes all sources, is approximately 100 nm in the vertical direction and 500 nm in the horizontal. The comparatively high noise level in the horizontal is in part due to the beam shape (the beam is much wider than it is tall), and also to a decreased sensitivity in the detector owing to the separation of charge between two different diamonds. This effect can arise from geometrical and electrical asymmetries (defect density and thickness differences between the diamonds) near the inner edge of the diamond. Any slight asymmetry in the horizontal metalization can result in a situation where the charge generated in one diamond (and collected by that diamond) could be physically closer to the other diamond. This can result in an apparent motion in the opposite direction. Also, at the edge of the diamond where defect density is high, a non-uniform charge collection can have a similar effect. In Figure 51(b) there is an apparent vertical thermal drift in the second uncooled wBPM of the order of 5 mm when the mini-gap undulator is closed to 5.6 mm, providing maximum flux. The apparent drift stabilizes over an hour, as the copper block support slowly heats to its equilibrium temperature of 318 K. The temperature near the diamonds reaches an equilibrium temperature of 325 K within a few minutes. Once the wBPM has stabilized, the vertical noise is comparable with that of the water-cooled upstream wBPM. This stabilization period induces an apparent drift of the vertical beam angle, stabilizing to a value of 0.07 μrad in the horizontal and 0.06 μrad in the vertical. The temperature of the two WBPMs also depends on the undulator gap. Fully closed (gap = 5.6 mm), the temperature nearest the diamond is 315 K and 349 K for the upsteam and downstream detectors, respectively. Fully open (gap = 7.0 mm), the temperature nearest the diamond is 313 K and 341 K for the upsteam and downstream detectors, respectively. By taking the sums of the current in the four pads of each detector, the wBPMs can be used as flux monitors. With the known spectrum of the beamline undulator (Tanabe et al., 2007), and the absorption in the diamond, the power in the white beam can be calculated. In Figure 51(d) the white-beam power is overlaid with the current in the synchrotron

storage ring. The power in the white beam was determined using the known undulator spectrum, the absorption of the diamond and the current in the device. The slow decay of the beam did not result in any change in the beam position, confirming the linearity of the response with incident power on the diamonds.

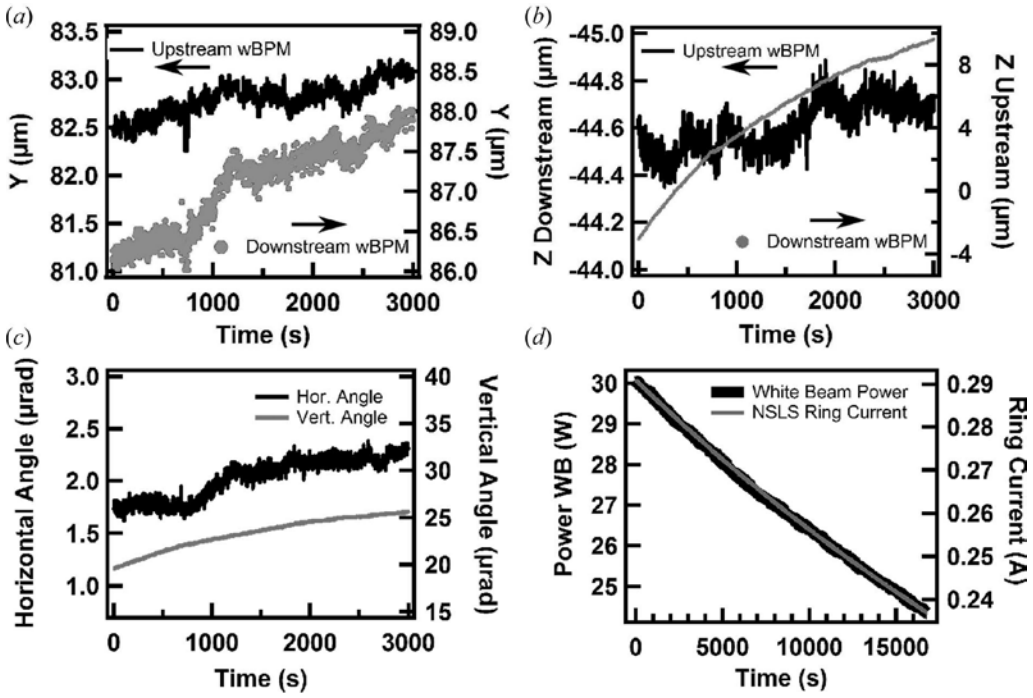

Figure 51 (a), (b) The horizontal and vertical position noise observed by both wBPMs. (c) The angular position of the photon beam. (d) Power in the white X-ray beam as measured by the wBPM and the current in the synchrotron storage ring.

Motion of X-ray source

The wBPMs were used to investigate the correlation of the motion in the photon beam with motion of the electron beam as it passes through the undulator. In collaboration with the NSLS, the electron orbit was altered to provide local translations and angular changes in the electron beam. The beamline layout is crucial for understanding the motion observed by the two wBPMs. The position of the electron beam is monitored at both the entrance and exit of the undulator by pick-up electrodes (PUEs) which are capable of determining the position of the electron beam to a resolution of about 10 mm. From the undulator, the photon beam has a divergence of 0.4 mrad × 0.1 mrad (h × v), trimmed by front-end FEAs located 10 m downstream. The FEA defines a new virtual source for the two wBPMs and will impact the motion of the photon beam. The FEAs are normally set to 3 mm× 1 mm (h × v) but can be varied to accommodate some experiments.

The X25 beamline set-up results in parallax motion of the photon beam, pivoting about the FEA as the primary source moves, a real motion of the photon beam. This is best illustrated by making deliberate motions of the electron beam (Figure 52a) and comparing these with the

observed motions of the photon beam (Figure 52b). The electron beam was moved in steps of 50 μm to a total vertical deviation from the standard orbit of 150 μm in both directions, recorded by the PUE on each side of the undulator. Upon deflection of the electron beam, the photon beam is observed to move in the opposite direction, which is consistent with parallax. As expected, the motion on the downstream wBPM is greater than on the upstream wBPM because the downstream wBPM is farther from the aperture than the upstream wBPM. The observed coupling between horizontal and vertical motions can arise from either a small angle between the detector orientation and the beam motion or a slight vertical misalignment between two diamonds of the same detector. A consequence of having the FEA is that a purely translational move of the electron beam introduces both a translation and an angular change to the photon beam. Unfortunately, the active area of the wBPM cannot accommodate the full undulator beam, so the aperture could not be removed or opened enough to avoid this effect.

The effects of angular motions of the electron beam on the photon beam were also investigated. Symmetrical movements of the electron beam (in opposite directions) about the center of the undulator were made, resulting in an angular trajectory of the electron beam through the undulator. We were limited to angles that were smaller than the source divergence (meaning that the aperture was still defining the beam size), thus only subtle movements in the photon beam were observed (Figure 52c).

Undulator gap and photon beam motion

The beamline typically operates with the undulator gap between 5.6 mm and 7.0 mm. One of the first observations with the wBPM was that the photon beam, in some cases, moves when the undulator gap is changed. It was also observed that intentional misalignment of the electron beam results in a photon beam position that depends on the value of the undulator gap. The stability of the photon beam position during undulator gap changes is dependent on both translation and angular movements of the electron beam. The horizontal position is most sensitive to the intentional misalignment, moving up to 15 μm as the gap is scanned from 5.6 mm to 7.0 mm for an intentional translational misalignment of 150 mm of the electron beam. In Figure 52(d) the position of the photon beam is shown as a function of the undulator gap.

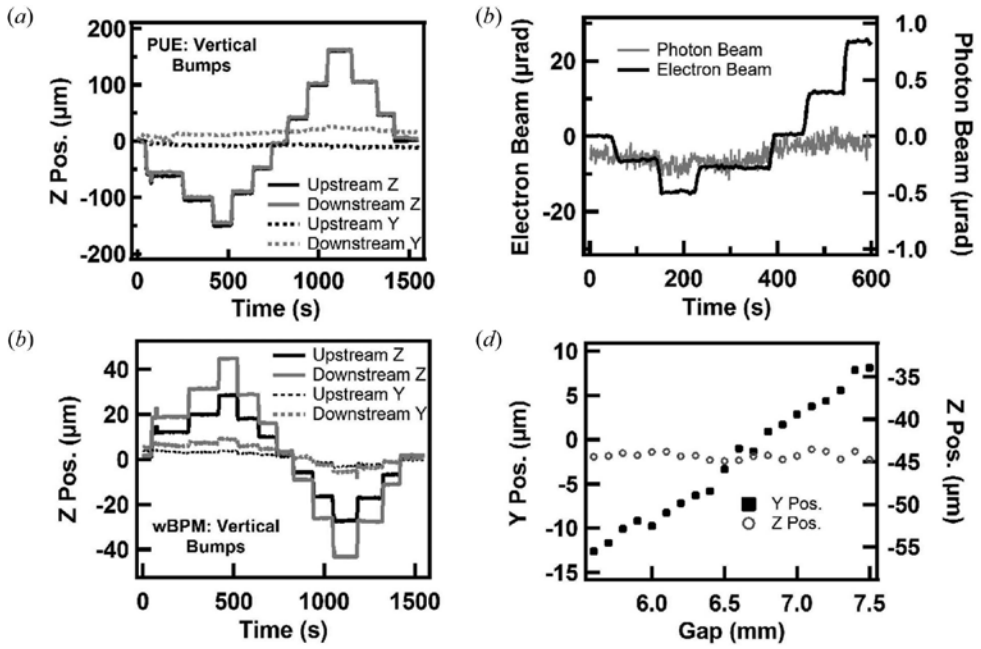

Figure 52 (a) Position of the electron beam showing 50 mm steps. (b) Corresponding motion of the photon beam as measured by both wBPMs. (c) Movement of the photon beam from angular movements of the electron beam, demonstrating that the photon beam does not respond to small angular motions of the electron beam. (d) Position dependence of the photon beam versus the undulator gap separation.

Conclusions

We have demonstrated that CVD diamond-based quadrant detectors perform well for constant monitoring of the flux and position of the white beam generated by an undulator. By employing two wBPMs, the angle of the photon beam can also be measured. The position sensitivity is 500 nm in the horizontal direction and 100 nm in the vertical direction for current devices. Up to 748 mA (gap of 5.68 mm) total current has been measured in the diamonds when the apertures were opened. A low bias is used to minimize the heat load on the device while still collecting all the generated charge carriers. Because of thermal drift in the non-water-cooled wBPM and the presence of the upstream FEAs, detection of angular motions of the beam are limited and should only be performed after they have thermally stabilized. The wBPM has proven to be reliable and robust, showing no degradation after more than one year in use. These devices represent a new type of beamline diagnostic, allowing inline optimization of the undulator and calibration of the frontend apertures during commissioning of new beamlines as well as during normal operation. As they are sensitive to electron beam motion in the insertion device, they also represent an accelerator diagnostic to check and complement existing electron BPMs and could potentially be used to correct motions using a feed-forward procedure (Chrin et al., 2008). The compact design allows easy installation in the beamline and the electronic readout set-up is simple and inexpensive to implement and incorporate into the beamline software.

Appendix VI Boron doped diamond as a contact

Introduction

There have been substantial interests in developing diamond based sensors in high-radiation, high heat-load environments due to its outstanding physical properties such as low x-ray absorption, wide band-gap, high heat conductivity, high breakdown voltage and radiation hardness.[2, 8, 31, 62] Various types of electrodes have been investigated to improve diamond based electronic devices.[8] Within which the p-type synthetic diamond electrodes with substitutional boron acceptors have been fundamentally studied and developed into temperature, pressure as well as electrochemical sensors over the past decades.[63-67] Our particular interest in boron doped diamond is to create a low absorption diamond contact for soft x-ray applications as an alternative to metal contacts.

Photoelectron spectroscopy has been intensely applied to characterize boron doped diamond (BDD) material to study the core level chemical shifts due to surface groups (mostly hydrocarbon species) [68-71] and various surface terminations induced band bending under controlled conditions.[67, 72-74] However, the probing of BDD valence band only appears in a few works and mostly on poly crystalline diamond thin films. [67] In our previous work we have successfully probed the valence band structure for intrinsic electronic grade single crystal diamond using hard x-ray photoelectron spectroscopy (HAXPES) and compared with theoretically calculated results.[75] In this section, we are expanding this method to study the core level and valence band structure of various boron-doped diamond samples prepared in different doping techniques.

Experiment

3 types of boron doped samples have been prepared and investigated. A fully boron doped single crystal diamond with a doping level of $10^{19}cm^{-3}$; a delta boron doped sample with [B]~ $5\times10^{20}cm^{-3}$; and an as grown boron doped epitaxial layer ([B]~$5\times10^{20}cm^{-3}$) are grown separately by microwave plasma-enhanced chemical vapor deposition (MPCVD). The first sample was 3mm×3mm×0.3mm and the other 2 are grown on 4mm × 4mm × 0.3mm diamonds. All diamonds are electronic grade single crystal diamonds ([N]< 5 ppb).

Boron doped layer ([B]~$5\times10^{20}cm^{-3}$) were grown epitaxially on a 4mm by 4mm electronic grade single crystal diamond ([N]< 5 ppb) by microwave plasma-enhanced chemical vapor deposition (MPCVD) and then polished down to an approximate thickness of 6nm.

HAXPES measurements were conducted at NIST beamline X24A at National Synchrotron Light Source (NSLS) with an incident photon energy of $h\nu$ =2145 eV and a bulk sensitive geometry by orient the sample surface to the spectrometer normal. The incident x-ray beam is tuned by a Si (111) double crystal monochromator and signals are collected by a hemispherical electron analyzer, with the pass energy set at 200 eV. Samples were heated to over 600°C to remove surface contamination from various carbon species.

Results and discussion

The carbon 1s XPS spectra collected from boron doped samples with different doping levels and techniques as well as the respective decomposition using XPSPeak 4.1 are as illustrated in Figure 53. A slight background has been removed from each plot using a non-linear Shirley function prior fitting and peaks are normalize and intensity is shown in arbitrary units.[51] Sub peak binding energies and assigned carbon chemical groups for each sample are listed in Figure 53d for comparison.

Note that in the boron implanted sample spectra, the sub peak ascribed to C=C graphite like carbon is significantly higher than the other boron doped diamond samples, which indicates the implantation induced lattice disorder in diamond. Studies showed that ion implantation will introduce lattice damage to diamond structure and though will be partially recovered under appropriate annealing processes, certain structural distortion still remains.[76-79] In section 3 and section 4 we have discussed the likely impact towards device performance coming from structural defects in diamond crystal, especially the ones close to diamond surface. Therefore, such structural damage might lead to a compromised device performance if we apply boron implantation as a diamond contact.

The dominant peak located at 284.3±0.1 eV for each spectra represents the carbon in sp^3 bulk. These peaks are found at relatively the same binding energy but differ slightly in peak intensity and band width for each spectrum. The bulk peak is symmetric and the chemical shift from other carbon species break the symmetry of the overall carbon 1s peak shape.

Besides the sp^3 bulk peak, the next main component in these spectrum are the broader peak located at 284.8±0.1 eV, which is reported to be attributed to hydrocarbon groups CH_x ($x\geq2$) absorbed in boron doped diamond layer during growth. In the 2 boron doped samples, this component was found at the same position while in the boron implanted sample spectra, it was shifted towards lower binding energy by 0.2eV. Note that these samples were prepared in a CH_x and H_2 environment and the relative intensity of this component is mainly determined by the feedgas and deposition pressure. [67, 70, 72]

Another weak peak found at a higher binding energy of 286.1±0.1eV for boron doped samples and 287.5±0.1eV for boron implanted diamond also contribute to each spectrum, which possibly come from the various types of oxygen bonded carbon.[70, 73, 74]

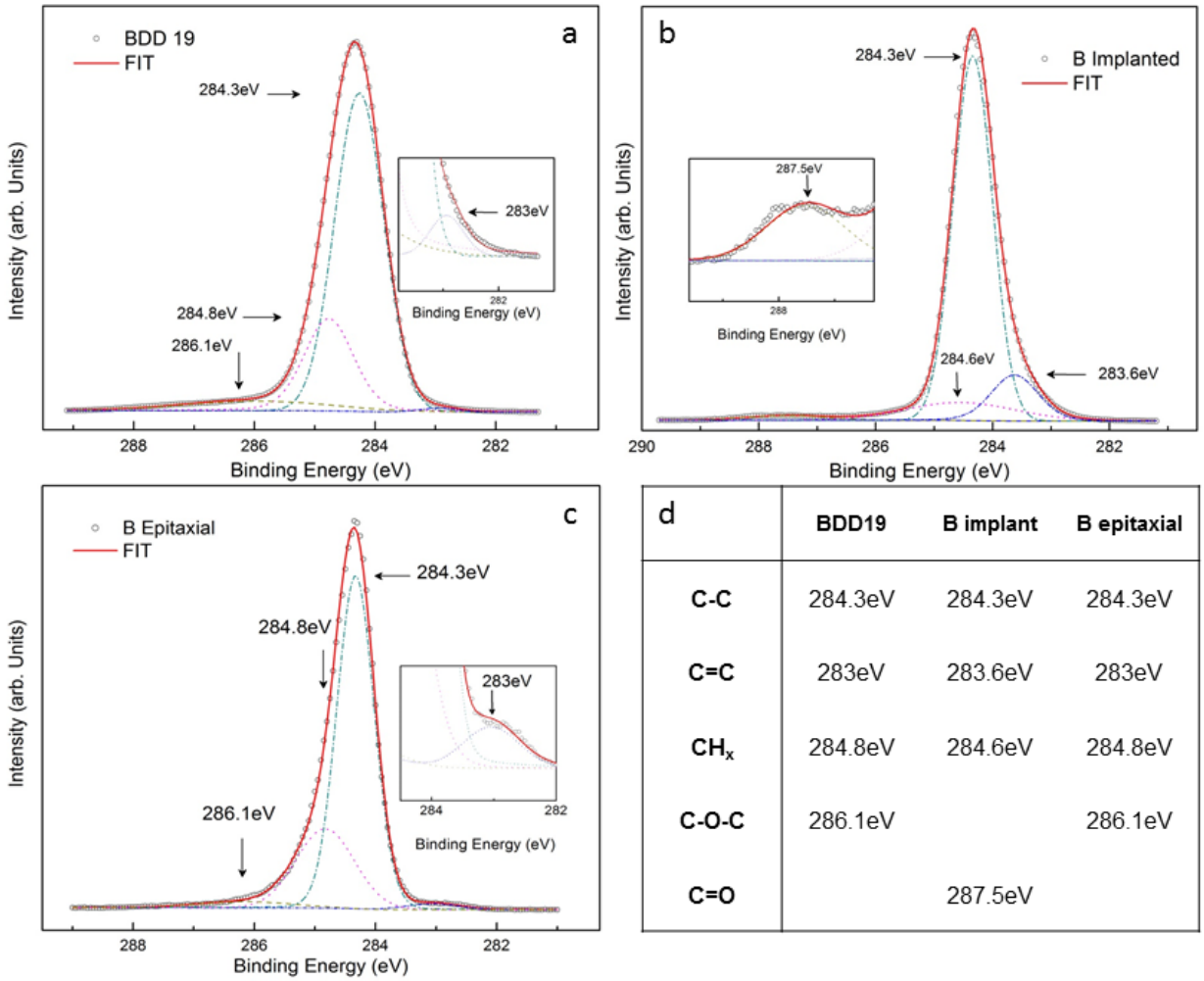

d	BDD19	B implant	B epitaxial
C-C	284.3eV	284.3eV	284.3eV
C=C	283eV	283.6eV	283eV
CH_x	284.8eV	284.6eV	284.8eV
C-O-C	286.1eV		286.1eV
C=O		287.5eV	

Figure 53 XPS carbon 1s spectrum (circular dots) and fitted curve (solid line) of a)Fully boron doped diamond with [B]~ $10^{19}cm^{-3}$.b) Boron implanted diamond.c) Boron (100) epitaxial layer with [B]~ $5\times10^{20}cm^{-3}$. d) Sub peak binding energies and assigned carbon chemical groups.

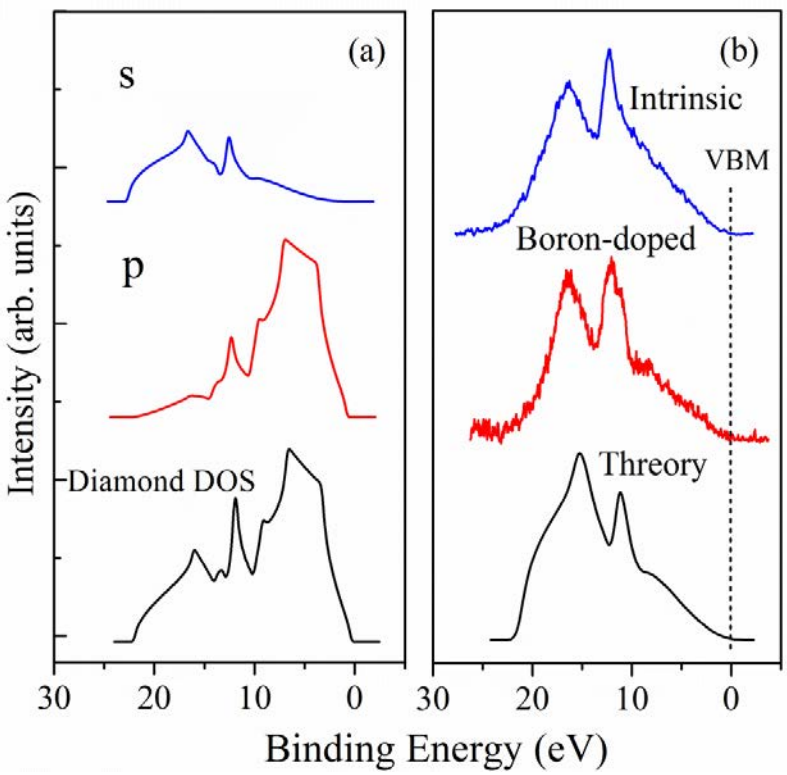

Figure 54 (a) Calculated partial and total DOS for diamond. (b) Dark curve is cross section applied total DOS for diamond at an incident photon energy of 2.15keV, convoluted with Gaussian (FWHM ω=0.26 eV). Experimental valence band structure of intrinsic diamond (blue line), boron doped diamond layer (red line) are compared with the theory. The feature VBM position are marked by dotted lines.

The valence band structure of obtained from the boron doped layer is compared with that from the intrinsic diamond, as well as the calculated density of states using 1st principle method. (see Figure 54) From the comparison we can tell that the overall construction of the valence band structure from the 3 plots are similar except for a few differences. One feature is that the boron doped diamond gives a clear sp^2 shoulder at around 10eV, which resembles the theory VB better than the intrinsic diamond. In the VB diagram of the intrinsic diamond, the sp^2 shoulder is smeared out due to surface charging while it appears in the VB plot of the boron doped diamond due to its conductivity. Another noticeable feature is the shoulder appeared next to the peak at around 11eV towards lower energy. This peak does not have a comparable counterpart in the theoretical VB for the intrinsic diamond, which might suggest that it's corresponding to states generated by boron doping.

Conclusion

The information extracted from the carbon corelevel indicates that the boron implantation will introduce lattice disorder and possibly structural defects close to the surface of the diamond, which might be potential charge trapping sites that'll lead to various electronic concerns. However, both the corelevel and the valence band analysis for the boron doped diamond epitaxial layer indicates a near-unchanged crystal structure compare to intrinsic diamond which might lead to a better device performance than to use boron implantation as diamond contact. Further work is needed to determine the cause of the changes in the valence band structure of the BDD epitaxial layer as well as to fabricate and test a diamond detector with BDD as its contact.